

1.0 1.1 1.25 1.4 1.6 1.8 2.0 2.2 2.5 2.8 3.2 3.6 4.0

MICROCOPY RESOLUTION TEST CHART
NATIONAL BUREAU OF STANDARDS-1963-A

ETL-0212

(4) IFVEL #

AD A110795

Optical power spectral
analysis for machine-readable
factor maps

Robert D. Leighty

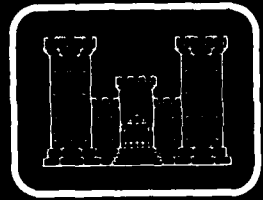
DECEMBER 1980

DTIC
ELECTE
FEB 11 1982
S B

DTIC FILE COPY

U.S. ARMY CORPS OF ENGINEERS
ENGINEER TOPOGRAPHIC LABORATORIES
FORT BELVOIR, VIRGINIA 22060

APPROVED FOR PUBLIC RELEASE - DISTRIBUTION UNLIMITED



E

T

L



Destroy this report when no longer needed.
Do not return it to the originator.

The findings in this report are not to be construed as an official
Department of the Army position unless so designated by other
authorized documents.

The citation in this report of trade names of commercially available
products does not constitute official endorsement or approval of the
use of such products.

UNCLASSIFIED

SECURITY CLASSIFICATION OF THIS PAGE (When Data Entered)

REPORT DOCUMENTATION PAGE		READ INSTRUCTIONS BEFORE COMPLETING FORM
1. REPORT NUMBER ETL - 0212	2. GOVT ACCESSION NO. AD-A110795	3. RECIPIENT'S CATALOG NUMBER
4. TITLE (and Subtitle) OPTICAL POWER SPECTRAL ANALYSIS FOR MACHINE-READABLE FACTOR MAPS	5. TYPE OF REPORT & PERIOD COVERED Research Note	
	6. PERFORMING ORG. REPORT NUMBER	
7. AUTHOR(s) Robert D. Leighty	8. CONTRACT OR GRANT NUMBER(s)	
9. PERFORMING ORGANIZATION NAME AND ADDRESS Research Institute U.S. Army Engineer Topographic Laboratories Fort Belvoir, VA 22060	10. PROGRAM ELEMENT, PROJECT, TASK AREA & WORK UNIT NUMBERS 4A161102B52C	
11. CONTROLLING OFFICE NAME AND ADDRESS U.S. Army Engineer Topographic Laboratories Fort Belvoir, VA 22060	12. REPORT DATE December 1980	
	13. NUMBER OF PAGES 134	
14. MONITORING AGENCY NAME & ADDRESS (if different from Controlling Office)	15. SECURITY CLASS. (of this report) Unclassified	
	15a. DECLASSIFICATION/DOWNGRADING SCHEDULE	
16. DISTRIBUTION STATEMENT (of this Report) Approved for public release; Distribution unlimited.		
17. DISTRIBUTION STATEMENT (of the abstract entered in Block 20, if different from Report)		
18. SUPPLEMENTARY NOTES		
19. KEY WORDS (Continue on reverse side if necessary and identify by block number) Computer simulation map storage and retrieval diffraction pattern sampling Terrain Information Systems graphics data base		
20. ABSTRACT (Continue on reverse side if necessary and identify by block number) A preliminary investigation of the application of Optical Power Spectral Analysis (OPSA) approaches to machine-readable factor maps for terrain information systems is presented. The objective is to offer a more compact, simpler, and cheaper data base storage and retrieval system that would be available by all digital technology. In the basic concept of the systems, OPSA is used to decode data from reduced factor maps that have been encoded by spatial frequency and direction of optical gratings.		

DD FORM 1473
1 JAN 73

EDITION OF 1 NOV 65 IS OBSOLETE

UNCLASSIFIED

SECURITY CLASSIFICATION OF THIS PAGE (When Data Entered)

1:2

PREFACE

This study was conducted under DA Project 4A161102B52C, Task S2, Work Unit 0007, "Optical Power Spectral Analysis for Pattern Recognition."

The author wishes to express his appreciation to Mr. David Rall and Mrs. Rosalinda Barron for their assistance in the preparation of the illustrations for this report.

The study was done during the period October 1977 to September 1978 under the general supervision of Mr. Melvin Crowell, Jr., Director, Research Institute.

COL Philip R. Hoge, CE and LTC William T. Stockhausen, CE were Commanders and Directors and Mr. Robert P. Macchia was Technical Director of the Engineer Topographic Laboratories during the study period.



Accession No.	
1755	
1755	
1755	
1755	
By	
Distribution/	
Availability Codes	
Avail and/or	
Dist	Special
A	

CONTENTS

TITLE	PAGE
PREFACE	1
ILLUSTRATIONS	3
TABLES	7
I. INTRODUCTION	9
II. BASIC CONCEPT	9
III. ANALYTICAL CHARACTERIZATION	14
A. ROSA Characterization	14
B. Gratings in OPS Systems	27
C. Grating and Aperture Transform Convolution	30
D. Geometry of ROSA Detectors	34
E. ROSA Sampling of Grating Spectra	44
IV. SIMULATING OPS DETECTION OF RONCHI GRATINGS	47
A. Program WRDET	47
B. Simulation Results	51
V. PRELIMINARY OPTICAL SUBSYSTEM DESIGN FOR GRATING MAP SYSTEMS	96
A. Basic Optical Subsystem Design	96
B. System Design Trade-Offs	98
VI. FABRICATION OF GRATING MAPS	107
A. Fabrication Requirements	107
B. The State of Technology	111
C. Further Discussion of System Design Trade-Offs	111
D. Extending the Storage Capacity of Grating Maps	116
VII. SYSTEMS CONCEPTS	117
A. Basic Subsystems	117
B. Example System Concepts	123
VIII. SUMMARY	130
IX. CONCLUSIONS	134

ILLUSTRATIONS

FIGURE	TITLE	PAGE
1	A Uniform Grating.	10
2	An Attribute Map and a Grating Map.	12
3	Optical Power Spectrum Sampling System Employing a ROSA Detector for Sampling Grating Maps.	13
4	ROSA Subsystems.	15
5	Analytical Characterization of ROSA Optical and Electronic Processing.	16
6	Amplitude of Circular Aperture Diffraction Patterns.	21
7	Optical Power Spectrum of a Circular Aperture.	22
8	Diffraction From a Circular Aperture.	23
9	Log-Linear Plot of Relative Intensity of a Circular Aperture Diffraction Pattern.	24
10	Fraction of the Total Energy Contained Within Circles of Prescribed Radii in the Diffraction Pattern of a Circular Aperture.	26
11	Cosine and Ronchi Grating Functions and Their Amplitude Fourier Transform Spatial Frequency Spectrums.	28
12	Convolving Amplitude Spectra From the Sampling Aperture and Grating to Yield a Detectable Intensity Spectrum.	33
13	Face Plates of Two ROSA Detectors.	35

ILLUSTRATIONS Continued

FIGURE	TITLE	PAGE
14	Spatial Frequency-Radial Distance Relation in the Back Focal Plane of a Transform Lens.	38
15	Linear Plot of Mid-Ring Radii for Two ROSA Detectors.	40
16	Semi-Log Plot of Mid-Ring Radii for Two ROSA Detectors.	41
17	Linear Plot of Detector Ring Width for Two ROSA Detectors.	42
18	Semi-Log Plot of Detector Ring Width for Two ROSA Detectors.	43
19	Flow Chart of the Main Components of Program WRDET.	48
20	Flow Chart of Subroutine AIRYD.	50
21	ROSA Simulation Results. A	56
22	ROSA Simulation Results. B	57
23	ROSA Simulation Results. C	58
24	ROSA Simulation Results. D	59
25	ROSA Simulation Results. E	60
26	ROSA Simulation Results. F	61
27	ROSA Simulation Results. G	62
28	Generalized Ring and Wedge Models.	67

ILLUSTRATIONS Continued

FIGURE	TITLE	PAGE
29	Three General Cases for Estimating Bessel Function Energy Incident on a ROSA Wedge Detector Element.	68
30	Eighteen Special Cases for Estimating Bessel Function Energy Incident on a ROSA Wedge Detector Element.	69
31	ROSA Simulation Results. H	73
32	ROSA Simulation Results. I	74
33	ROSA Simulation Results. J	75
34	ROSA Simulation Results. K	76
35	ROSA Simulation Results. L	77
36	ROSA Simulation Results. M	78
37	Example for S/N Less Than 1.0.	82
38	Signal-to-Noise Plots. A.	84
39	Signal-to-Noise Plots. B	85
40	Plots of Selected Data From Table 14.	87
41	ROSA Simulation Results. N	92
42	ROSA Simulation Results. O	93
43	ROSA Simulation Results. P	94
44	The f/D vs ρ (radius from optical axis) for Two Selected Bessel Zeros and Two Laser Wavelengths.	103

ILLUSTRATIONS Continued

FIGURE	TITLE	PAGE
45	Gratings Placed Before and After Transform Lenses.	106
46	Generating the Grating Map.	108
47	Optical Arrangements for Stationary Light Beam OPS Systems.	118
48	One- and Two-Dimensional Telecentric Beam-Scanning Arrangements Using Laser.	120
49	Optical Arrangements Using Parabolic Mirrors. Analogous to Figure 47 for Scanning Telecentric Beams.	121
50	Addition of a Photodiode Array Detector to Enable "Seeing" of the Image Sampled by the OPS Detector.	124
51	Concepts for Multiple-Coordinated Factor Map Gratings.	125
52	Example of an OPS Configuration Using a Spatial Light Modulator, a Rotating K Mirror, and a One-Dimensional Photodiode Array Detector.	126
53	Example of an OPS Configuration Using a Spatial Light Modulator, a Two-Dimensional Scanner and a Two-Dimensional Photodiode Array Detector.	126
54	A Simple Automated OPSA System for Reading Optically Stored MGI Factor Maps.	128
55	Program Associated With Automated OPSA System in Figure 54.	130

TABLES

NUMBER	TITLE	PAGE
1	Aperture-Diameter Scaling of Bessel Function.	25
2	ROSA Detector, Model WRD-6420.	36
3	ROSA Detector, Model WRD-6400.	37
4	Intensity Scaling Factors.	52
5	Summary of Simulation Conditions With Illustration and Data Page References.	53
6	Diameters Between Zero-Order Bessel Functions, Zeros for Delected Transform Lens Focal Lengths and Sampling Aperture Diameters.	63
7	Summary of Ronchi Grating Deltas for 177.8-mm Transform Lens Focal Length (Detector WRD-6420).	65
8	Summary of Ronchi Grating Deltas for 100.0-mm Transform Lens Focal Length (Detector WRD-6420).	66
9	Occurrences of Special Cases Shown in Figure 30 when Program WRDET Simulated Wedge Detection for ROSA Detector Model WRD-6420.	70
10	Detector Elements With $S/N > 1$ in Data Set 1A. (Detector WRD-6400).	72
11	Summary of Ronchi Grating Deltas for 177.8-mm Transform Lens Focal Length (Detector WRD-6400).	79
12	Summary of Ronchi Grating Deltas for 100.0-mm Transform Lens Focal Length (Detector WRD-6400).	80
13	Detector Elements With $S/N > 1$ in Data Set 1B. (Detector WRD-6400).	83
14	S/N for Ronchi Grating Deformations, $f = 100.0$ mm, $D = 0.1$ mm, (Detector WRD-6400).	86

TABLES Continued

NUMBER	TITLE	PAGE
15	S/N for Ronchi Grating Deformations, $f = 100.0$ mm, $D = 0.1$ mm, (Detector WRD-6400).	88
16	S/N For Grating Rotations From Wedge Bisector, $f = 100.0$ mm, $D = 0.1$ mm, (Detector WRD-6420).	90
17	Summary for a ROSA-Type Detector With Equal Ring Widths.	91
18	Detector Elements With $S/N > 1$ in Data Set 3A. (Equal Ring Width Detector).	95
19	Sampling Aperture Diameters Projected Onto Map and Ground Surface For Selected Map Reduction Ratios.	99
20	Common Gas Lasers and Their Associated Wave- lengths.	101
21	Equivalent Sampling Aperture Diameters For Selected Laser Wavelengths.	102
22	ROSA Detector (WRD-6420) Mid-Ring Spatial Frequencies For Four Laser Wavelengths.	104
23	Parameters For Grating Map Recorders.	110
24	Examples of Grating Recording Systems.	112
25	Example Worksheet For Selection of Grating Detection System Parameter Values.	115

OPTICAL POWER SPECTRAL ANALYSIS FOR MACHINE-READABLE FACTOR MAPS

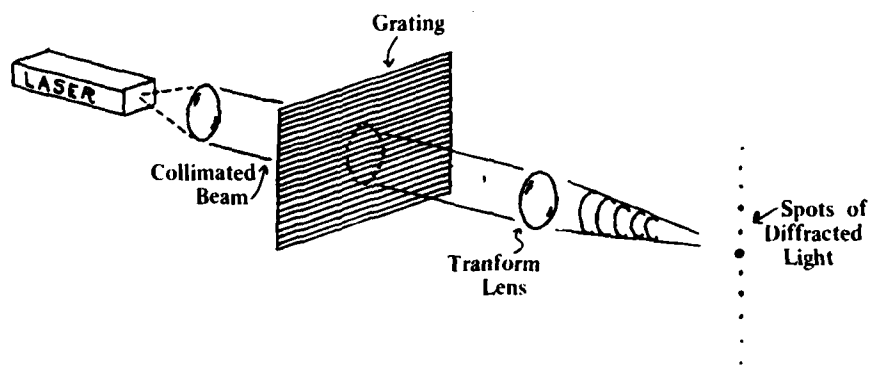
I. INTRODUCTION

A preliminary investigation of the application of Optical Power Spectral Analysis (OPSA) approaches to machine-readable factor maps for use in terrain information systems is presented. The objective is to offer a more compact, simpler, and cheaper data base storage and retrieval system than would be available by all-digital technology. In the basic concept of the systems, OPSA is used to decode data from reduced factor maps that have been encoded by spatial frequency and direction of optical gratings.

Alternative concepts to high-priced, large volume, and relatively slow digital mass storage systems for operation in the field are few. For this reason, a preliminary study of the application of OPSA was conducted in depth. The basic concept of optical coding and OPSA decoding of terrain factor maps is presented in Chapter 2. Chapter 3 contains an analytical characterization of the OPSA sampling system and its use in detection of Ronchi gratings. Chapter 4 presents a digital simulation program and simulation results from its use under a range of operational parameters. The preliminary design of an optical subsystem for detection of grating maps is developed in Chapter 5 to show how the interaction of parameters forces the designer to make trade-offs for realistic optical system specification. In Chapter 6 the technology for producing grating maps is reviewed and approaches for extending capabilities to produce gratings with increased storage capacity are outlined. Chapter 7 outlines more general system concepts which integrate optical, electronic, digital, and storage and retrieval subsystems and an example of a grating detection system is described to illustrate subsystem interactions. Chapter 8 presents the conclusions.

II. BASIC CONCEPT

If we insert a uniform grating in a collimated coherent light beam, as in figure 1, at the back focal plane of the transform lens, we will detect a number of collinear light spots. The spacing of the light spots will be determined by the grating frequency and type of grating, with the intensity of the spots related to the type of grating. The orientation of the line of spots will be perpendicular to the direction of the linear grating. If we change the grating, the spots will change accordingly in the back focal plane of the lens.



Note: This Uniform grating is illuminated by a collimated coherent light beam that results in collinear diffraction spots in the back focal plane of the transform lens.

FIGURE 1. A Uniform Grating.

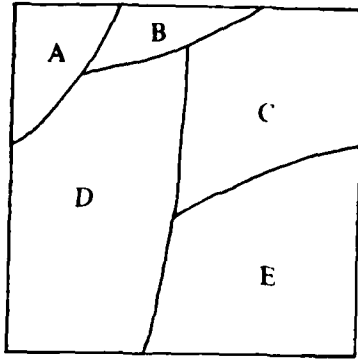
Knowing the type of grating employed in the optical system, we can determine without error the grating frequency and orientation by taking a few simple measurements on the light spots.

Now consider a simplified attribute map as shown in figure 2, wherein each bounded area is a two-dimensional representation of a range of one or more properties coded by an alphanumeric character. Decoding is accomplished by reading the description associated with the character code in the map's legend. Within each area having the same character code, the properties are expected to have the same range of values, and discontinuities occur only at boundary lines between coded areas. The example of an attribute map in Military Geographic Intelligence (MGI) is, of course, the terrain factor map where separate maps code surface configuration, surface composition, vegetation, etc.

Instead of alphanumeric character codes, we can use grating codes as shown in figure 2 with the boundaries retained. The code symbols are now a two-tuple (w, ϕ) , with w representing an element or the discrete set of spatial frequencies, $w \in W$, and ϕ representing an element of the discrete set of grating directions, $\phi \in \theta$.

The grating map of figure 2 can be a film transparency with the grating lines having a high optical density and the space between the grating lines having a low optical density. If the optical grating map is placed in the optical power spectrum sampling system shown at the top of figure 3, that part of the grating illuminated by the collimated coherent light beam passing the sampling aperture will result in spots of diffracted light, as indicated in figure 1. When a Recording Optical Spectrum Analyzer (ROSA) detector that has 32 ring detector elements and 32 wedge detector elements with (see figure 3) each element providing an electrical output signal is centered on the optical axis in the back focal plane of the transform lens, the diffracted light spots from any grating will result in a set of detected signals for those elements so illuminated.

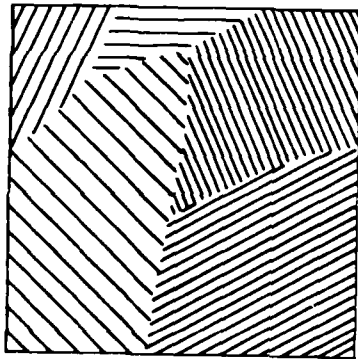
The remainder of this report will show that the grating codes can be optimally designed so that when they are encoded in an optical grating map and used in a properly designed optical system the result is several hundred unique coding classes for each map sheet. Each possible pair vector has a unique address in a computer lookup table.



ATTRIBUTE MAP

Legend:

- A _____
- B _____
- C _____
- D _____
- E _____



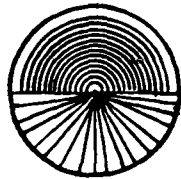
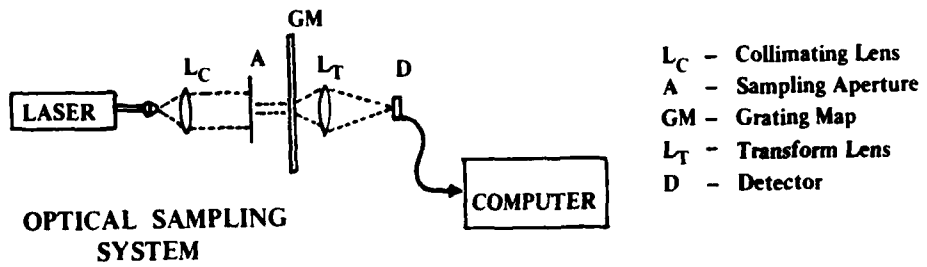
GRATING MAP

Legend:

-  _____
-  _____
-  _____
-  _____
-  _____

Note: The attribute map is coded with alphanumeric characters and the grating map has attributes coded with gratings of different spatial frequency and direction.

FIGURE 2. An Attribute Map and a Grating Map.



DETECTOR:

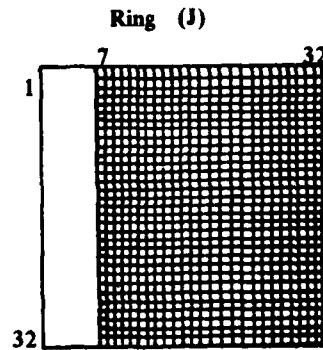
- 32 Ring Detectors
- 32 Wedge Detectors

Ring Detectors Provide Spatial Frequency Data

Wedge Detectors Provide Directional Data

COMPUTER LOOK-UP TABLE

$C(I,J)$ $I = 1,32$ $J = 7,32$



$32 \times 26 = 832$ coding classes

FIGURE 3. Optical Power Spectrum Sampling System Employing a ROSA Detector for Sampling Grating Maps.

III. ANALYTICAL CHARACTERIZATION

In this chapter the analytical characterization of ROSA and the theoretical aspects of OPSA as applied to optical gratings and their detection will be discussed. This material will serve as a background for subsequent discussions involving a computer simulation program that will demonstrate grating discrimination potential with ROSA systems and involving the design of grating detection systems. The ROSA system hardware has been previously reported,¹ and the system's use for automated pattern recognition research is documented in several publications.^{2,3,4}

The approach used here should not be considered rigorous, but rather more intuitive so as to provide a reader without a background in OPSA with enough foundation to understand the relation of the design variables and the nature of the trade-offs to achieve a useful operational system.

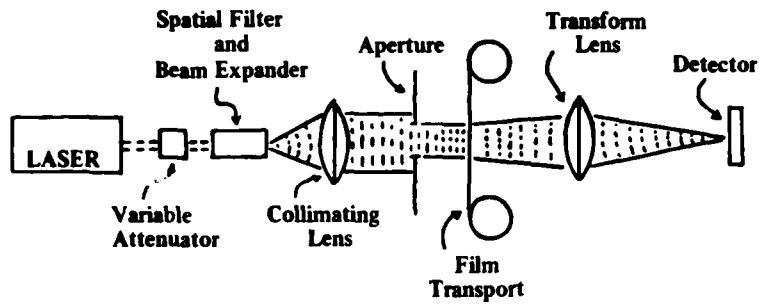
A. ROSA Characterization • The three ROSA subsystems are indicated in figure 4. Here we will be concerned with the signals produced by optical sampling and the nature of the electronic signal processing in the ROSA system. The signal flow and analytical characterization of the optical and electronic signal processing within the ROSA is summarized in figure 5. We will now develop the expressions shown in this illustration.

¹R. D. Leighty, *Optical Power Spectrum Analysis (OPSA) (Report No. 1, Recording Optical Spectrum Analyzer System Hardware)*, U. S. Army Engineer Topographic Laboratories, Fort Belvoir, VA, Report ETL-TR-74-11, May 1975, AD-A016 131.

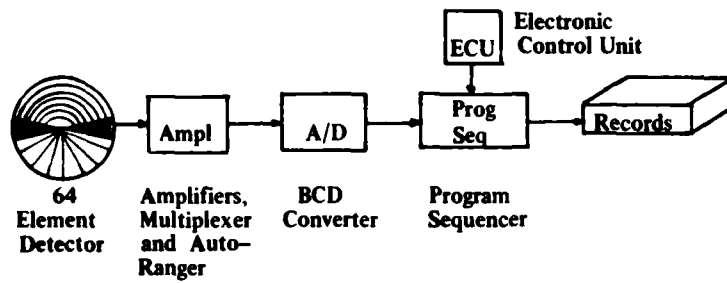
²R. D. Leighty, and G. F. Lukes, "Cloud Screening From Aerial Photography," *Proc. 40th Annual Meeting ASP/ACSM*, St. Louis, MO, 1974, pp 309-332.

³G. F. Lukes, "Cloud Screening from Aerial Photography Applying Coherent Optical Pattern Recognition Techniques," *Proc. SPIE, Coherent Optics in Mapping*, Vol. 45, 1974, pp 265-272.

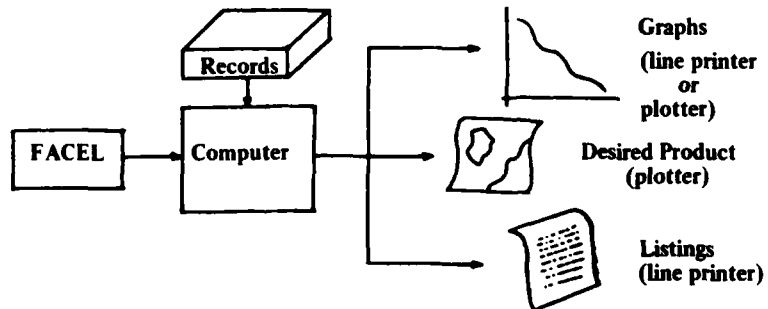
⁴G. E. Lukes, "Rapid Screening of Aerial Photography by OPS Analysis," *Proc. SPIE, Data Extraction From Film*, Vol. 117, 1977, pp 89-97.



A. Coherent optical system configuration

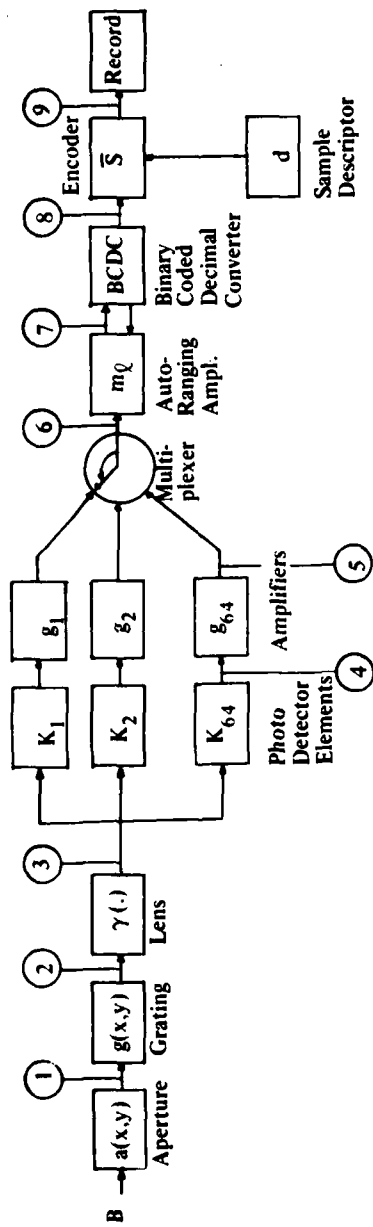


B. Electronic processing and record system



C. Software processing and output

FIGURE 4. ROSA Subsystems.



- ① $a(x, y)$
- ② $a(x, y)g(x, y) = h(x, y)$
- ③ $\int \int_{x, y} h(x, y) \exp [j(xu + yv) / (f\lambda)] dx dy = H(u, v)$
- ④ $K_n \int \int_{\rho, \theta} |H(\rho, \theta)|^2 \rho d\rho d\theta, n = 1, 64$
- ⑤ $K_n g_n \int \int_{\rho, \theta} \rho d\rho d\theta = z_n$
- ⑥ $\{z_n\}_{n = 1, 64}$
- ⑦ $\{m_\ell z_n\}_{\ell = 0, 3} = \{z_n\}, n = 1, 64$
- ⑧ $\{(z_n / 10^\ell, 3 - \ell)_m\} = \{s_n\}, \ell = 0, 3, n = 1, 64$
- ⑨ $\{d, \{s_j\}_{j = 1, 8, i}\}_{i = 1, 8} = \{S\}_i$

FIGURE 5. Analytical Characterization of ROSA Optical and Electronic Processing.

The circular sampling aperture $a(x, y)$ of radius r is centered on the optical axis. When illuminated by normally incident coherent plane waves of amplitude B and wavelength λ , the aperture has a transmission function

$$a(x, y) = \begin{cases} B, & \text{if } \sqrt{x^2 + y^2} \leq r \\ 0, & \text{otherwise} \end{cases} \quad (1)$$

The light from the aperture is then modulated and diffracted by the transmission function $g(x, y)$ of the grating transparency to yield $h(x, y)$, such that

$$h(x, y) = a(x, y) g(x, y) \quad (2)$$

The diffraction-limited, transform lens of focal length f and diameter, D_1 , where $D_1 \gg r$, then images the Fraunhofer diffraction pattern of $h(x, y)$ in its back focal plane. This process is equivalent to a two-dimensional Fourier transformation $F(h(x, y))$ except for a constant phase factor, which has no effect upon the results. Thus,

$$F(h(x, y)) = H(u, v) = \frac{1}{\lambda f} \iint_{x, y} a(x, y) g(x, y) \exp[-j2\pi(xu + yv)/(\lambda f)] dx dy \quad (3)$$

where (u, v) represents space coordinates in the detector or focal plane. To express $H(u, v)$ in terms of spacial frequencies w_u and w_v , use

$$w_u = \frac{u}{\lambda f} \quad \text{and} \quad w_v = \frac{v}{\lambda f} \quad (4)$$

Thus, $H(u/\lambda f, v/\lambda f) = H(w_u, w_v)$.

The detector is responsive only to light intensity, and the intensity distribution at the photo detector is equivalent to the squared modulus of the light amplitude, or

$$I(u, v) = |H(u, v)|^2 \quad (5)$$

Now consider each of the $n = 1,64$ photo detector elements to have response K_n for incident light energy. The signal for any detector element is then a function of the element surface area and the responsivity of the material. At this point, u and v can be expressed in polar coordinates, where $\phi = \sqrt{u^2 + v^2}$ and $\theta = \tan^{-1}(v/u)$. Therefore, the signal from any detector element is

$$K_n \int_{\rho_n} \int_{\theta_n} |H(\rho, \theta)|^2 \rho \, d\rho d\theta, \quad n = 1, 64 \quad (6)$$

where ρ_n and θ_n represent both the lower and upper limits for each element considered in the integral.

Each of the signals next passes through two amplifier stages, the first has constant gain g_n^a with adjustable bias c_n^a , and the second has variable gain g_n^b with an adjustable bias c_n^b . The net amplification being

$$g_n = (g_n^a - c_n^a) z_n + c_n^b \quad (7)$$

Signals z_n at the output of these amplifiers are then

$$z_n = g_n K_n \int_{\rho_n} \int_{\theta_n} |H(\rho, \theta)|^2 \rho \, d\rho d\theta \quad (8)$$

The multiplexer steps through each of the n channels to form the set $\{z_n\}$, $n = 1, 64$. Next, the signals pass to an autoranging amplifier linked to a binary-coded decimal converter. The amplifier has four gains m_p , $p = 0, 3$, determined by the position of the most significant digit in the converter. Final output of the amplifier is then

$$\{m_p z_n\} \quad p = 0, 3 = q_n, \quad n = 1, 64 \quad (9)$$

where

$$m_p = \begin{cases} m_0 = 2 \times 10^0, & \text{if } 10^4 < z_n < 10^5 \\ m_1 = 2 \times 10^1, & \text{if } 10^3 < z_n < 10^4 \\ m_2 = 2 \times 10^2, & \text{if } 10^2 < z_n \leq 10^3 \\ m_3 = 2 \times 10^3, & \text{if } z_n \leq 10^2 \end{cases} \quad (10)$$

and output from the converter is then the three most significant digits and the decimal characteristic. Thus,

$$\{S_n\} = (q_n / 10^p, 3-p), \quad p = 0, 3, \quad n = 1, 64 \quad (11)$$

The encoder then reformats $\{s_n\}$ into eight groups of numbers for recording, along with a six-digit decimal sample descriptor number d input by the operator from the control unit and card number $i = 1, 8$. The output data is then a set of eight card images

$$\{S\}_i = \{d, \{S_j\}_{j=1,8}, i\}_{i=1,8} \quad (12)$$

from which the sample vector $\bar{S} = \{s_n\}$, $n = 1, 64$ is available for the computer pattern recognition efforts.

Establishing an optimum set of values for the optical and electronic parameters, i.e. aperture diameter, transform lens focal length, amplifier gains, etc., to obtain the best sample vector \bar{S} for the grating patterns to be investigated is dependent on knowledge of the effects on the output data owing to variables in the analytical expressions just discussed. This point is aptly illustrated when reviewing the optical power spectrum analysis literature to find that authors do not recognize the effects of the sampling aperture on the output data. In equation (3), the sampling aperture $a(x, y)$ is assumed to have a spatially uniform or constant value in a finite area. It is this finite area that sets the integration limits with the result that equation (3) is termed the superposition integral, which reflects spatial frequency domain convolution. If $a(x, y)$ and $g(x, y)$ have respectively the Fourier transforms $A(u, v)$, and $G(u, v)$, then equation (3) can be expressed in the spatial frequency domain by

$$H(u, v) = \frac{1}{\lambda f} A(u, v) ** G(u, v) \quad (13)$$

where the double asterisk symbolizes the two-dimensional convolution operation, which in integral form is

$$H(u, v) = \frac{1}{\lambda f} \iint A(\alpha - u, \beta - v) G(u, v) \, d\alpha d\beta \quad (14)$$

Thus, $A(u, v)$ is convolved with $G(u, v)$ having a smoothing effect, and the amount of smoothing is inversely related to the aperture diameter.

Aperture effects on detection of gratings are of considerable importance for our problem. Therefore, we will provide many illustrations related to diffraction patterns resulting from circular apertures. These illustrations and their underlying concepts will be referenced frequently in the following discussions. $A(\rho)$ is represented by the first-order Bessel function, often referred to as the Airy function. Hereafter, this will be referred to as the Bessel function. Thus

$$A(\rho) = \beta\pi \frac{D^2}{4} \left[\frac{2J_1(\pi\rho D/\lambda f)}{(\pi\rho D/\lambda f)} \right] \quad (15)$$

where ρ is the spatial frequency variable and D is the sampling aperture diameter. In figure 6, the amplitude distribution for circular aperture diffraction patterns is shown for two values for aperture diameter, and associated with each of these patterns are three values of transform lens focal length. The intensity pattern of $A(\rho)$,

$$A(\rho)^2 = \frac{B^2 \pi^2 D^4}{16} \left[\frac{2J_1(\pi\rho D/\lambda f)}{(\pi\rho D/\lambda f)} \right]^2 \quad (16)$$

is pictured in figure 7 for an aperture of arbitrary diameter. In figure 8, the relation of the intensity function to the amplitude function without weighting is indicated. Note that the intensity function is definitely positive. If we plot the intensity function semi-logarithmically as in figure 9, this presentation will clearly depict the intensity function's relation to the logarithmic exposure response of a photographic emulsion as shown in figure 7. If the aperture diameter is decreased, the rings in figure 7 would be further spaced as shown in figure 6, indicating a higher degree of spatial smoothing in equation (14). This spacing is significant when small aperture diameters are required to sample the grating maps so as to retain the boundary definition within some tolerable minimum effective ground-sampling diameter. The scaling effects for five small sampling apertures and two different transform lens focal lengths are shown in table 1. Note the decrease in the first zero crossing (point 2) with increasing aperture diameter. In figure 10 is shown the fraction of the total energy contained within circles of prescribed radii in the diffraction pattern of a circular aperture. Approximately 84 percent of the energy lies within the central lobe of the Bessel function. Therefore, to minimize smoothing effects, this first zero crossing must be as small as possible, i.e. the diameter of the sampling aperture must be as large as possible. Also, note that the amplitude values for the maximums and minimums of the Bessel functions in table 1 have not been scaled for aperture area according to equation (15).

From equation (3) the effect of the lens focal length f and the monochromatic wavelength λ will inversely affect the amplitude of the output as well as the scale of the presentation on the detector.

The optical power spectrum has polar symmetry as indicated in equation (5) since $I(u, v) = I(-u, -v)$. This redundancy allows use of the ring and wedge geometry in design of the ROSA detector without any loss of information.

Detector element responses K_n are a function of the respective receptive areas as well as the element's responsivity. Thus, all wedges, being of the same area, are expected to have the same response for a given constant responsivity; whereas, the responses for rings will increase with radius from the center. If the second stage amplifier gain g_n^b in (7) is adjusted so that

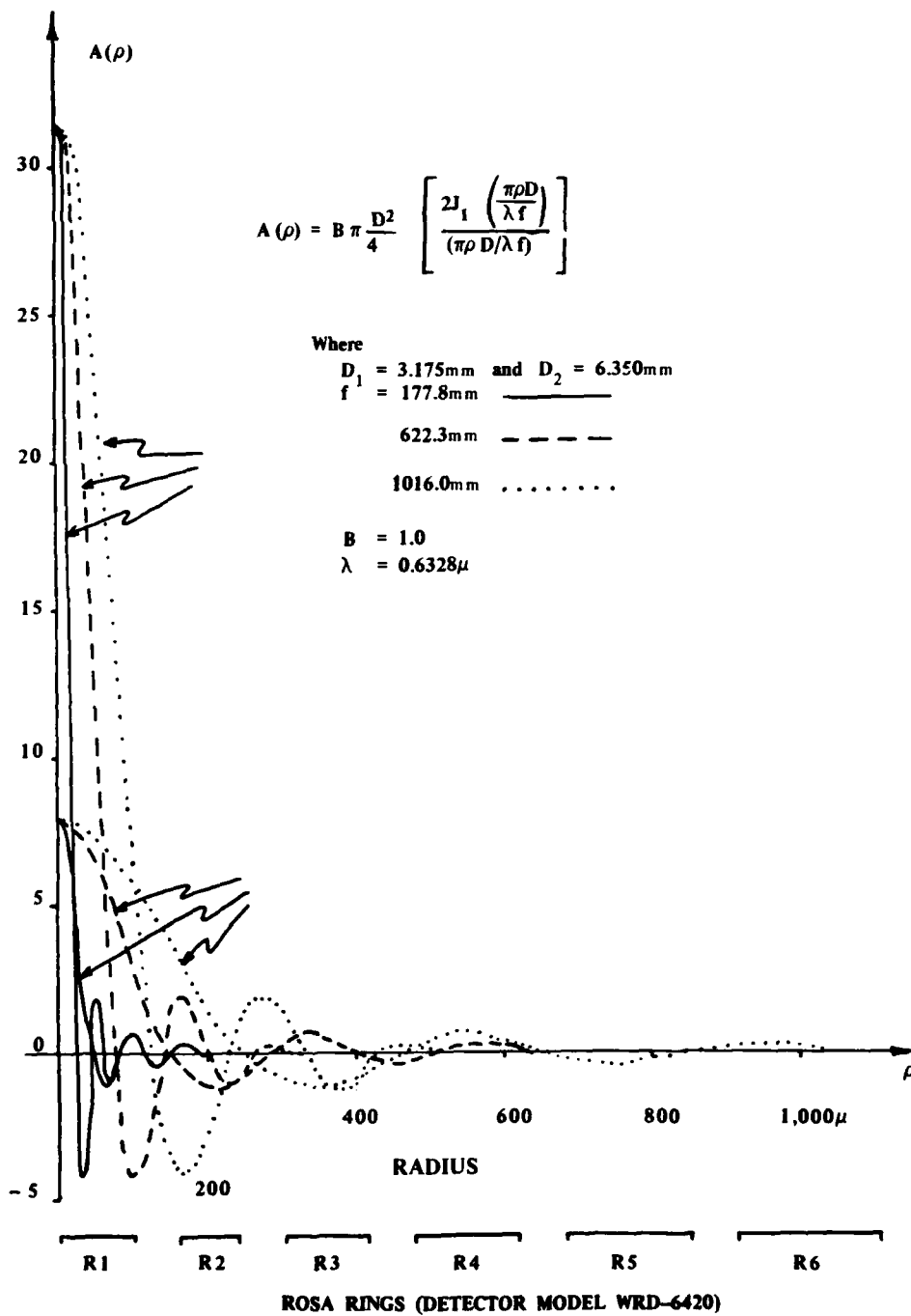


FIGURE 6. Amplitude of Circular Aperture Diffraction Patterns.

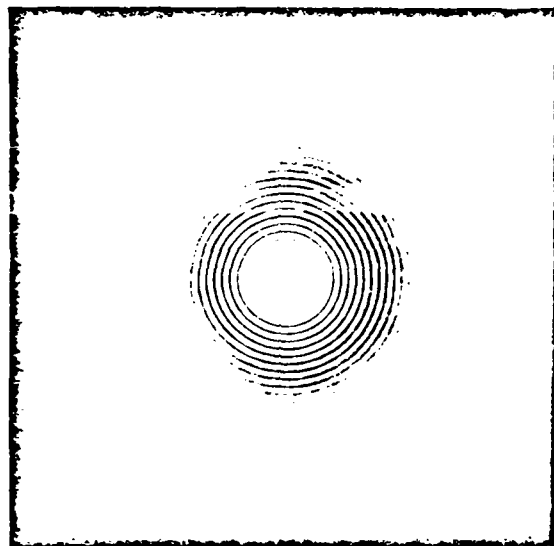


FIGURE 7. Optical Power Spectrum of a Circular Aperture.

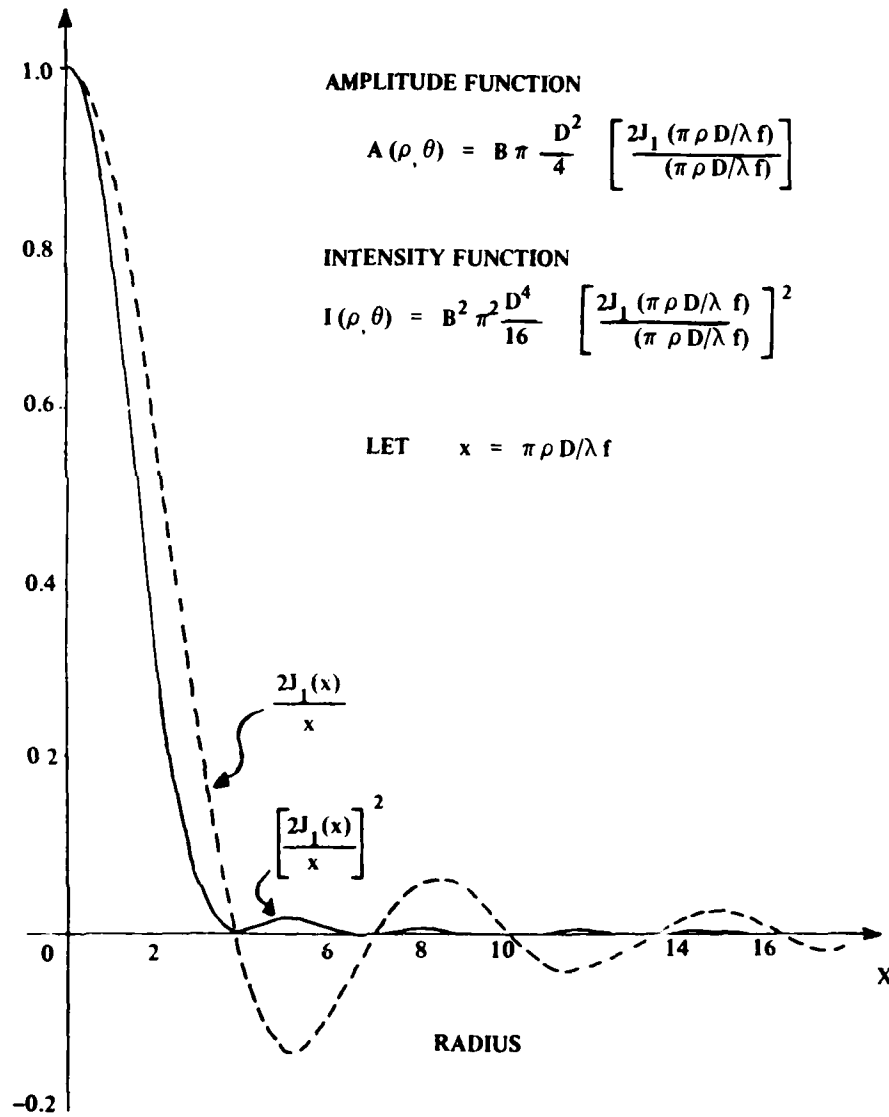
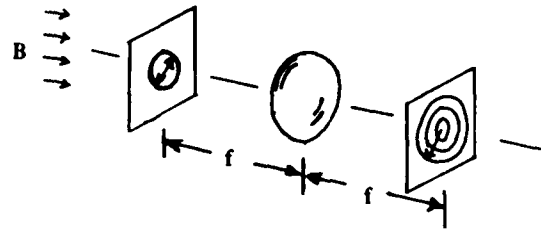


FIGURE 8. Diffraction From a Circular Aperture.

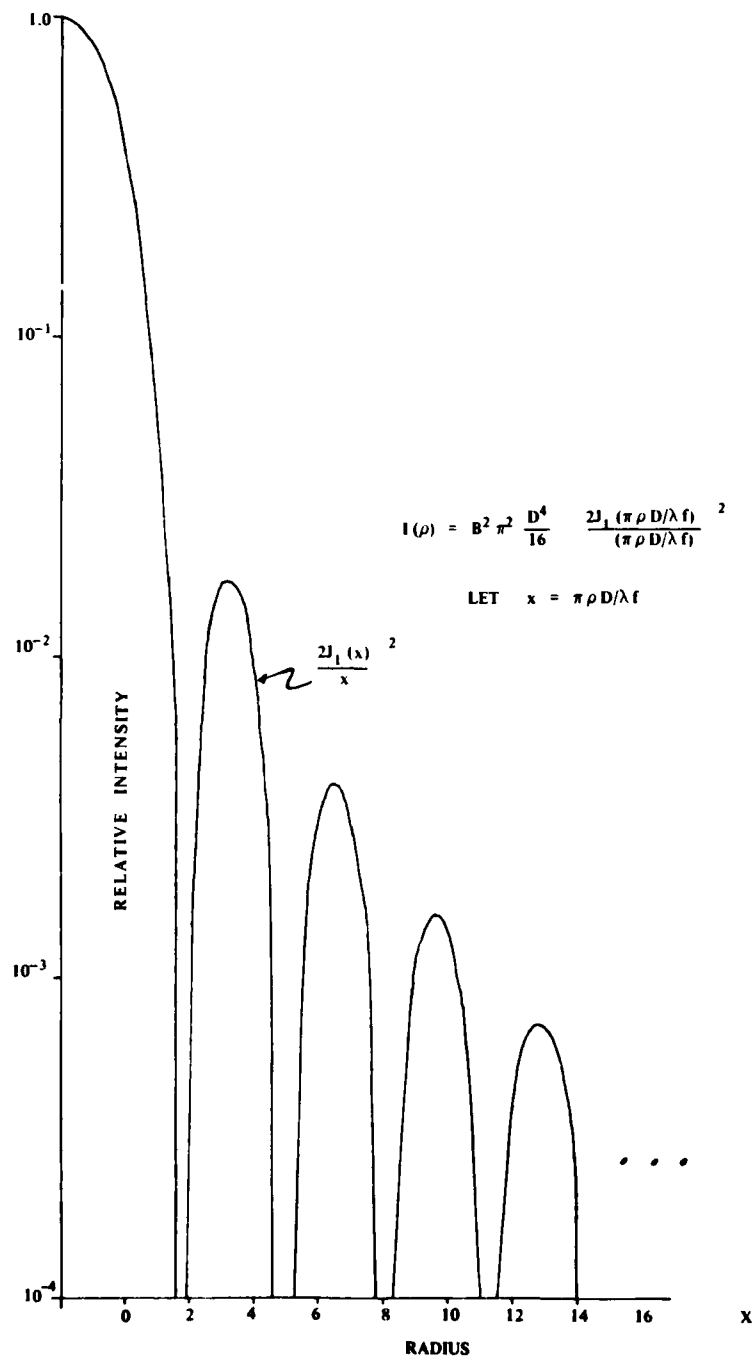


FIGURE 9. Log-Linear Plot of Relative Intensity of a Circular Aperture Diffraction Pattern.

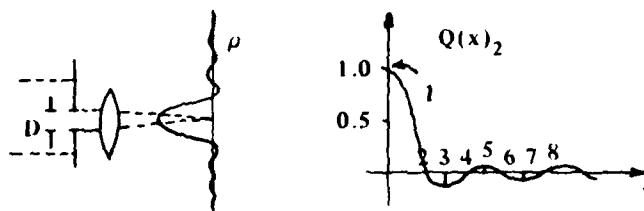


TABLE 1. Aperture-Diameter Scaling of Bessel Function.

LET

$$Q(x) = \frac{2J_1(\pi \rho D/\lambda f)}{(\pi \rho D/\lambda f)}$$

WHERE

$$x = \pi \rho D/\lambda f$$

$$\rho = \frac{x \lambda f}{\pi D} \text{ and if } C_i = X_i/\pi$$

$$\text{Then } \rho = C_i \frac{\lambda f}{D}$$

DISTANCE FROM OPTICAL AXIS, ρ in mm.

$$f = 177.8 \text{ mm}, \quad \lambda = 0.6325 \times 10^{-3} \text{ mm}$$

APERTURE DIAMETER, D in mm.

i	C_i	$Q(x)$	0.075	0.10	0.25	0.50	0.75	1.00
1	0.0	+1.000	0	0	0	0	0	0
2	1.220	0	1.830	1.373	0.549	0.275	0.183	0.137
3	1.635	-0.1323	2.453	1.870	0.734	0.368	0.245	0.187
4	2.233	0	3.350	2.512	1.005	0.502	0.335	0.251
5	2.679	+0.0648	4.019	3.014	1.206	0.603	0.402	0.301
6	3.238	0	4.858	3.643	1.457	0.729	0.486	0.364
7	3.699	-0.0400	5.549	4.162	1.665	0.832	0.555	0.416
8	4.241	0	6.362	4.772	1.909	0.954	0.636	0.477

$$f = 1000.0 \text{ mm}, \quad \lambda = 0.6328 \times 10^{-3} \text{ mm}$$

APERTURE DIAMETER, D in mm.

i	C_i	$Q(x)$	0.075	0.10	0.25	0.50	0.75	1.00
1	0.0	+1.000	0	0	0	0	0	0
2	1.220	0	1.029	0.772	0.309	0.154	0.103	0.077
3	1.635	-0.1323	1.380	1.035	0.414	0.207	0.138	0.104
4	2.233	0	1.884	1.413	0.565	0.283	0.188	0.141
5	2.679	+0.0648	2.260	1.695	0.678	0.339	0.226	0.170
6	3.238	0	2.732	2.049	0.820	0.410	0.273	0.205
7	3.699	-0.0400	3.121	2.341	0.936	0.468	0.312	0.234
8	4.241	0	3.578	2.683	1.073	0.537	0.358	0.268

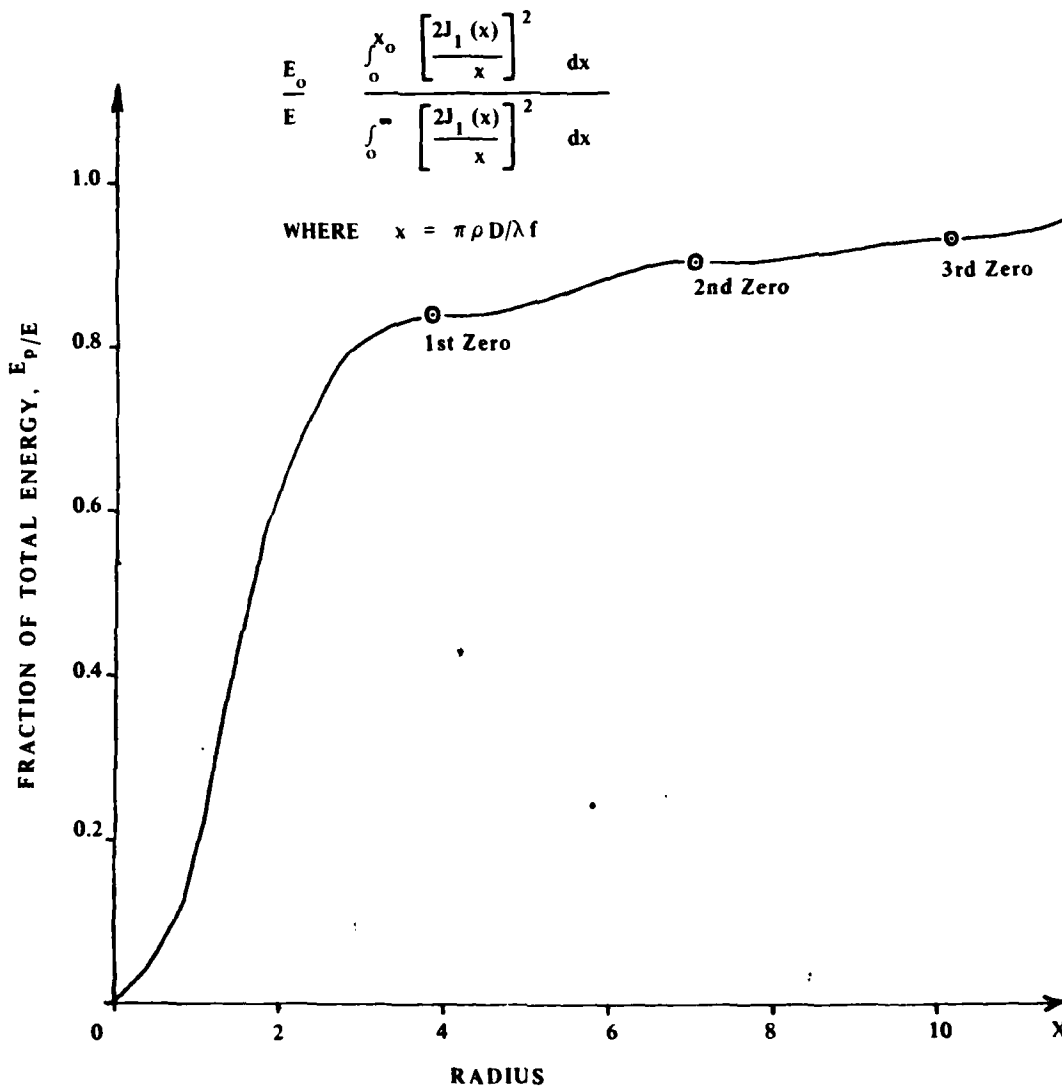


FIGURE 10. Fraction of the Total Energy Contained Within Circles of Prescribed Radii in the Diffraction Pattern of a Circular Aperture.

$$|g_n^d + c_n^d| = |g_n^h + c_n^h| \quad (17)$$

then the responsivity differences of detector elements is ignored. Although if $g_n =$ constant, i.e. if the outputs from all second-stage amplifiers are equal, then detector element areas are normalized. However, the flexibility exists with software to adjust data for desired area response; thus, the former approach is generally used in practice.

B. Gratings in OPS Systems • A transmission grating will be defined as a one-dimensional repeating optical transmission function. For example,

$$g(x, y) = g(x) = A \cos(2\pi x/p) \quad (18)$$

is a cosine function of amplitude A in the x -direction that repeats every p units of x , and the value of the function at any point x is the same for all values of y . The spatial frequency of a grating in line pairs per millimeter (mm) is the reciprocal of the grating period in millimeters, i.e.

$$w = 1/p \quad (19)$$

The Fourier transform of $g(x)$ is $G(w)$, which will be symbolized as shown in equation (3), i.e. $F[g(x)] = G(w)$. As in equation (18) where the grating can be expressed in one dimension, it is frequently advantageous to present expressions as $F[g(x, y) = g(x)] = G(u, \phi) = G(p, \theta)$, where p is a radial distance and θ is a direction angle. Since the grating transform for a specific grating will have $\theta =$ a constant, we can then talk in general of $G(p, \theta_1) = G(p)$. By equation (4), we have $w = p/\lambda f$, thus $G(p/\lambda f) = G(w)$.

As shown in figure 11, the Fourier transform for a cosine grating is equal to two delta functions, $\delta(w \pm 1/p)$, with amplitudes of $A/2$ positioned at $\pm 1/p$ in the spatial frequency presentation. This results from the equality

$$\cos(w_0 x) = \frac{e^{jw_0 x} + e^{-jw_0 x}}{2}, j^2 = -1$$

and since $F[e^{jw_0 x}] = \delta(w - w_0)$, where $w_0 = 1/p$ in $1/p$ mm, we have for equation (18)

$$F[A \cos(2\pi x/p)] = A/2 [\delta(w - 1/p) + \delta(w + 1/p)] \quad (20)$$

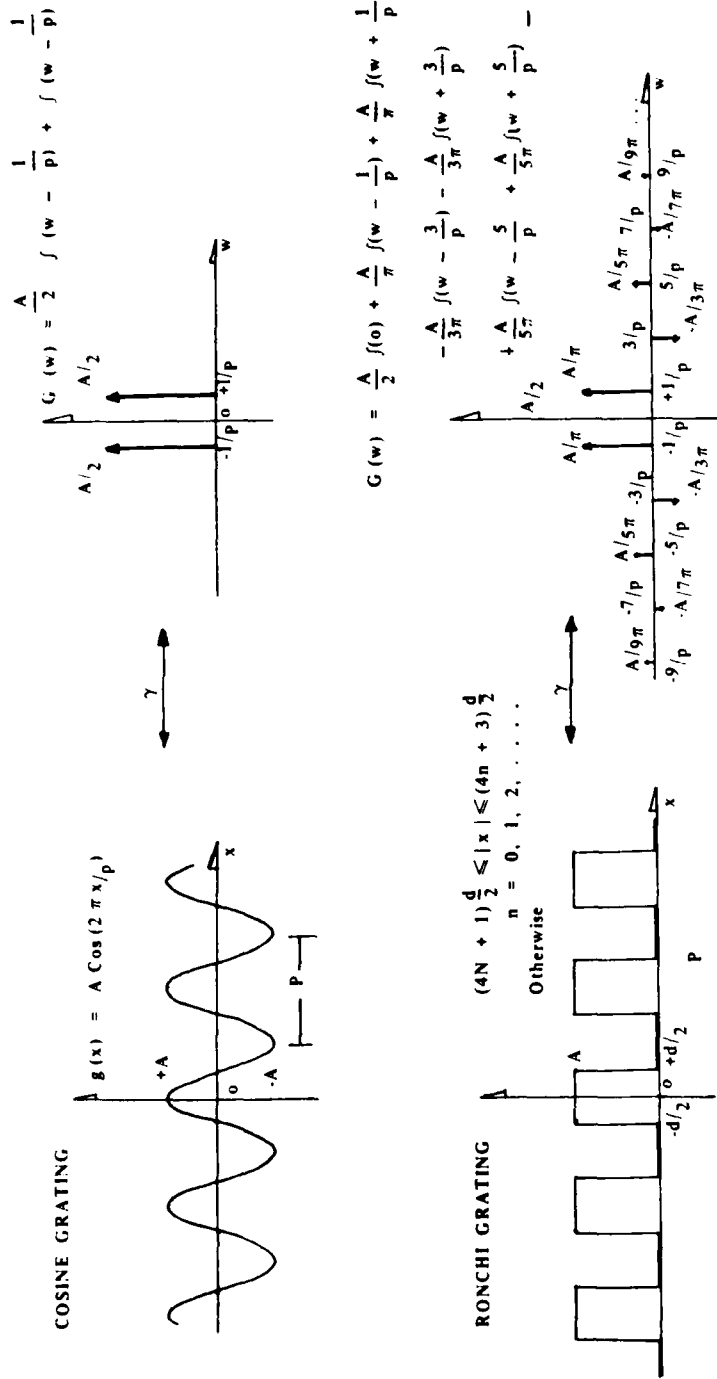


FIGURE 11. Cosine and Ronchi Grating Functions and Their Amplitude Fourier Transform Spatial Frequency Spectrums.

A few words about delta functions is necessary. A delta function $\delta(t)$, also known as a unit impulse function, may be defined in many ways. Here the following definition will be used:

$$\delta(t) = \begin{cases} 0, & \text{if } t \neq 0 \\ \infty, & \text{if } t = 0 \end{cases} \quad (21)$$

$$\int_{-\infty}^{\infty} \delta(t) dt = \int_{-\epsilon}^{\epsilon} \delta(t) dt = 1, \epsilon > 0$$

The first relation indicates that $\delta(t)$ is zero except at $t = 0$, where it becomes infinite in such a way that the second relation is satisfied. Delta functions have many useful mathematical properties, which we will only reveal as needed to clarify the concepts under discussion.

Delta functions in optics are point sources of light; and since the cosine grating has only two delta functions, each of which has infinite resolution in the frequency domain, it would appear that this grating would be ideal for OPSA applications such as we are investigating. Indeed, if we had means for fabricating cosine gratings of selected spatial frequencies with the desired spatial boundary conditions, it would be ideal; unfortunately we do not.

A square wave grating would be much simpler to realize, except that we cannot obtain negative light values with optical transparencies. We can however use a 'Ronchi' grating, which is a square wave grating with a positive $A/2$ bias.

Another unique characteristic of a Ronchi grating is that the grating width, d , is one-half of the grating period, p . The disadvantage of using Ronchi gratings instead of cosine gratings is that harmonic delta functions are found in the Fourier transform, as shown in figure 11. These harmonics decrease in amplitude with increasing spatial frequency and alternate plus and minus in amplitude. To obtain the functional expression for Ronchi grating transforms, we use the Fourier series representation for a square wavetrain with a constant bias. Using the Fourier series results in an infinite number of coefficients. An infinite number of cosine waves are required to realize perfect square waves, but if we select the first n coefficients, where n is a modest number, we can transform each Fourier series term and the result is that each Fourier series term has its unique delta function in the spatial frequency domain.

By using Ronchi gratings, we trade simplicity of grating fabrication for complexity in detection of the grating transforms. We will show that the detection of ideal Ronchi gratings can be made at sufficiently high signal-to-noise ratios to yield unique signals for OPSA applications.

C. *Grating and Aperture Transform Convolution.* • Equation (14) is the convolution integral for a general signal function, $G(u, v)$, and a general aperture function, $A(u, v)$. In this section we will be more specific and use grating functions and small circular sampling aperture functions. The objective is to indicate the nature of the resulting function indicated by equation (14) when parameter values of the aperture and grating function are varied.

To introduce the concepts with minimum complexity, we will first assume that a cosine grating is illuminated by a collimated, coherent light beam passing through a circular sampling aperture. We will rewrite equation (14) in one-dimensional form as

$$H(w) = \frac{1}{\lambda f} \int_{-\infty}^{\infty} A(a) G(w - a) da$$

Now substitute equations (15) and (20)

$$H(w) = \frac{1}{\lambda f} \int_{-\infty}^{\infty} B\pi \frac{D^2}{4} \frac{2J_1(\pi a D/\lambda f)}{(\pi a D/\lambda f)} \frac{A}{2} [\delta(w - 1/p - a) + \delta(w + 1/p - a)] da$$

With the relation,

$$F(w) * \delta(w - w_0) = \int_{-\infty}^{\infty} (a - w_0) F(a) da = F(w_0)$$

Then,

$$H(w) = \frac{1}{\lambda f} \frac{AB\pi D^2}{8} \left[\frac{2J_1(\pi(w-1/p)D/\lambda f)}{(\pi(w-1/p)D/\lambda f)} + \frac{2J_1(\pi(w+1/p)D/\lambda f)}{(\pi(w+1/p)D/\lambda f)} \right] \quad (22)$$

Expression (22) tells us that convolving an optical cosine grating transform with the first-order Bessel function, which is the transform of the aperture function, is equivalent to creating two new first-order Bessel functions with one positioned at the spatial frequency $1/p$, and the other at $-1/p$. The Bessel functions will have their same spatial frequency distribution as that of the aperture function, but will be scaled by a factor of one-half in amplitude. Another important revelation of expression (22) is the potential for significant interaction between the two Bessel functions resulting from the convolution. We have seen from figure 6 and table 1 how the Bessel function is scaled in spatial frequency inversely with the diameter of the sampling aperture. Then, for very small sampling apertures and low spatial frequency gratings, one could expect to have overlapping Bessel functions that add algebraically to yield a net amplitude spectrum somewhat different than that of the individual Bessel functions. We will show examples of these implications in the simulations to follow.

Using the results of expression (22) as a guide, we can easily extrapolate to a simple expression for an ideal Ronchi grating illuminated by collimated, coherent light passing through a circular sampling aperture. The major differences between the expressions that result from the differences between the cosine transform function and the Ronchi grating transform function are as indicated earlier, and as shown in figure 11. The infinite expression for Ronchi grating convolution is then more complicated in appearance and is given by

$$\begin{aligned}
H(w) = & \frac{B\pi D^2}{4\lambda f} \frac{A}{2} \frac{2J_1(\pi w D/\lambda f)}{(\pi w D/\lambda f)} + \frac{A}{\pi} \frac{2J_1(\pi(w-1/p)D/\lambda f)}{(\pi(w-1/p)D/\lambda f)} \\
& + \frac{A}{\pi} \frac{2J_1(\pi(w+1/p)D/\lambda f)}{(\pi(w+1/p)D/\lambda f)} - \frac{A}{3\pi} \frac{2J_1(\pi(w-3/p)D/\lambda f)}{(\pi(w-3/p)D/\lambda f)} \\
& - \frac{A}{3\pi} \frac{2J_1(\pi(w+3/p)D/\lambda f)}{(\pi(w+3/p)D/\lambda f)} + \dots \quad (23)
\end{aligned}$$

This convolution is indicated in figure 12. Note the net amplitude spectrum resulting from the individual overlapping Bessel amplitude spectra. Since only the intensity spectrum is detectable, the bottom of figure 12 shows the intensity spectrum to be the magnitude squared of the net amplitude spectrum, as indicated in equation (6). Thus,

$$I(w) = |H(w)|^2 \quad (24)$$

To understand the intensity function of equation (24) in terms of the individual Bessel function in equation (23), we will generalize (23) to

$$\begin{aligned}
H(w) = K & [A_1 J(w) + A_2 J(w + w_1) + A_2 J(w - w_1) \\
& - A_3 J(w + 3w_1) - A_3 J(w - 3w_1) + \dots] \quad (25)
\end{aligned}$$

The first term within the parenthesis is a Bessel function centered on the optical axis, the second and third terms represent the positive and negative first harmonics, respectively, and the fourth and fifth terms represent the positive and negative third harmonics. Higher order terms have been omitted from equation (25).

When (25) is squared, as in (24), interaction terms result.

$$\begin{aligned}
H^2(w) = & K^2 [A_1^2 J^2(w) + A_2^2 J^2(w + w_1) + A_2^2 J^2(w - w_1) \\
& - A_3^2 J^2(w + 3w_1) - A_3^2 J^2(w - 3w_1) + \dots \\
& + A_1 A_2 J(w) J(w + w_1) + A_1 A_2 J(w) J(w - w_1) \\
& - A_1 A_3 J(w) J(w + 3w_1) - A_1 A_3 J(w) J(w - 3w_1) \\
& - A_2 A_3 J(w + w_1) J(w + 3w_1) - A_2 A_3 J(w - w_1) J(w - 3w_1) \\
& + \dots] \quad (26)
\end{aligned}$$

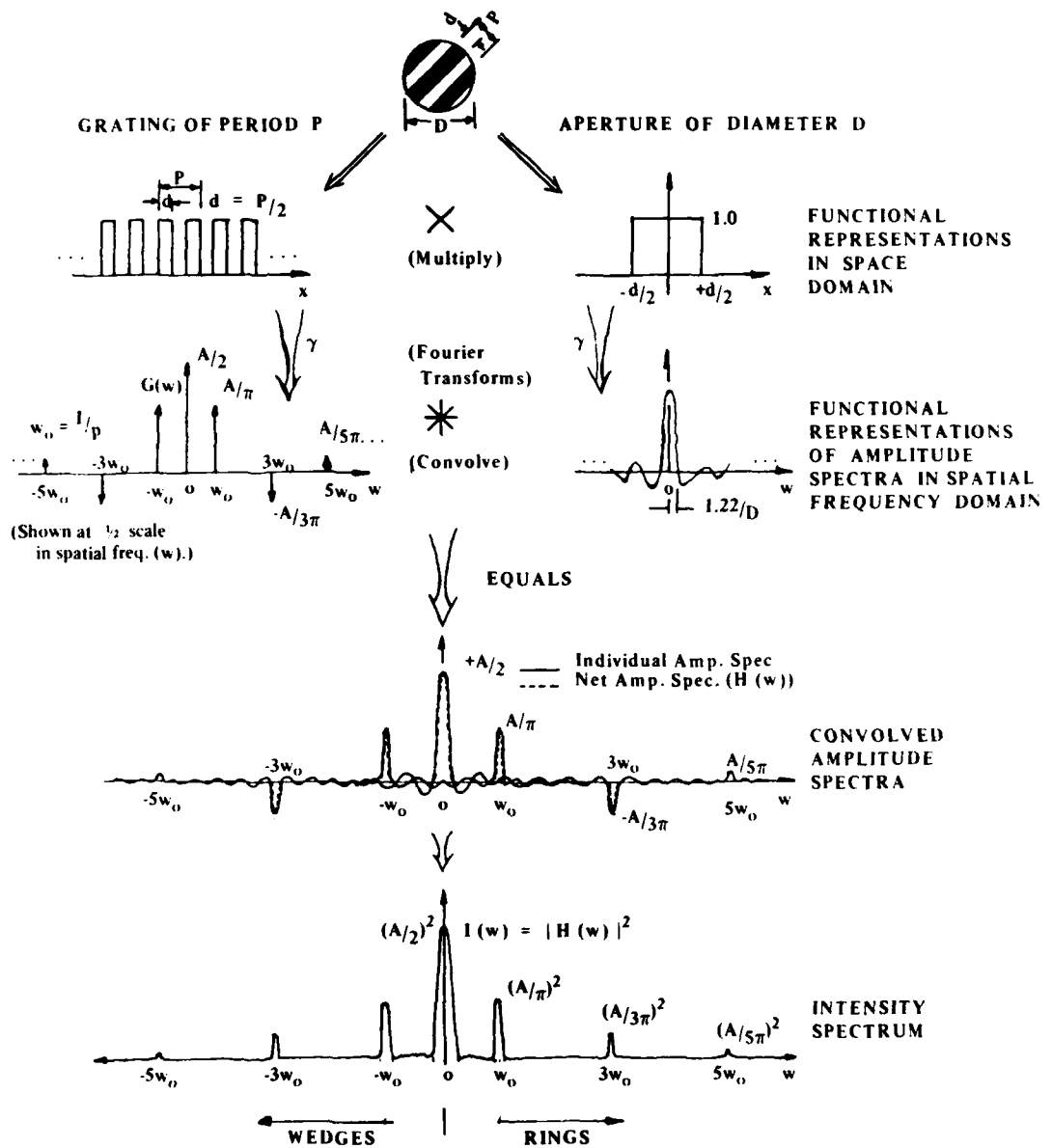


FIGURE 12. Convolution of Amplitude Spectra From the Sampling Aperture and Grating to Yield a Detectable Intensity Spectrum.

The significance of the interaction terms is dependent upon the scaling of the Bessel function, as dictated by the size of the sampling aperture and the focal length of the transform lens, and upon the positioning of the functions as determined by the Ronchi grating frequency, w_1 . If the sampling aperture is large, the interaction terms will be insignificant; but when the sampling aperture is small and the grating frequency is small, then some of the interaction terms can be significant. This will be discussed later.

It should be noted that (23) implies that the Ronchi grating is a real function, i.e., has no phase components. In practice this is never fully realized, and the effects include even-order harmonics. This will be discussed subsequently.

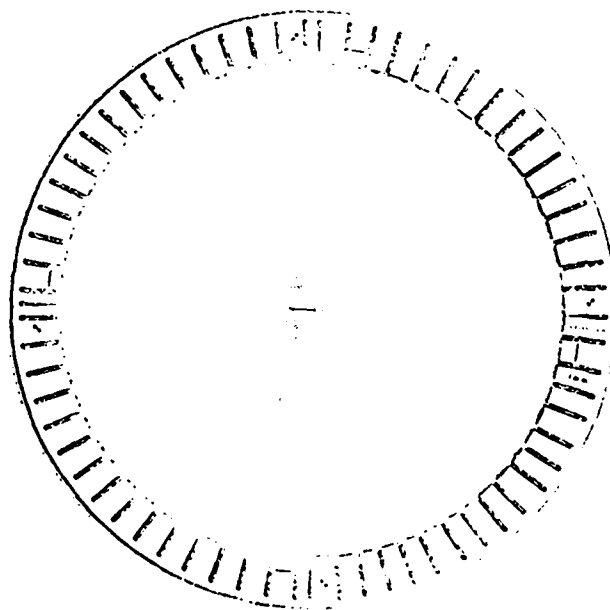
D. Geometry of ROSA Detectors. • Equation (23) indicates the nature of the amplitude signal on the detector. Here we describe the geometrical nature of ROSA detectors that will partition or sample the incident grating spectra, and the following section will discuss the sampling of grating spectra.

Two ROSA detector models are available from Recognition Systems Inc., each has 32 ring elements and 32 wedge elements; however, the detectors have some major differences. The detection of Ronchi gratings was simulated for both detectors with slightly different results that are better understood with a knowledge of the detectors and their differences.

The older detector, Model WRD-6420, has two 20° scratch wedges (usually oriented normal to the direction of roll-film travel in a manner such that emulsion scratches will not yield false diffraction signals), and the newer detector, Model WRD-6400, has no scratch wedges. The face plates of these detectors is shown in figure 13. Table 2 lists the dimensions of the ROSA Model WRD-6420 detector and table 3 presents similar data for the Model WRD-6400 detector. In both tables, the data is presented for each detector ring element. The least and maximum radius and their radial difference give the dimensions of the concentric detector rings that integrate incident energy. For each ring, the mid-radius is a key dimension in the later simulations because the gratings will be designed to have their first harmonic positioned at the mid-radius. The tables indicate the spatial frequencies associated with the mid-radii for four different focal length transform lenses. In figure 14, the relation is plotted between radial distance and spatial frequency in the back focal plane of these four lenses as given by equation (4). The remaining dimension shown in tables 2 and 3 concerns the wedge width at mid-radius. This dimension will be used to analyze grating direction detection in the simulations



a. Model WRD-6420



b. Model WRD-6400

FIGURE 13. Face Plates of Two ROSA Detectors.

TABLE 2. ROSA Detector, Model WRD-6420.

Ring No.	MEASUREMENTS IN mm.				Wedge Width	Radius Difference	Maximum Radius	Mid-Radius	MID-RING SPATIAL FREQUENCY (1/mm)		
	Least Radius	Mid-Radius	Maximum Radius	f = 1.774 mm/f					f = 1.774 mm/f	f = 1.774 mm/f	
1	0.0	-	0.1016	-	-	0.0747	-	-	1.75	0.52	0.32
2	0.1651	0.2045	0.2438	-	-	0.1119	0.2438	3.22	1.75	0.52	0.32
3	0.3373	0.3632	0.4131	-	-	0.1397	0.4131	5.74	2.23	0.56	0.36
4	0.4326	0.5525	0.6223	-	-	0.1676	0.6223	8.72	4.31	1.40	0.86
5	0.6253	0.7696	0.8534	-	-	0.1956	0.8534	12.17	6.85	1.95	1.20
6	0.9169	0.9147	1.1125	-	-	0.2186	1.1125	16.04	9.02	2.54	1.58
7	1.1760	1.2853	1.3285	-	-	0.2438	1.3285	20.31	11.43	3.26	2.00
8	1.4590	1.5739	1.7018	-	-	0.2667	1.7018	24.97	14.04	4.01	2.46
9	1.7653	1.8737	2.0320	-	-	0.2933	2.0320	30.01	16.87	4.82	2.86
10	2.0268	2.2435	2.3701	-	-	0.3223	2.3701	35.45	19.93	5.70	3.49
11	2.4663	2.6175	2.7626	-	-	0.3223	2.7626	41.36	23.26	6.65	4.07
12	2.8449	3.0074	3.1620	-	-	0.3251	3.1620	47.52	26.72	7.64	4.68
13	3.2461	3.4201	3.5941	-	-	0.3459	3.5941	54.05	30.39	8.69	5.32
14	3.6732	3.8557	4.0411	-	-	0.3728	4.0411	60.94	34.27	9.79	6.00
15	4.1173	4.3142	4.5110	-	-	0.3937	4.5110	68.17	38.34	10.96	6.71
16	4.5972	4.7943	5.0013	-	-	0.418	5.0013	75.76	42.61	12.17	7.46
17	5.0775	5.2372	5.5163	-	-	0.4374	5.5163	83.71	47.08	13.45	8.24
18	5.5331	5.8230	6.0522	-	-	0.4537	6.0522	92.02	51.75	14.73	9.06
19	6.1220	6.3703	6.6116	-	-	0.4826	6.6116	100.62	56.61	16.18	9.91
20	6.6878	6.9333	7.1907	-	-	0.5029	7.1907	109.66	61.67	17.62	10.79
21	7.2669	7.5311	7.7953	-	-	0.5284	7.7953	119.01	66.93	19.12	11.71
22	7.8715	8.1458	8.4201	-	-	0.5486	8.4201	128.73	72.40	20.69	12.67
23	8.4963	8.7908	9.0653	-	-	0.5690	9.0653	138.76	78.04	22.30	13.66
24	9.1415	9.4374	9.7333	-	-	0.5913	9.7333	149.13	83.88	23.97	14.68
25	9.8095	10.1169	10.4242	-	-	0.6147	10.4242	159.88	89.92	25.69	15.74
26	10.5004	10.8132	11.1379	-	-	0.6375	11.1379	170.97	96.16	27.47	16.83
27	11.2241	11.5431	11.8720	-	-	0.6579	11.8720	182.41	102.53	29.31	17.95
28	11.9482	12.2886	12.6289	-	-	0.6807	12.6289	194.20	109.21	31.21	19.11
29	12.7051	13.0569	13.4097	-	-	0.7036	13.4097	206.34	116.05	33.16	20.31
30	13.4849	13.8469	14.2028	-	-	0.7239	14.2028	218.82	123.07	35.16	21.54
31	14.2850	14.6584	15.0317	-	-	0.7467	15.0317	231.64	130.28	37.22	22.80
32	15.1079	15.4915	15.8750	-	-	0.7671	15.8750	244.80	137.69	39.34	24.10

NOTE:

Wedge detector elements have 5.0 wedge angle, inner radius is 1.176 mm and outer radius is 15.367 mm for all wedges.

TABLE 3. ROSA Detector, Model WRD-6400.

Ring No.	Least Radius	Max. Dis.	Maximum Radius	Radius Difference	Ring Angle	Wedge Width	f = 1000 mm	f = 277.5 mm	f = 422.3 mm	f = 1016.5 mm
1	0.12	0.153	0.258	0.106	35.00	-	2.33	1.62	0.46	0.28
2	0.147	0.181	0.311	0.127	35.00	-	4.44	3.62	0.71	0.44
3	0.174	0.215	0.374	0.159	35.00	-	6.55	5.39	0.96	0.59
4	0.201	0.249	0.447	0.206	35.00	-	8.66	7.27	1.22	0.75
5	0.228	0.283	0.520	0.276	35.00	-	10.77	9.19	1.48	0.91
6	0.255	0.317	0.593	0.366	35.00	0.057*	12.88	11.16	1.76	1.08
7	0.282	0.351	0.666	0.474	35.00	0.114	14.99	13.19	2.05	1.26
8	0.309	0.385	0.739	0.600	35.00	0.171	17.10	15.30	2.37	1.47
9	0.336	0.419	0.812	0.746	35.00	0.228	19.21	17.50	2.71	1.66
10	0.363	0.453	0.885	0.911	35.00	0.285	21.32	19.79	3.00	1.90
11	0.390	0.487	0.958	1.096	35.00	0.342	23.43	22.16	3.32	2.16
12	0.417	0.521	1.031	1.300	35.00	0.400	25.54	24.63	3.64	2.44
13	0.444	0.555	1.104	1.524	35.00	0.457	27.65	27.19	3.97	2.77
14	0.471	0.589	1.177	1.767	35.00	0.514	29.76	29.84	4.34	3.14
15	0.498	0.623	1.250	2.030	35.00	0.571	31.87	32.58	4.71	3.56
16	0.525	0.657	1.323	2.313	35.00	0.628	34.00	35.41	5.11	4.03
17	0.552	0.691	1.396	2.616	35.00	0.685	36.11	38.33	5.53	4.56
18	0.579	0.725	1.469	2.939	35.00	0.742	38.22	41.34	5.99	5.16
19	0.606	0.759	1.542	3.292	35.00	0.800	40.33	44.44	6.47	5.80
20	0.633	0.793	1.615	3.675	35.00	0.857	42.44	47.63	6.98	6.48
21	0.660	0.827	1.688	4.088	35.00	0.914	44.55	50.91	7.51	7.20
22	0.687	0.861	1.761	4.531	35.00	0.971	46.66	54.28	8.07	7.95
23	0.714	0.895	1.834	5.004	35.00	1.028	48.77	57.74	8.65	8.73
24	0.741	0.929	1.907	5.507	35.00	1.085	50.88	61.29	9.25	9.54
25	0.768	0.963	1.980	6.040	35.00	1.142	52.99	64.93	9.87	10.38
26	0.795	0.997	2.053	6.603	35.00	1.200	55.10	68.66	10.51	11.25
27	0.822	1.031	2.126	7.196	35.00	1.257	57.21	72.48	11.17	12.15
28	0.849	1.065	2.200	7.819	35.00	1.314	59.32	76.39	11.85	13.08
29	0.876	1.099	2.273	8.472	35.00	1.371	61.43	80.39	12.55	14.04
30	0.903	1.133	2.346	9.155	35.00	1.428	63.54	84.48	13.27	15.03
31	0.930	1.167	2.419	9.868	35.00	1.485	65.65	88.66	14.01	16.05
32	0.957	1.201	2.492	10.611	35.00	1.542	67.76	92.93	14.77	17.10
33	0.984	1.235	2.565	11.384	35.00	1.600	69.87	97.29	15.55	18.18
34	1.011	1.269	2.638	12.197	35.00	1.657	71.98	101.74	16.35	19.29
35	1.038	1.303	2.711	13.050	35.00	1.714	74.09	106.27	17.17	20.43
36	1.065	1.337	2.784	13.943	35.00	1.771	76.20	110.89	18.01	21.60
37	1.092	1.371	2.857	14.876	35.00	1.828	78.31	115.59	18.87	22.80
38	1.119	1.405	2.930	15.849	35.00	1.885	80.42	120.37	19.75	24.03
39	1.146	1.439	3.003	16.862	35.00	1.942	82.53	125.24	20.65	25.29
40	1.173	1.473	3.076	17.915	35.00	2.000	84.64	130.19	21.57	26.58
41	1.200	1.507	3.149	19.008	35.00	2.057	86.75	135.22	22.51	27.89
42	1.227	1.541	3.222	20.141	35.00	2.114	88.86	140.33	23.47	29.23

NOTE:

All wedge detector elements have 5.65 wedge angles, inner radius of wedge, 16 and 17 is 0.666 mm and all other wedges have inner radii of 5.54 mm, outer radii of all wedges are 15.90 mm.

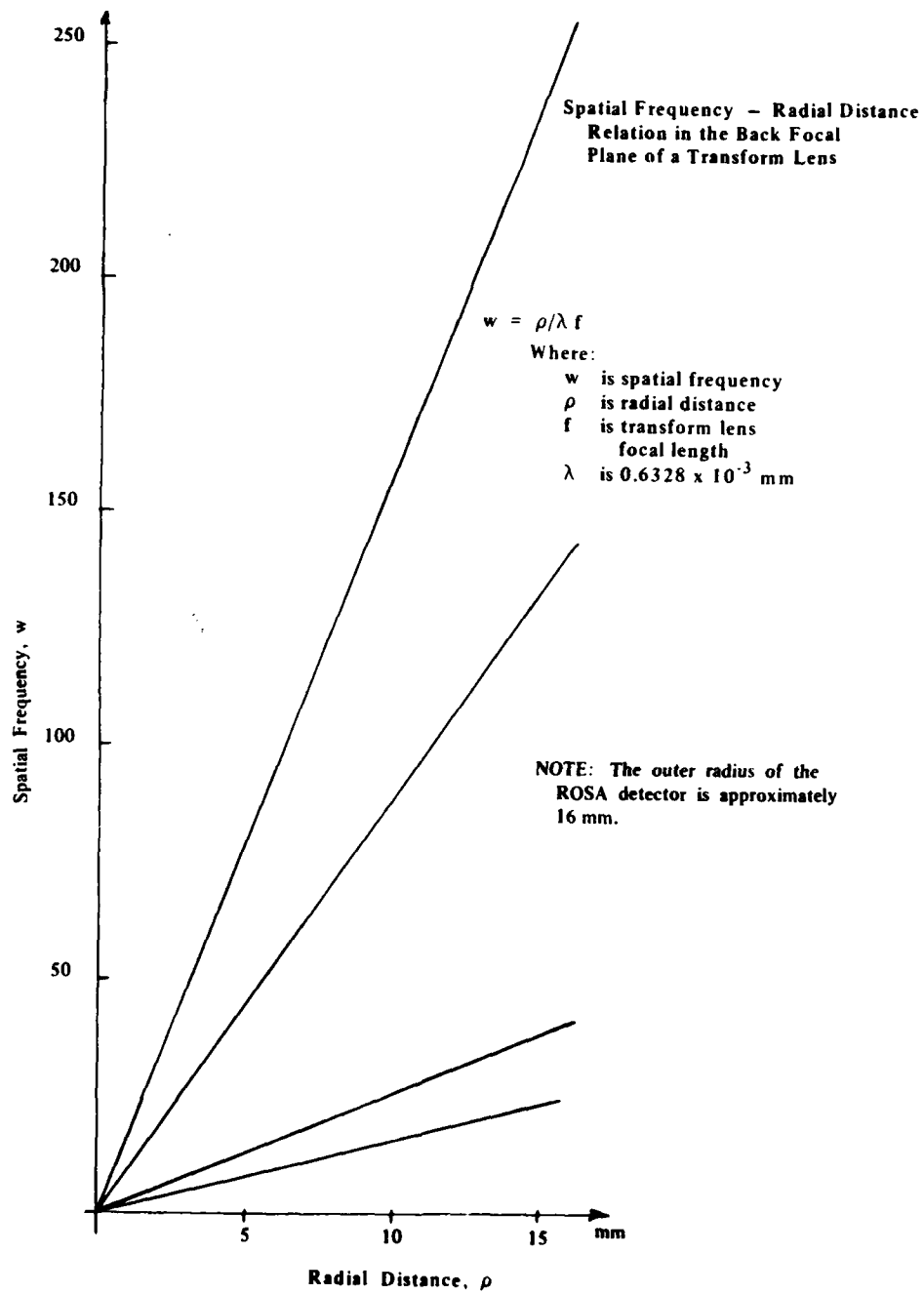


FIGURE 14. Spatial Frequency-Radial Distance Relation in the Back Focal Plane of a Transform Lens.

The wedge angles for the WRD-6420 detector are 5.000° , and the wedge angles for the WRD-6400 detector are 5.625° ; therefore, the wedge widths will be different for each detector.

Note that the inner radius for WRD-6420 detector wedges is 1.176 millimeter. Therefore, only ring-wedge combinations for rings 7 through 32 are available for grating detection. For the Model WRD-6400 detector, wedges have an inner radius of 0.544 millimeter, except for wedges 16 and 17, which have an inner radius of 0.660 millimeter corresponding to rings 6 and 7 respectively. The outer radius of the wedges for Model WRD-6420 detectors is 15.367 millimeters; whereas, the maximum radius for Ring 32 is 15.875 millimeters. This will have significance in later simulations. For the WRD-6400 detector, the outer wedge radius and the maximum radius for Ring 32 are all equal to 15.900 millimeters.

In figures 15 and 16, linear and semi-log plots of the mid-radii for the two detectors are presented. In general, figure 15 indicates that the WRD-6400 detector has greater frequency domain resolution than the WRD-6420 detector up to about Ring 20 and less resolution at higher spatial frequencies. Figure 16 indicates that the rings of detector WRD-6400 are spaced logarithmically beyond Ring 6. In figures 17 and 18, linear and semi-log plots of the ring widths for the two detectors are presented. Here figure 17 shows the ring widths for the WRD-6420 detector to increase in a linear manner; whereas, those of the WRD-6400 detector are shown to be nonlinear. In the semi-log plot of figure 18, both are quasi semi-log in nature, but with different slopes.

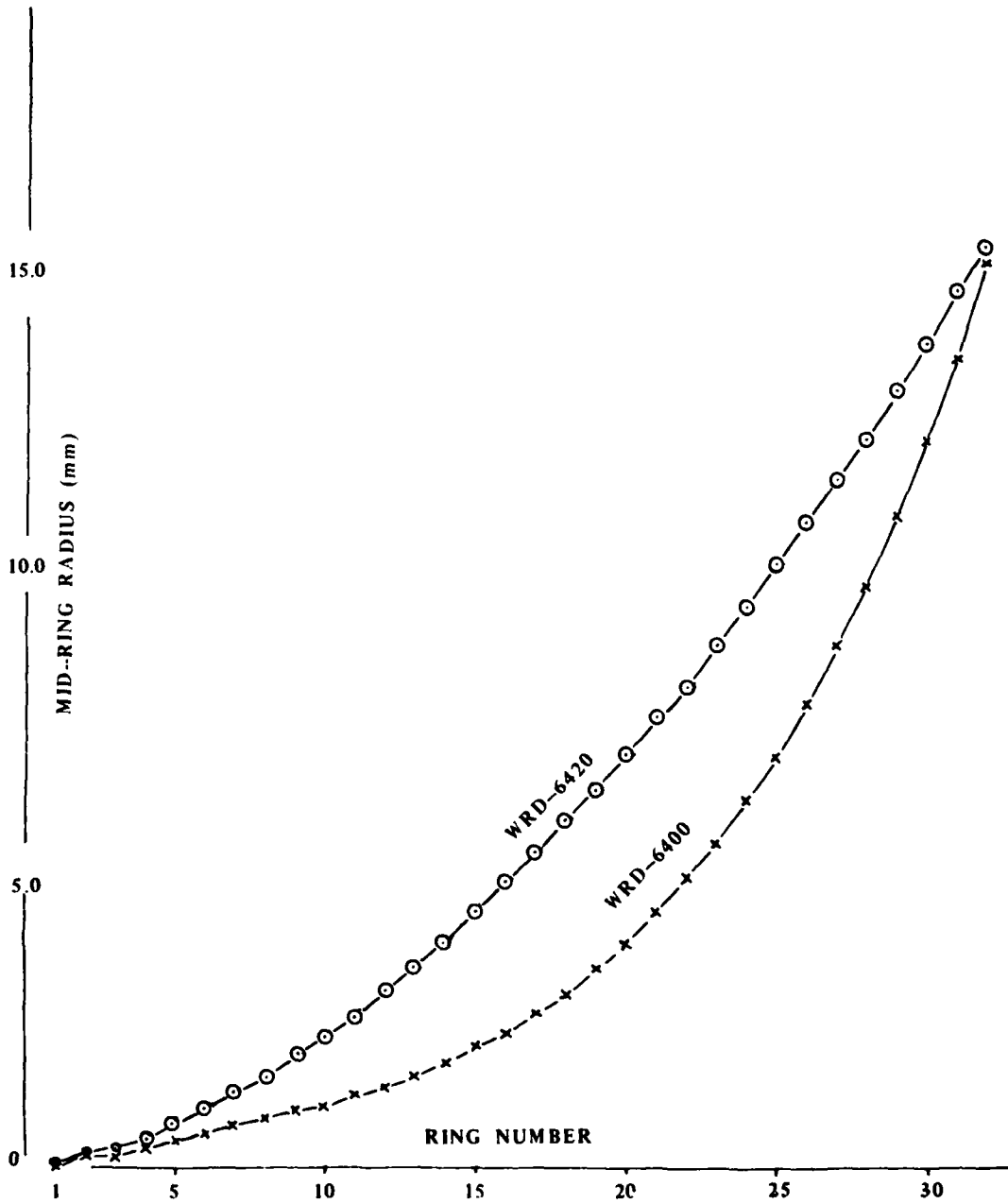


FIGURE 15. Linear Plot of Mid-Ring Radii for Two ROSA Detectors.

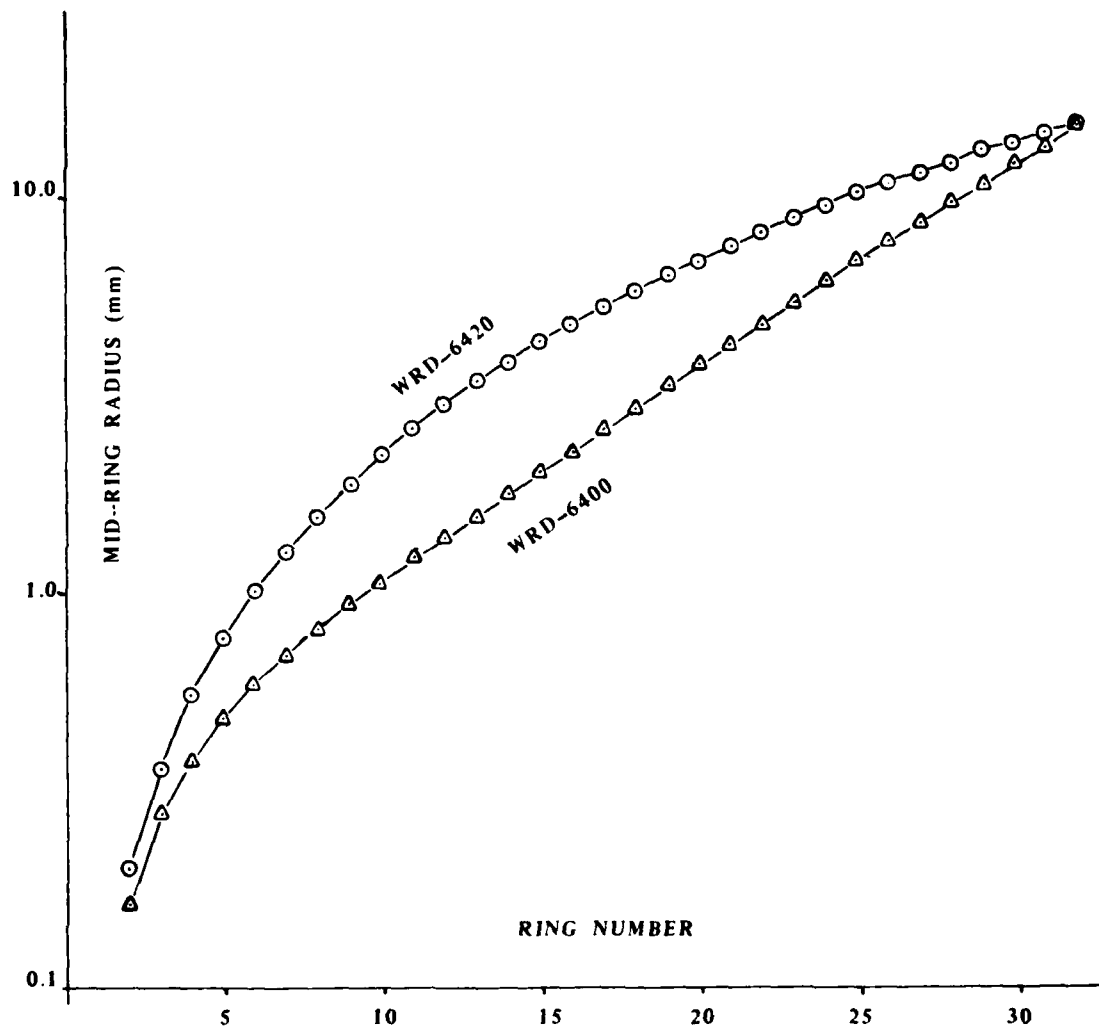


FIGURE 16. Semi-Log Plot of Mid-Ring Radii for Two ROSA Detectors.

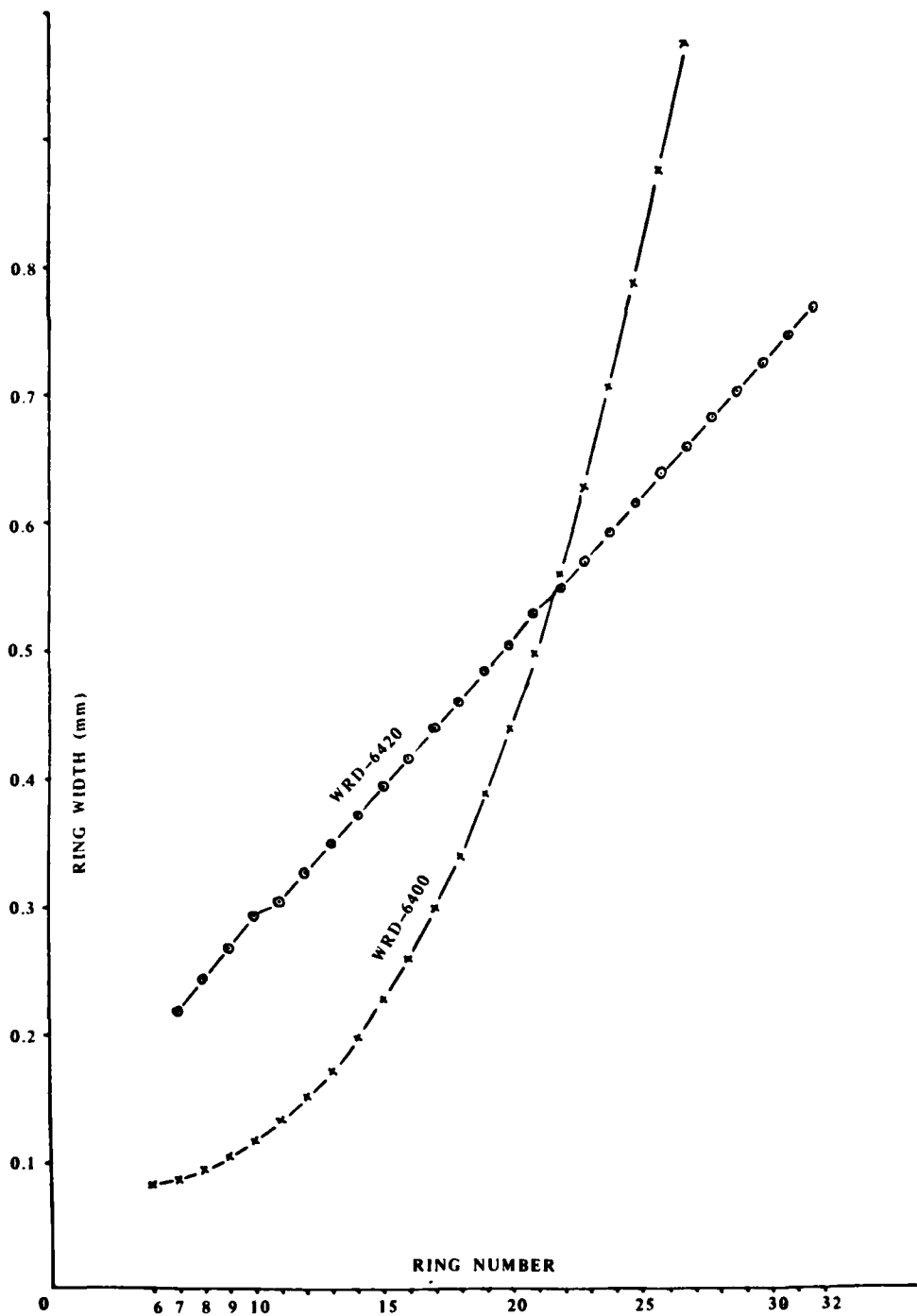


FIGURE 17. Linear Plot of Detector Ring Width for Two ROSA Detectors.

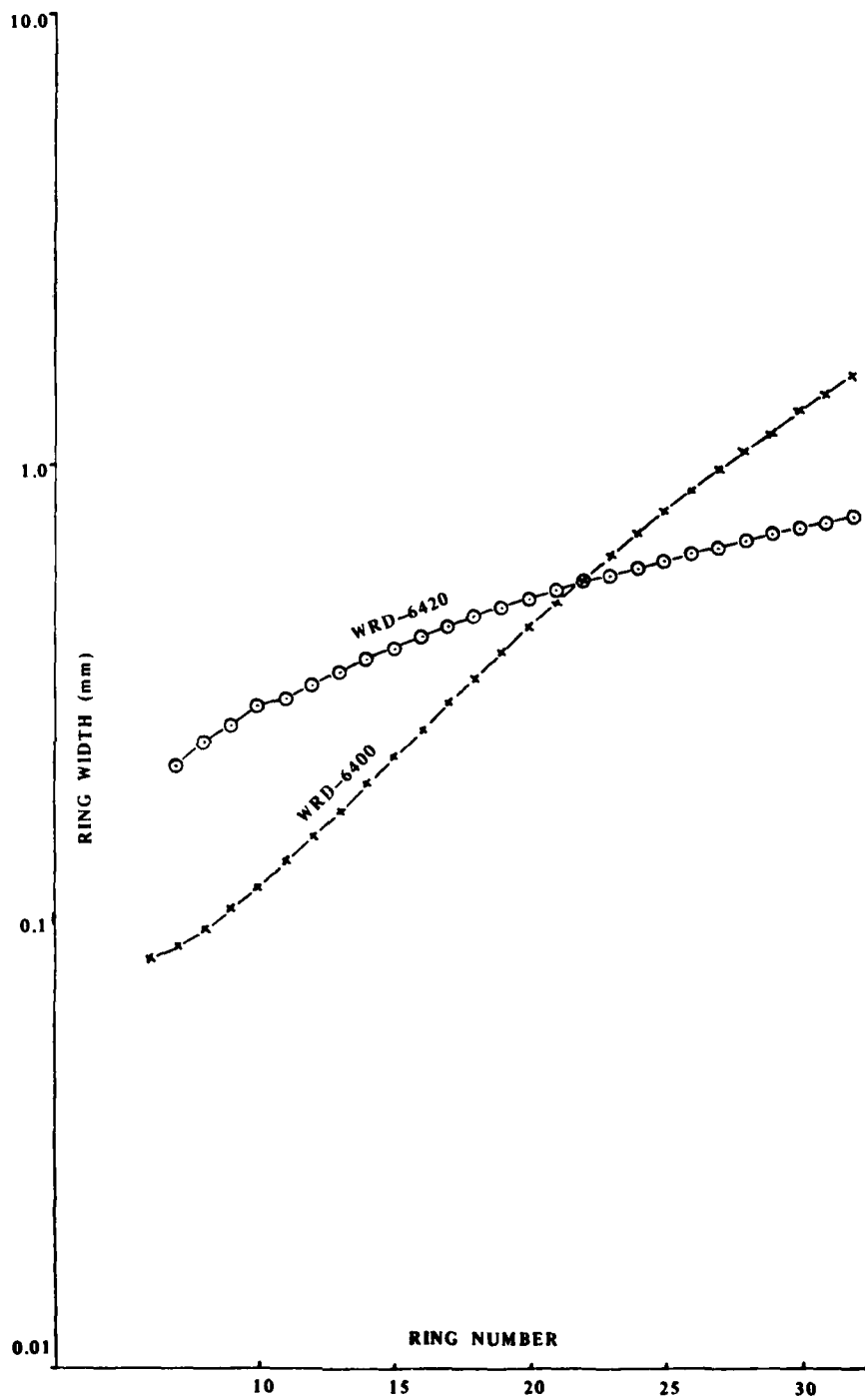


FIGURE 18. Semi-Log Plot of Detector Ring Width for Two ROSA Detector.

E. ROSA Sampling of Grating Spectra. • In the ROSA characterization section, we analytically outlined the general optical and electrical signal flow through the ROSA system. The next section introduced gratings in OPS systems, and the following section dealt with grating and aperture convolution. Then the previous section introduced the geometry of the ROSA detectors. In this section, we integrate the previous material and discuss Ronchi grating sampling with ROSA detector ring and wedge elements.

For this discussion, we assume the condition of equation (17) to be valid, i.e., the gain and bias of the amplifiers are adjusted to normalize responsivity differences of the detector elements and also normalize detector element areas. This condition implies a point source of light imaged on any detector element will yield the same output. This simplifying assumption in no way restricts the generality of the approach, as a review of the ROSA characterization section will indicate that any set of amplifier gains and biases can be used to compute any other set, if so desired.

Now, consider that each ring element of the detector has a finite width with an inner radius and outer radius and that each ring element is separated by a nonsensitive band. We can use these radii for each ring for the limits of integration in equation (6) for determining the signal from any intensity spectrum. This can be visualized by considering the one-dimensional intensity spectra at the bottom of figure 12 with the detector ring radii converted to their spatial frequency equivalents for a given scaling factor of the transform lens focal length and wavelength of light. The signal for each detector element is then proportional to the area of the curve between the ring's inner and outer radii.

We can see from figure 1 that there may be one or more Bessel functions within the area of a wedge, depending upon the spatial frequency of the Ronchi grating illuminated by the aperture. Suppose one side of the intensity spectrum in figure 12 represents the center line of a wedge; the signal for the detector wedge element can be visualized by considering the area under the curve. Depending upon the diameter of the sampling aperture and scaling by the transform lens focal length, the adjacent detector wedge elements will have detectable signal levels owing to the portions of the Bessel functions imaged onto their surfaces.

If we can uniquely fabricate ideal Ronchi rulings at 26 selected grating periods such that with a selected focal length of a transform lens a unique signal will result for each ring element of the detector between 7 and 32, and if we further have the capability of fabricating these Ronchi gratings with 5-degree differences in direction, we then have

the potential capability of encoding 832 separate types of information for the WRD-6420 detector. In the following section, we will simulate the grating detection process for both detectors to show that unique signals can be detected, even for small sampling apertures.

A few comments on the sampling at grating boundary locations in OPS systems are warranted in discussing ROSA grating sampling. Let us begin with equation (3), the basic expression for the grating illuminated by coherent light passing through a sampling aperture. Suppose the grating map $g(x, y)$ is such that $g(x, y) = g_1(x, y) + g_2(x, y)$, where $g_1(x, y)$ and $g_2(x, y)$ are nonoverlapping, contiguous grating functions. For the moment, suppose the sampling aperture diameter is very large; therefore, the aperture convolution effects can be neglected, e.g. if $D = 50.0$ mm then the central lobe of the Bessel function has a diameter of 0.0055 mm, as indicated in table 1 for a transform lens focal length of 177.8 mm and a wavelength of light of 0.6328×10^{-3} mm.

If the illumination is uniform over the aperture and the aperture is located immediately adjacent to the transparency along the optical axis, then

$$g(x, y) = c_1 g_1(x, y) + c_2 g_2(x, y) \quad (27)$$

where c_1 and c_2 represent the percentage of the aperture illuminated by $g_1(x, y)$ and $g_2(x, y)$, respectively. If the respective Fourier transforms of $g_1(x, y)$ and $g_2(x, y)$ are $G_1(u, v)$ and $G_2(u, v)$, then the linearity property of the Fourier transformation indicates

$$[c_1 g_1(x, y) + c_2 g_2(x, y)] = \frac{1}{\lambda f} [c_1 G_1(\rho, \theta_1) + c_2 G_2(\rho, \theta_2)] \quad (28)$$

when expressed in polar coordinates for easier visualization. In this expression, the delta functions of $G_1(\rho, \theta_1)$ and $G_2(\rho, \theta_2)$ are separately collinear along their respective directions of θ_1 and θ_2 . The intensity function of equation (28), however, indicates the possible existence of interaction between $G_1(\rho, \theta_1)$ and $G_2(\rho, \theta_2)$, as shown by

$$\begin{aligned} I(\rho, \theta) &= \frac{1}{\lambda^2 f^2} |c_1 G_1(\rho, \theta_1) + c_2 G_2(\rho, \theta_2)|^2 \\ &= \frac{1}{\lambda^2 f^2} (c_1^2 G_1^2(\rho, \theta_1) + 2c_1 G_1(\rho, \theta_1) c_2 G_2(\rho, \theta_2) \\ &\quad + c_2^2 G_2^2(\rho, \theta_2)) \end{aligned} \quad (29)$$

When θ_1 differs from θ_2 , the interaction term concerns only the delta functions at the origin. When $\theta_1 = \theta_2$, there will be no additional interaction unless the periods of $g_1(x, y)$ and $g_2(x, y)$ are integer multiples, which as table 2 indicates is not likely with the ROSA Model WRD-6420 detector when the Ronchi gratings are properly designed.

Now, let us generalize the discussion for any sampling aperture diameter so as to consider convolution smoothing and interaction*in the spatial frequency domain. Expression (28) is now rewritten as

$$\begin{aligned} \left[a(x, y) \left(c_1 g_1(x, y) + c_2 g_2(x, y) \right) \right] &= \frac{1}{\lambda f} \left[A(\rho, \theta) ** \left(c_1 G_1(\rho, \theta_1) + \right. \right. \\ & \left. \left. c_2 G_2(\rho, \theta_2) \right) \right] = \frac{1}{\lambda f} \left(A(\rho, \theta) ** c_1 G_1(\rho, \theta_1) + A(\rho, \theta) ** \right. \\ & \left. c_2 G_2(\rho, \theta_2) \right) \end{aligned} \quad (30)$$

The intensity function for equation (30) is

$$\begin{aligned} I(\rho, \theta) &= \frac{1}{\lambda^2 f^2} \left[\left(A(\rho, \theta) ** c_1 G_1(\rho, \theta_1) \right)^2 + 2 \left(A(\rho, \theta) ** c_1 G_1(\rho, \theta_1) \right. \right. \\ & \left. \left. \left(A(\rho, \theta) ** c_2 G_2(\rho, \theta_2) \right) + \left(A(\rho, \theta) ** c_2 G_2(\rho, \theta_2) \right) \right)^2 \right] \end{aligned} \quad (31)$$

The first and third terms of equation (31) are additive where they overlap in (ρ, θ) space owing to the convolution broadening. The second term produces a multiplicative function at the origin that is added to those of the first and third terms. Additionally, the multiplicative interaction of the amplitude functions in (ρ, θ) space occurs where the functions of terms one and three overlap. Although this interaction could be considerable for very small sampling apertures, in the Systems Concepts Section a number of strategies will be discussed for uniquely determining grating frequency and direction when the sampling aperture illuminates more than one grating function.

This discussion, although being somewhat general in interpretation to the real world, pertains mainly to the idealized or theoretical Ronchi spectra. Real world spectra will contain even-order harmonics with amplitudes somewhat proportional to their deviation from the theoretical. The real world effect on the theoretical data will result in the potential for overlapping spectra of odd and even harmonics with an associated loss in spatial frequency discrimination.

IV. SIMULATING OPS DETECTION OF RONCHI GRATINGS

A FORTRAN IV program, WRDET, has been prepared to simulate the concepts of the preceding section, wherein ideal Ronchi gratings of selected spatial frequencies are illuminated with collimated light passing through a circular sampling aperture. The intensity spectra derived from the convolved Fourier transforms for these two functions, i.e. the grating and the aperture functions, as given in equation (26), is then partitioned and summed for the appropriate ring and wedge elements of the ROSA detector configuration. The critical variables tested were sampling aperture diameter, Ronchi grating spatial frequency, and focal length of the transform lens.

In this Chapter, we will describe the major features of WRDET and present simulation results.

A. Program WRDET. • Program WRDET simulates detection of ideal Ronchi optical transmission gratings in an optical power spectrum analyzer using a ROSA detector. For a given transform lens focal length and diameter of the sampling aperture, the OPS intensity distributions for RONCHI gratings having spatial frequencies corresponding to mid-ring radii of the ROSA ring detector elements were partitioned according to the ROSA wedge and ring detector elements and integrated for selected wedge and ring detector elements. All calculations were accomplished for the HeNe laser light wavelength of 0.6328 micrometer (μm).

The discussion will follow the flow chart of the major parts of Program WRDET given in figure 19. A listing of the program is included as appendix A. Initialization of Program WRDET involves setting the values for the sampling aperture diameter, the transform lens focal length, the Ronchi grating spatial frequencies corresponding to the mid-ring radii for the selected ring detector elements, the inner and outer radii for the ring and wedge detector elements, and a list of the first four Bessel zero coefficients. An optical scaling factor for the Bessel function is computed, and this factor is used to compute the radii of the Bessel rings in the spatial frequency plane, as indicated in table 1.

The main DO loop of Program WRDET then increments through each selected grating frequency. For each selected spatial frequency, the amplitude and radial distances are computed for each delta function falling on the detector, as indicated in figures 11 and 12.

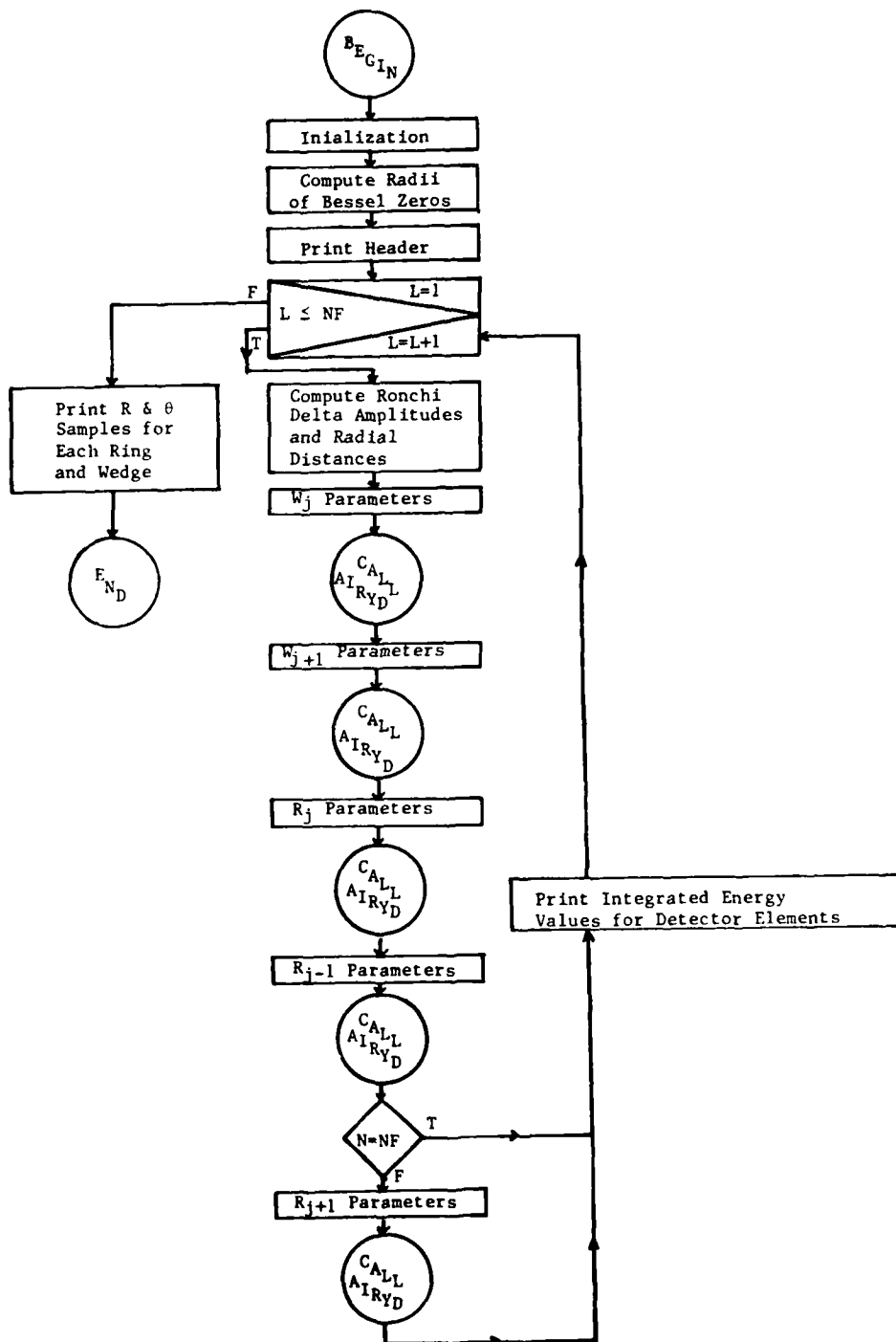


FIGURE 19. Flow Chart of the Main Components of Program WRDET.

For each mid-ring spatial frequency, the integrated OPS is computed for the selected ring R_j and its adjacent rings R_{j+1} and R_{j-1} . Similar computations are made for a wedge W_j and its neighbor W_{j+1} when the grating is oriented so that the Ronchi grating deltas are collinear along the bisector of the wedge W_j . These computations are made in Subroutine AIRYD, which is outlined in the flowchart in figure 20. This subroutine integrates the two-dimensional diffracted energy incident on a wedge or ring detector element in the spatial frequency plane by Simpson's Rule using polar coordinates. Thus, the subroutine performs the integration of equation (26) where the definite integrals have limits set by the indicated wedge or ring element.

When Subroutine AIRYD is called, the radial and angular sampling parameters are computed. Next, a table of normalized first-order Bessel amplitudes are computed for the appropriate scaling parameter, as indicated in figure 8. Then, nested integration DO loops increment through all angle and radial-distance sample points. For each sample point, the radial distance between that point and the position of each Ronchi delta function on the detector is used to determine the scaled Bessel amplitudes. The sum of these amplitudes for each point are then squared to obtain the intensity estimate. Simpson's integration rule is applied for the radial and angular dimensions to provide a number representing the detector element signal.

The major assumption associated with Program WRDET involves the maximum radius of the first-order Bessel function used in the computation of diffraction amplitudes. The first-order Bessel function is infinite in extent and to make computation tractable, yet meaningful, required truncation of the Bessel function. As indicated in figure 10, the function has most of its energy within the central lobe, 83.8 percent, and the total energy contained by the Bessel function radii within the second, third, and fourth zeros are 91.0, 93.8, and 95.3 percent, respectively. In table 1, the radial distances for these zero crossings are shown for six aperture diameters and two transform lens focal length values. A realistic and effective compromise for the Bessel function truncation radius would be the fourth zero radius.

The line-printer output from Program WRDET needs to be explained. The results of the simulation data are presented in appendix B and will be discussed in detail subsequently. Each simulation run is on a separate sheet having a header indicating programmed values for transform lens focal length, sampling aperture diameter, radius to the fourth Bessel zero, optical wavelength, RSI detector model, and number of sampling divisions in the Bessel function to the fourth zero. The body of the printout lists the integrated values for equation (26) for detector rings R_{j-1} , R_j , and R_{j+1} and detector wedges W_j and W_{j+1} for each mid-ring grating spatial frequency.

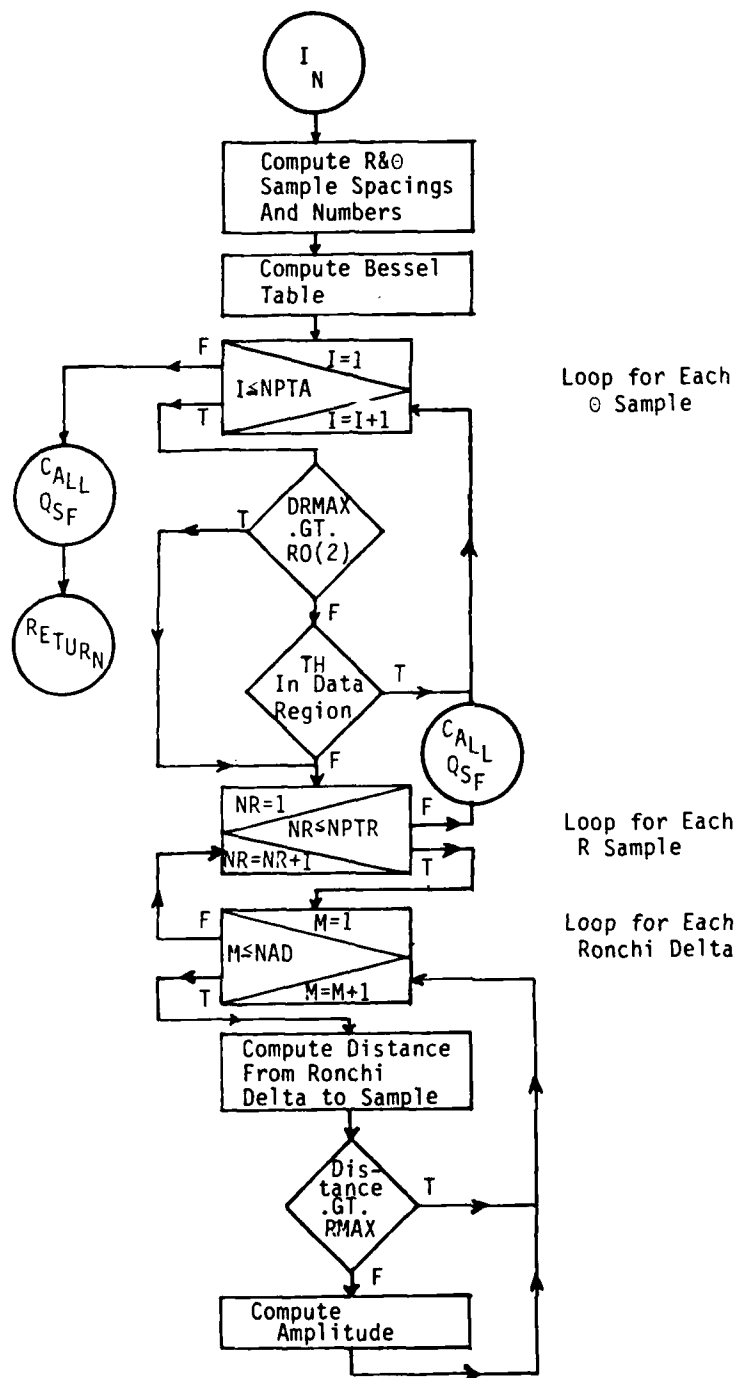


FIGURE 20. Flow Chart of Subroutine AIRYD.

It is important to note that the simulation values have not been scaled by the factor

$$I_{st} = K^2 = \left[\frac{B\pi D^2}{4\lambda f} \right]^2 \quad (32)$$

as shown in equation (23) and equation (26). In table 4, the values for the scaling factor are indicated for four transform lens focal lengths and four aperture diameters when $B = 1.0$. To adjust the light input amplitude B so as to maintain normalized output from the values in table 4, we have

$$B = \frac{4\lambda f}{\pi D^2} = \left[\frac{1}{I_{st}} \right]^{1/2} \quad (33)$$

and the expected range of B , for the simulations to be presented, is well within operational optical capabilities.

B. Simulation Results. • Program WRDET was used to provide simulation data for the OPS detection of Ronchi gratings with a ROSA detector. The simulations are grouped into three data sets and summarized with their simulation conditions in table 5. Data Set 1A simulates detection conditions for the WRD-6420 detector with different transform lens focal lengths and sampling aperture diameters, and Data Set 1B simulates the WRD-6400 detector with similar conditions. Data Set 2 simulates data from uniform Ronchi grating deformations for the WRD-6420 detector, i.e. the Ronchi grating frequency is displaced some percentage from the mid-ring grating frequency in Data Set 2A and the Ronchi grating direction is displaced by an angular factor from the mid-wedge angle in Data Set 2B. Data Set 3 simulates a non-existent detector with equal ring widths (Data Set 3A) and with modifications of equal ring width (Data Set 3B). Table 5 lists the illustration number for the graphical presentation of the data and the appendix B page of the data listings.

TABLE 4. Intensity Scaling Factors.

$$I_{SF} = \frac{B\pi D^2}{4\lambda f}^2$$

where $B=1.0$ and $\lambda=0.6328 \times 10^{-3} \text{mm}$

Aperture Diameter	f = 100.0 mm	f = 177.8 mm	f = 622.3 mm	f = 1016.0 mm
0.1	0.01540	0.99487	0.00040	0.00015
0.25	0.60174	0.19035	0.01554	0.00583
0.5	9.62780	3.04553	0.24861	0.09327
1.0	154.4472	48.72853	3.97784	1.49231

TABLE 5. Summary of Simulation Conditions with Illustration and Data Page References. (all measurements in mm)

Data Set 1A:		D			
WRD-6420 Detector		0.50	0.25	0.10	0.075
	177.8	Fig. 21 B-1	Fig. 22 B-2,3	Fig. 23 B-4,5	No Data
f	100.0	Fig. 24 B-6	Fig. 25 B-7	Fig. 26 B-8	Fig. 27 B-9,10

Data Set 1B:		D			
WRD-6400 Detector		0.50	0.25	0.10	0.075
	177.3	Fig. 31 B-11	Fig. 32 B-12	Fig. 33 B-13	No Data
f	100.0	No Data	Fig. 34 B-14	Fig. 35 B-15	Fig. 36 B-16

Data Set 2A:

WRD-6420 Detector, $f = 100.0$ mm, Grating freq = factor x mid-ring freq

factor	D = 0.1	D = 0.075	
0.96		B-25	
0.97		B-18	
0.98		B-19	
0.99	Table 14	B-20	
1.00		B-8	
1.01		B-21	
1.02		B-22	
1.03		B-23	
1.04		B-24	
		Table 15	B-26
			B-27
	B-9,10		
	B-28		
		B-29	
		B-30	

TABLE 5. Continued.

Data Set 2B:

WRD-6420 Detector, $D = 0.1$ mm, $f = 100.0$ mm, Grating angle = wedge center
+ factor angle

Factor angle

0.0	B-8
0.5	B-31
1.0	B-32
1.5	B-33
2.0	B-34
2.5	B-35

Data Set 3A:

Equal ring width detector, $D = 0.1$ mm

f

100	Fig. 40, B-36
150	Fig. 41, B-37
200	Fig. 42, B-38

Data Set 3B:

Modified equal ring width detector, $D = 0.1$ mm, $f = 100.0$ mm

Mod-1	B-39
Mod-2	B-40
Mod-3	B-41

1. Data Set 1A - Detector WRD-6420 Simulations. Figures 21 through 27 contain plots of the simulation data for Data Set 1A. The purpose of this data set is to show the nature of the detector element responses and S/N for the WRD-6420 ROSA detector with different transform lens focal lengths (177.8 and 100.0 mm) and sampling aperture diameters (0.5, 0.25, 0.10, and 0.075 mm). In reviewing this data set, we will first look at the gross comparison of the curves and then at the details of curve configuration and curve differences. The WRD-6420 dimensional data in table 2 and figures 2 and 18 will be referred to frequently in the detailed discussions.

For a transform lens focal length of 177.8 mm, we note that the S/N for the rings and wedges (R_j/R_{j-1} , or R_j/R_{j+1} , and W_j/W_{j+1}) increases sharply for the 0.5 mm sampling aperture and the signal ring R_j and wedge W_j values are generally of the same order of magnitude. As the aperture is made smaller, we see that the S/N decreases, the positive slope of the signal detector elements R_j and W_j increases, and the negative slope of the adjacent detector elements, R_{j-1} , R_{j+1} , and W_{j+1} , decreases. For the smallest sampling aperture at this focal length, 0.1 mm, and S/N values for the wedges are positive throughout; whereas, the S/N values for the rings are less than one for the lower spatial frequencies.

For a transform lens focal length of 100.0 mm, the same generalizations are valid with the additional statement that the S/N values are higher. This is readily seen by comparing figures 24 and 21.

At this time, we will consider the details of curve configuration and curve differences. Graphical and tabular summaries will be introduced to aid in this analysis.

The similarity of figures 21 and 25 is important. We note that for figure 21, when $f = 177.8$ mm and $D = 0.5$ mm, the relative aperture, given by $f^\# = f/d$, is $f/355.6$; and for figure 24, when $f = 100.0$ mm and $D = 0.25$ mm, the relative aperture is $f/400.0$. As shown in table 1, the relative aperture provides the scaling function for the relative size of the Bessel function in the spatial frequency domain. The Bessel function zero crossings pertaining to Data Set 1 can be abstracted from table 1 and shown in table 6 as diameters between Bessel function zeros. Considering that 83.9 percent of the energy of the Bessel function is contained in the central maximum, i.e. the diameter between the first zero crossing, that only 7.1 percent of the energy is between the first and second zero crossings, and that 2.8 percent and 1.5 percent of the total energy occurs between the second to third and the third to fourth zero crossings, respectively, one can use the detector ring and wedge dimensional data in table 2, with the Bessel function zero crossing dimensions to assist in understanding the ring and wedge data in figures 21 through 27.

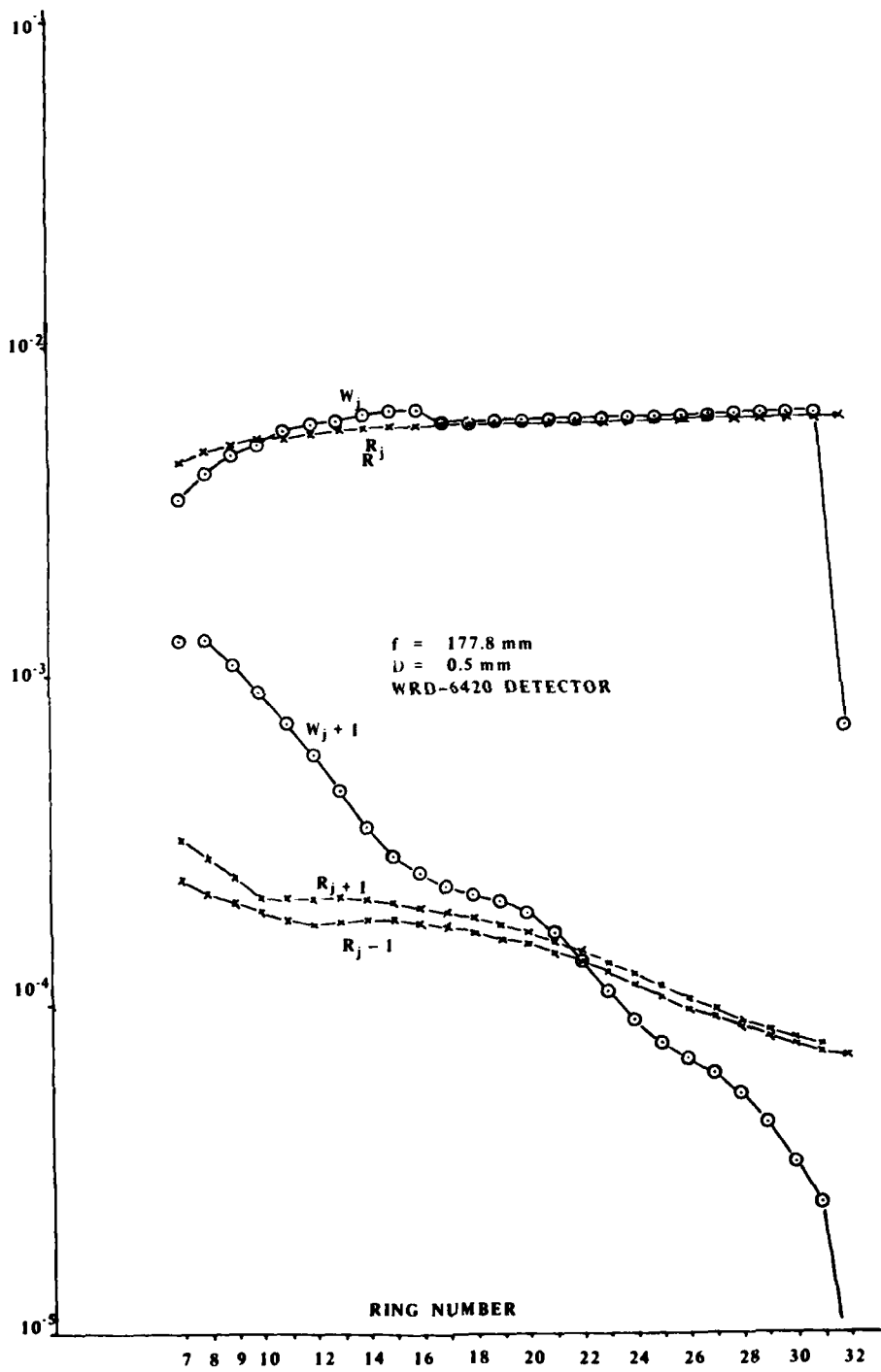


FIGURE 21. ROSA Simulation Results. A

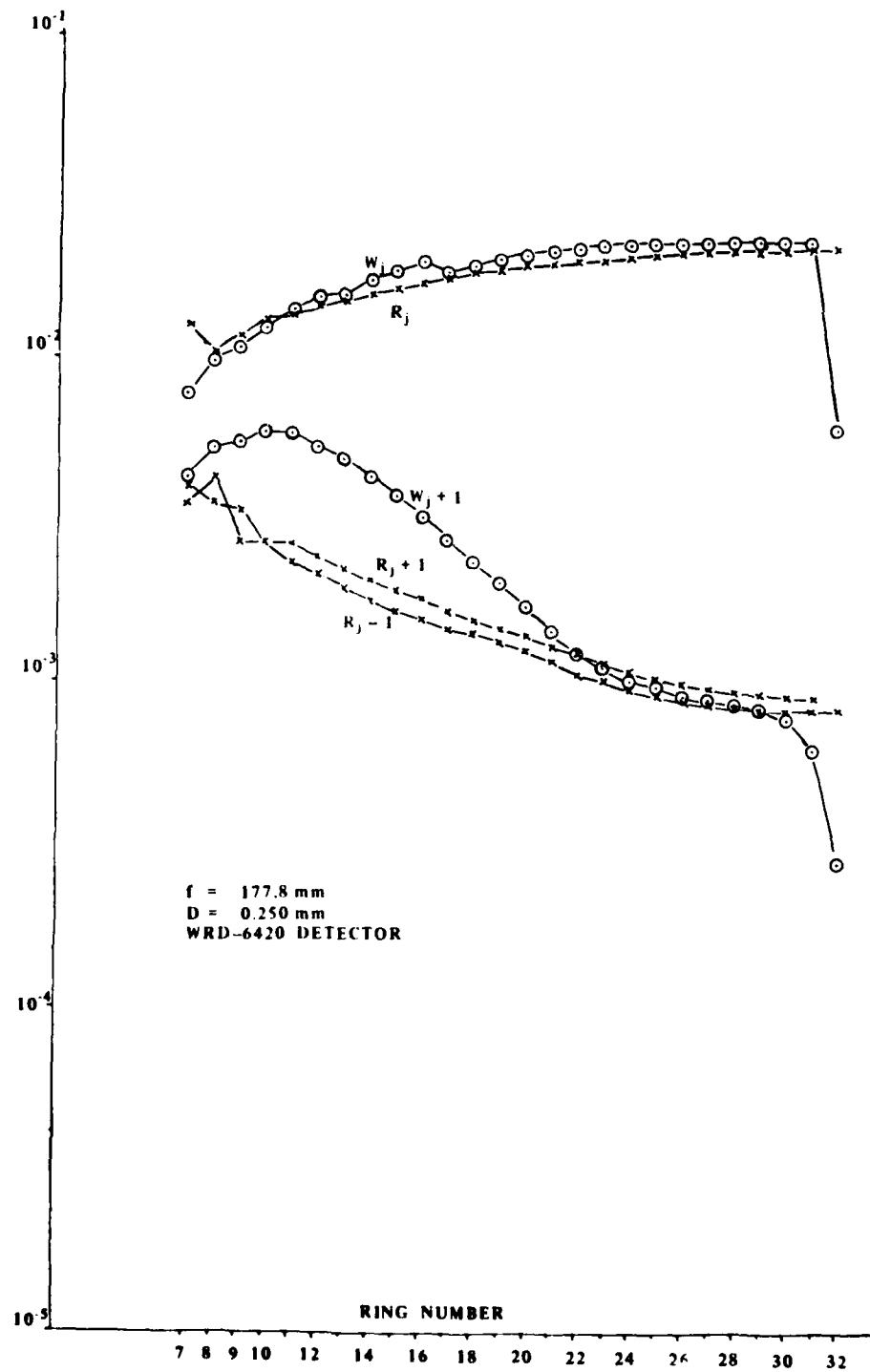


FIGURE 22. ROSA Simulation Results. B

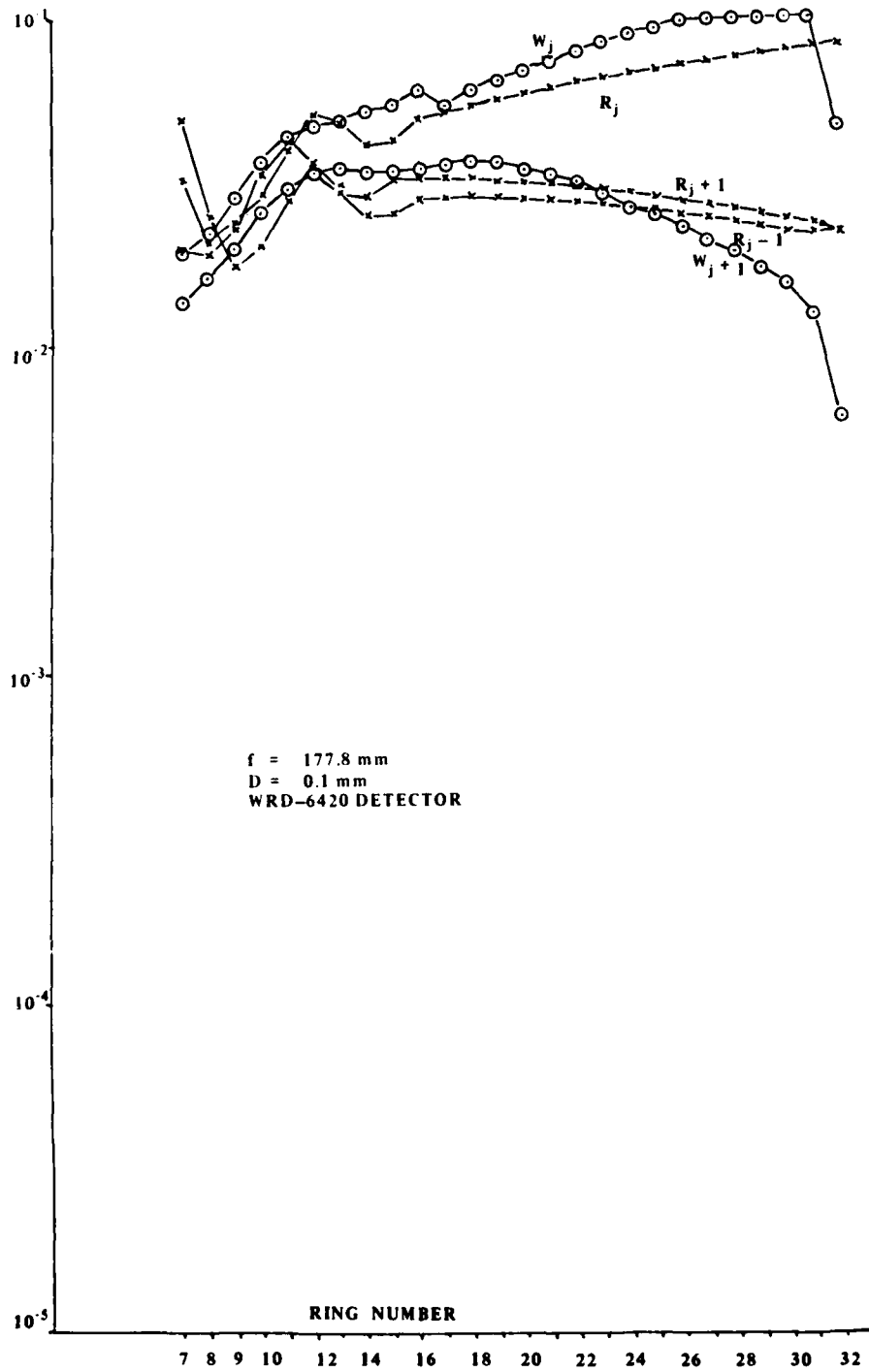


FIGURE 23. ROSA Simulation Results. C

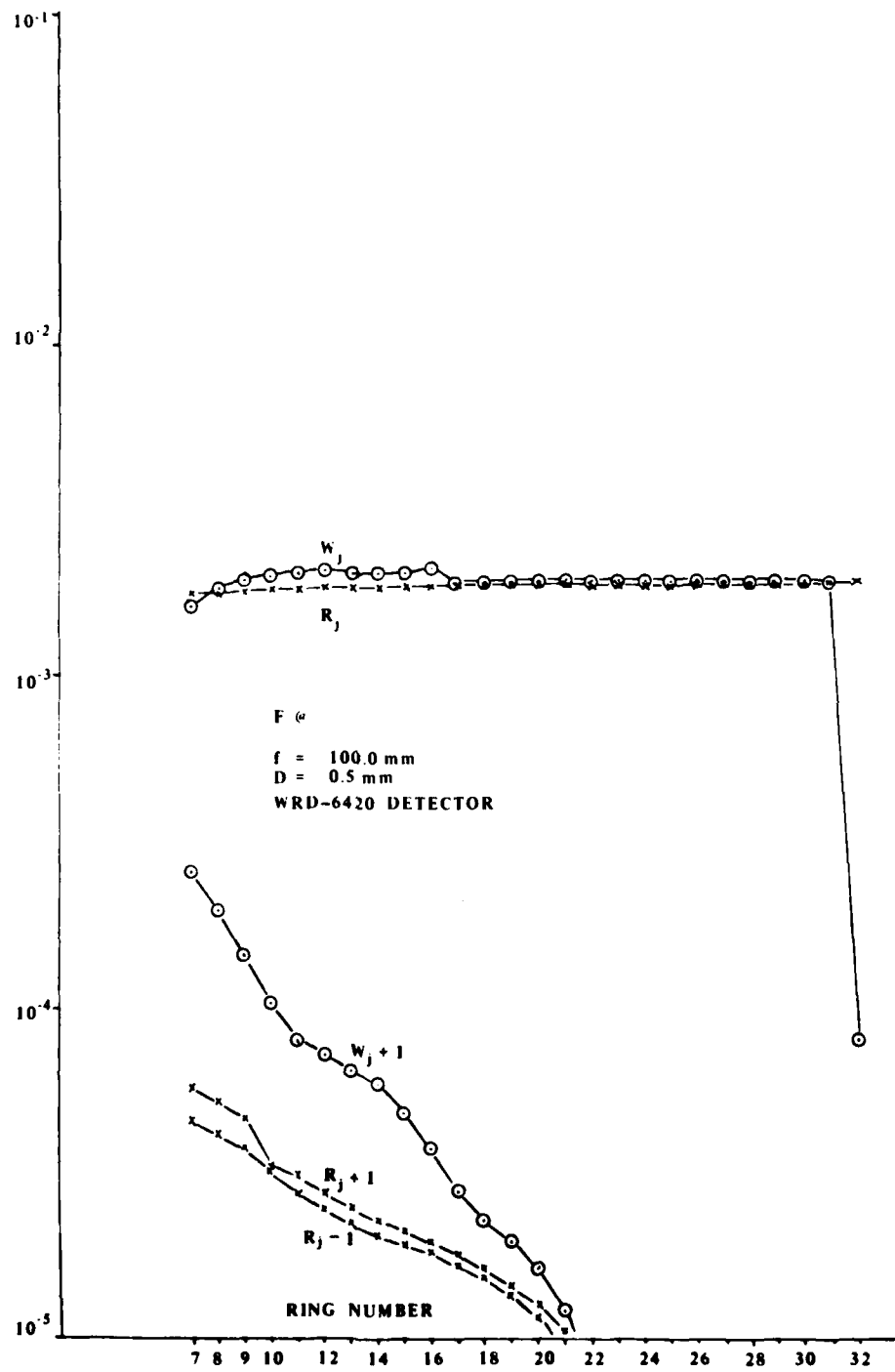


FIGURE 24. ROSA Simulation Results. D

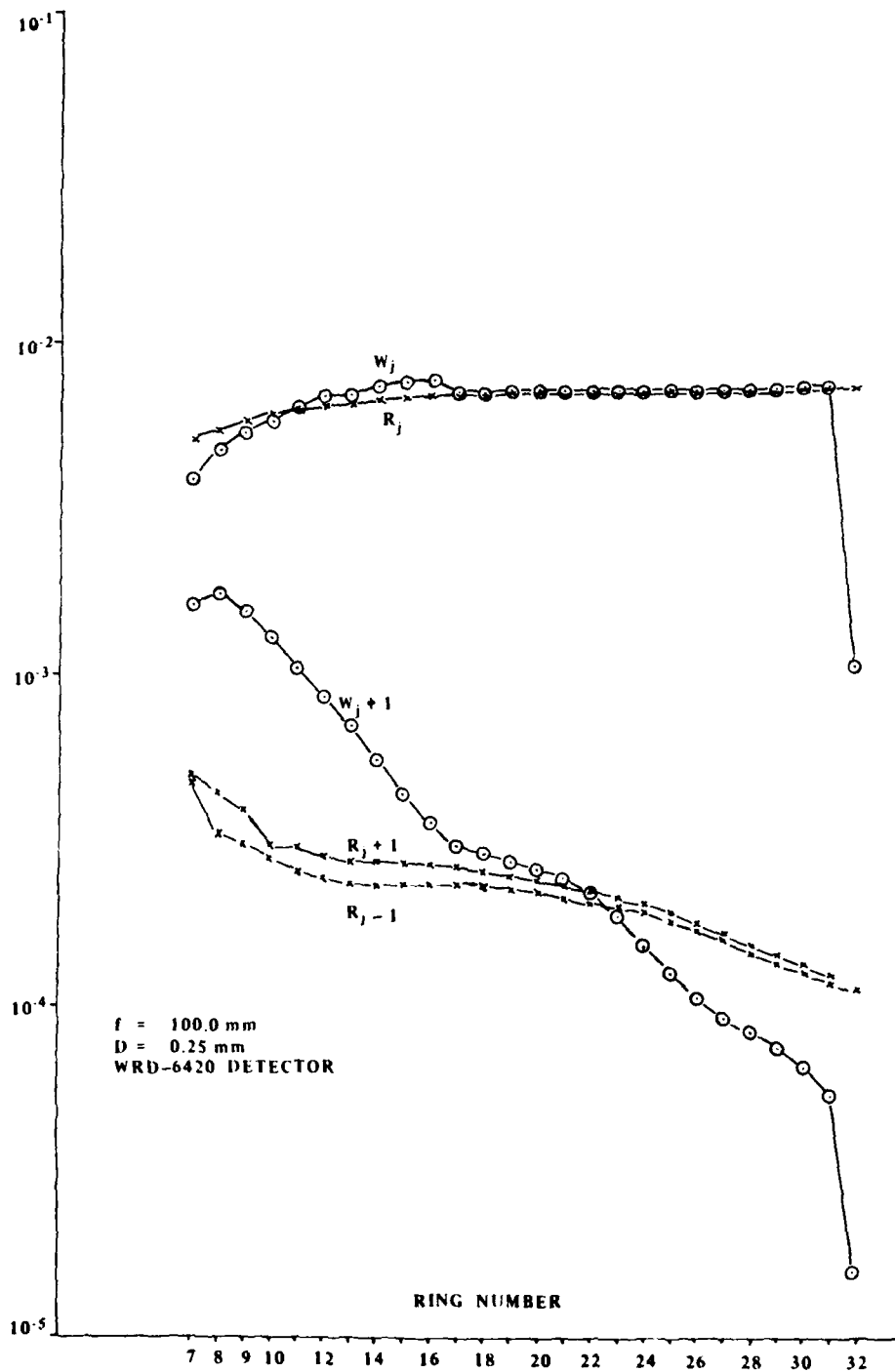


FIGURE 25. ROSA Simulation Results. E

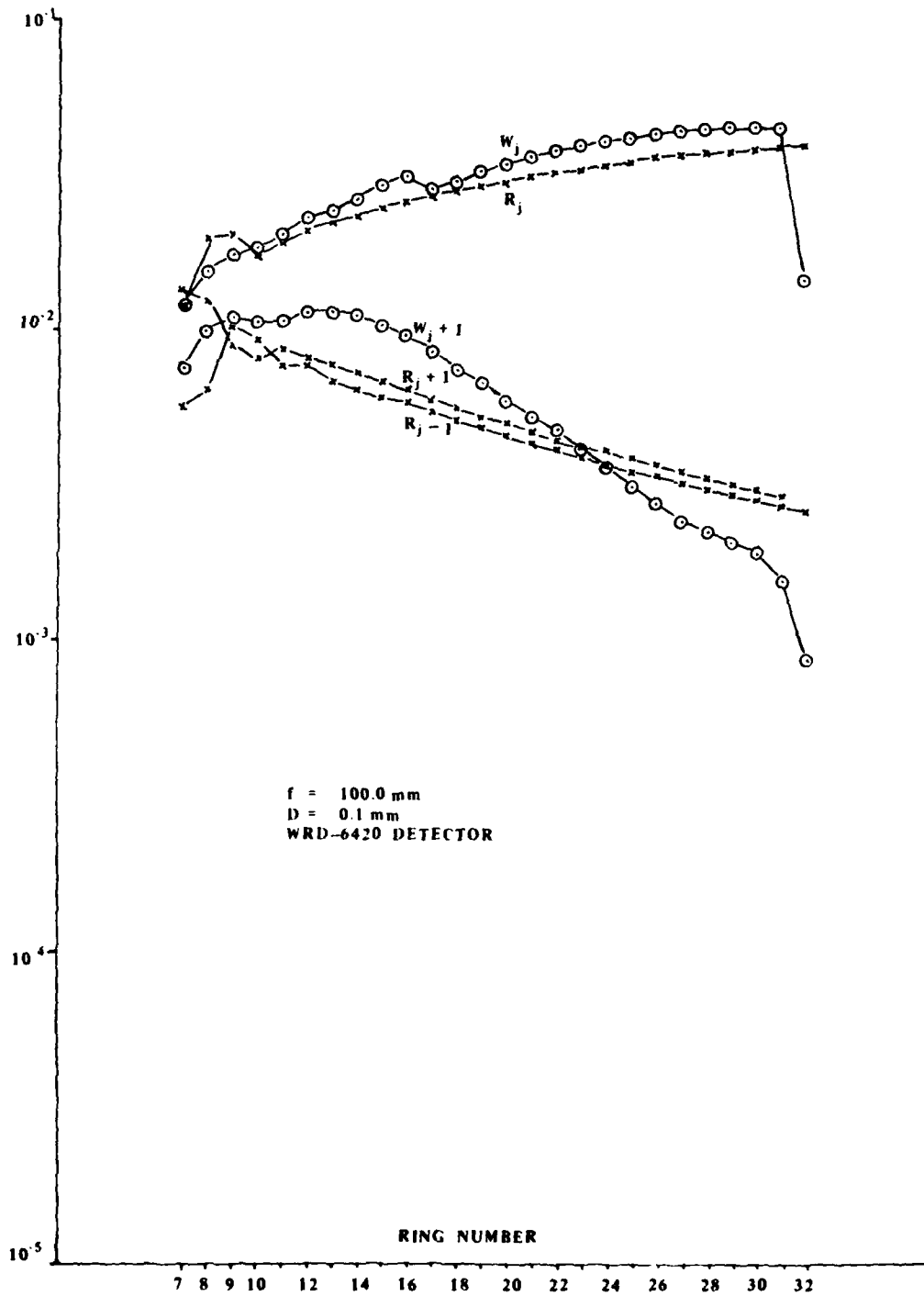


FIGURE 26. ROSA Simulation Results. F

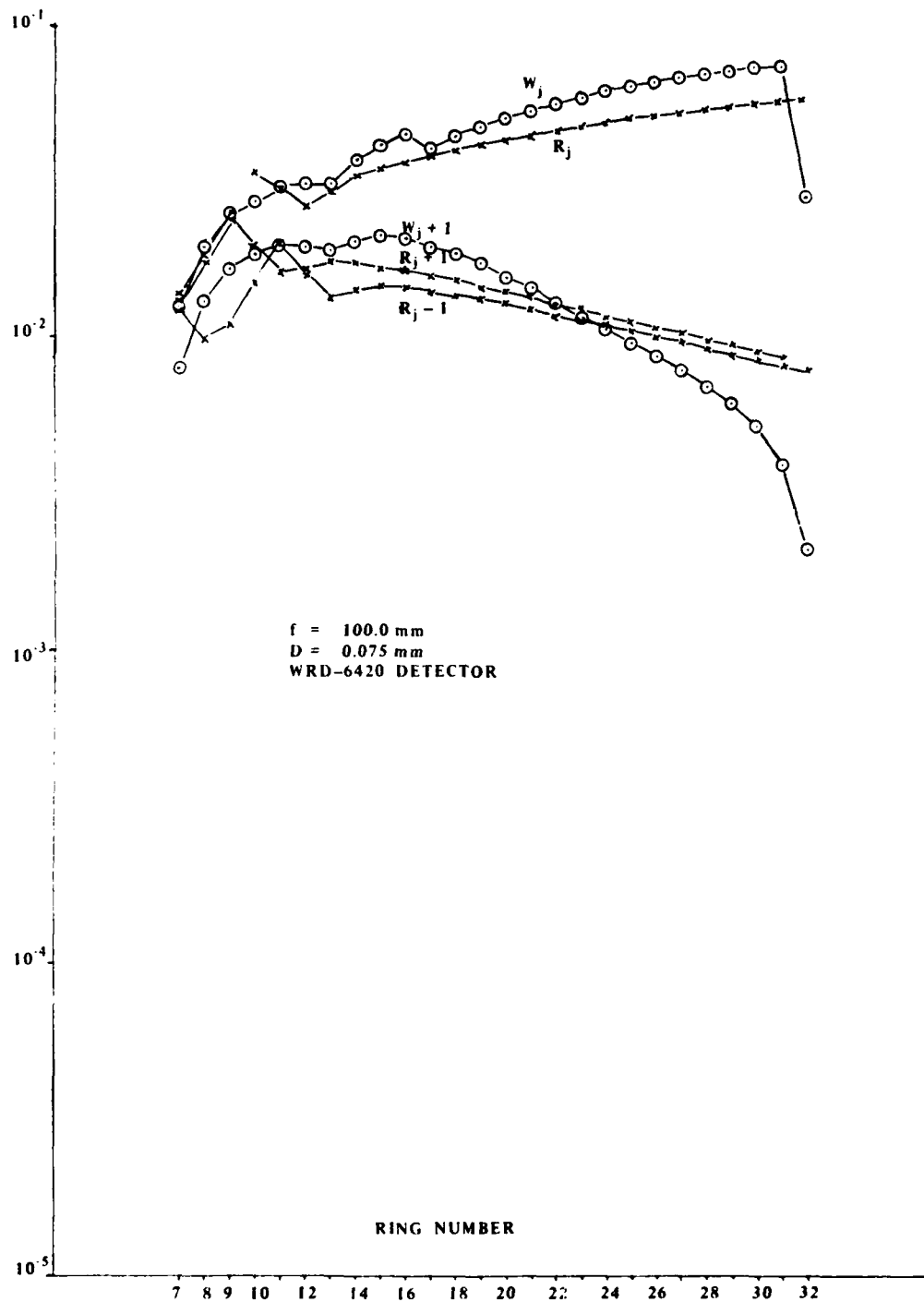


FIGURE 27. ROSA Simulation Results. G

TABLE 6. Diameters Between Zero-Order Bessel Functions, Zeros for Selected Transform Lens Focal Lengths (f) and Sampling Aperture Diameters (D). (Dimensions in mm).

Zero Crossing	f = 177.8			f = 100.0		
	D = 0.50	D = 0.25	D = 0.10	D = 0.50	D = 0.25	D = 0.10
1st Zero	0.550	1.098	2.746	0.308	0.618	1.544
2nd Zero	1.004	2.010	5.024	0.566	1.130	2.826
3rd Zero	1.458	2.914	7.286	0.820	1.640	4.098
4th Zero	1.908	3.818	9.544	1.074	2.146	5.366
						2.058
						3.768
						5.464
						7.156

Another useful type of data for interpretation of Data Set 1 is the location of the Ronchi Grating deltas for the mid-ring spatial frequencies associated with the WRD-6420 detector when the transform lens focal lengths are specified. Table 7 represents data of this type for a 177.8 mm transform lens focal length, and table 8 has similar data for a 100.0 mm lens.

The next data analysis aids to be introduced are the generalized ring and wedge models shown in figure 28. The ring model shows the Bessel functions, represented in plan view by the four zero crossing circles, located at the mid-ring radius, and each successive ring has a greater radius difference, as shown in table 2 and figures 17 and 18. The scale of the Bessel function is arbitrary and can be adjusted to satisfy our interpretation of the mod and to fit the curve being interpreted. The wedge model of figure 28 represents the Bessel functions positioned for a Ronchi grating spatial frequency of 30.39 line-pairs per millimeter when the 177.8 mm transform lens is employed. This corresponds to the data for Ring 13 in table 7. This wedge model has 3 general cases and 18 special cases, shown in figures 29 and 30, respectively. The general cases apply where all of the Bessel function energy within the fourth zero radius is incident on the detector wedges. For the first general case, the Bessel function is scaled so that the total significant energy is detected by W_j and the energy in W_{j-1} and W_{j+1} is considered insignificant. In general case two, all of the energy is contained in wedges W_{j-1} , W_j , and W_{j+1} ; and for general case three, the energy is incident on other adjacent wedges. The special cases apply when portions of the scaled Bessel function exist outside of the detector wedges. In figure 30, the special cases of the bottom row apply when the lower radius of the detector wedges (WLR) is greater than the axial distance of the delta harmonic r_p less the fourth zero radius of the Bessel function r_2 . Likewise, the special cases in the top and middle rows of figure 30 apply when portions of the fourth zero circle are beyond the higher radius of the detector wedges (WHR). Table 9 represents a summary of the occurrences of special cases for selected simulation with the WRD-6420 detector, which will be useful in analyzing curves for detector signals.

Figure 21 can be analyzed as a simple example of a detailed curve analysis. The remaining curves in Data Sets 1A and 1B can be analyzed in like fashion. First, note that the scaled Bessel function at the origin has a fourth zero crossing radius less than the least radius of Ring 7 (tables 6 and 2). Next, note that with the first harmonic positioned at the mid-radius of Ring 7, there will be no signal contribution on Ring 7 owing to the Bessel function positioned at the third-order harmonic (tables 2, 6 and 7). This lack of signal is easily seen when the third-order Bessel function is positioned at an axial distance of 3.855 mm and when the radius of fourth zero crossing for $f = 177.8$ mm and $D = 0.5$ mm is 0.954 mm. When subtracted, the resulting radial distance (2.901 mm) is greater than the maximum ring radius (1.395 mm) for Ring 7. Thus,

TABLE 7. Summary of Ronchi Grating Deltas for 177.8 mm Transform Lens Focal Length (Detector WRD-6420).

Ring No.	Mid-Ring Spatial Frequency	Axial Distance of Ronchi Harmonics (mm) (Circled Distances Are Harmonics Beyond Detector)											Harmonic Delta Intensity
		0	1	3	5	7	9	11					
7	11.42	0	1.285	3.855	6.424	8.994	11.564	14.134	0.0008				
8	14.04	0	1.580	4.739	7.898	11.058	14.217	17.380					
9	16.87	0	1.898	5.694	9.490	13.287	17.082						
10	19.93	0	2.242	6.727	11.212	15.697	20.178						
11	23.26	0	2.617	7.851	13.085	18.319							
12	26.72	0	3.006	9.019	15.032	21.042							
13	30.39	0	3.419	10.258	17.095								
14	34.27	0	3.856	11.567	19.280								
15	38.34	0	4.314	12.941	21.570								
16	42.61	0	4.794	14.382	23.970								
17	47.08	0	5.297	15.891									
18	51.75	0	5.822	17.466									
19	56.61	0	6.369	19.107									
20	61.67	0	6.939	20.817									
21	66.93	0	7.530	22.590									
22	72.40	0	8.146	24.438									
23	78.04	0	8.780	26.340									
24	83.88	0	9.437	28.311									
25	89.92	0	10.117	30.351									
26	96.16	0	10.819	32.457									
27	102.59	0	11.543	34.629									
28	109.21	0	12.287	36.861									
29	116.05	0	13.057	39.171									
30	123.07	0	13.847	41.541									
31	130.28	0	14.658	43.974									
32	137.69	0	15.492	46.476									

TABLE 8. Summary of Ronchi Grating Deltas For 100.0 mm Transform Lens Focal Length (Detector WRD-6420).

Ring No.	Mid-Ring Spatial Frequency	Axial Distance of Ronchi Harmonics (mm) (Circled Distances Are Harmonics Beyond Detector)											Harmonic Delta Intensity	
		0	1	3	5	7	9	11						
7	20.31	0	1.285	3.856	6.426	8.997	11.567	14.137						
8	24.97	0	1.580	5.740	7.901	11.061	14.221	17.381						
9	30.01	0	1.899	5.697	9.495	13.293	17.091							
10	35.45	0	2.244	6.730	11.216	15.703	20.189							
11	41.36	0	2.618	7.852	13.086	18.321								
12	47.52	0	3.007	9.021	15.035	21.049								
13	54.05	0	3.420	10.261	17.101									
14	60.94	0	3.856	11.569	19.281									
15	68.17	0	4.314	12.941	21.569									
16	75.76	0	4.794	14.382	23.970									
17	83.71	0	5.297	15.892										
18	92.02	0	5.823	17.469										
19	100.66	0	6.370	19.109										
20	109.66	0	6.939	20.818										
21	119.01	0	7.531	22.593										
22	128.73	0	8.146	24.438										
23	138.76	0	8.781	26.342										
24	149.13	0	9.437	28.311										
25	159.88	0	10.117	30.352										
26	170.97	0	10.819	32.457										
27	182.41	0	11.543	34.629										
28	194.20	0	12.289	36.867										
29	206.34	0	13.057	39.172										
30	218.82	0	13.847	41.541										
31	231.64	0	14.658	43.975										
32	244.80	0	15.492	46.473										

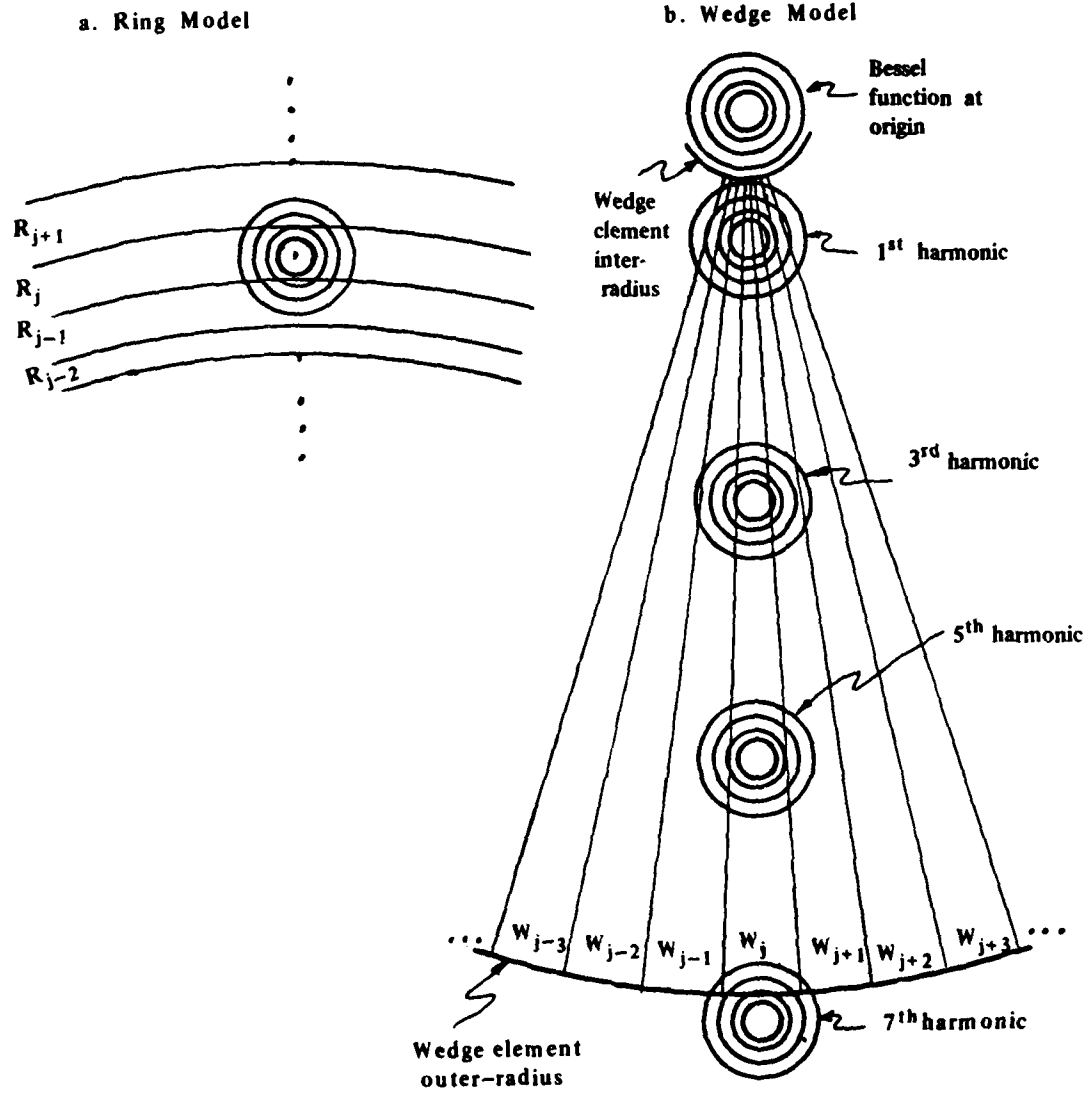
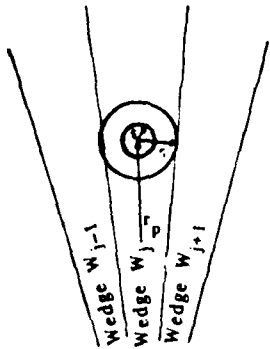


FIGURE 28. Generalized Ring and Wedge Models.

LET: r_p = axial distance of i^{th} delta harmonic.
 r_1 = radius of inscribed circle in wedge W_j , centered at r_p .
 r_2 = radius of Bessel function 4th zero.
 r_3 = radius of inscribed circle in wedges $W_{j-1} + W_j + W_{j+1}$, centered at r_p .

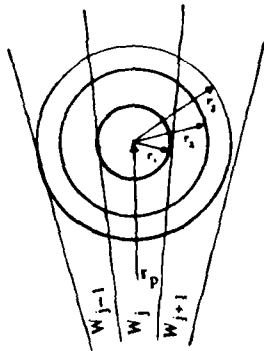


GENERAL CASE #1 - When $r_2 \leq r_1$.
 Energy E_j on wedge W_j due to Bessel function centered at r_p is

$$E_j \approx I_i [1 - J_0^2(\pi r_2 D / \lambda f)] = I_{r_2}$$

where I_i is the intensity of the i^{th} delta harmonic.

Energy E_{jh} on Wedge W_{j+1} is considered insignificant.



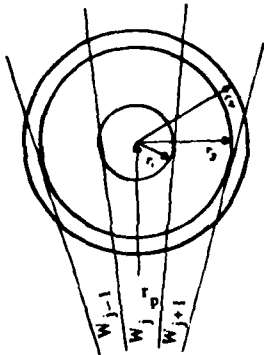
GENERAL CASE #2 - When $r_1 < r_2 \leq r_3$.
 Energy E_j on wedge W_j is

$$E_j \approx I_{r_2} - I_i P'$$

where P' is percentage of Bessel function energy in sectors outside of W_j .

Energy E_{jh} on wedge W_{jh}

$$E_{jh} \approx I_i P' / 2$$



GENERAL CASE #3 - When $r_2 > r_3$.
 As in General Case #2 Energy on W_j is

$$E_j \approx I_{r_2} - I_i p P'$$

Energy E_{j+1} on wedge W_{j+1} is

$$E_{j+1} \approx I_i (P' - P'') / 2$$

where P'' is percentage of Bessel function energy in sectors outside of

$$(W_{j+1} + W_j + W_{j+1}).$$

FIGURE 29. Three General Cases for Estimating Bessel Function Energy Incident on a ROSA Wedge Detector Element.

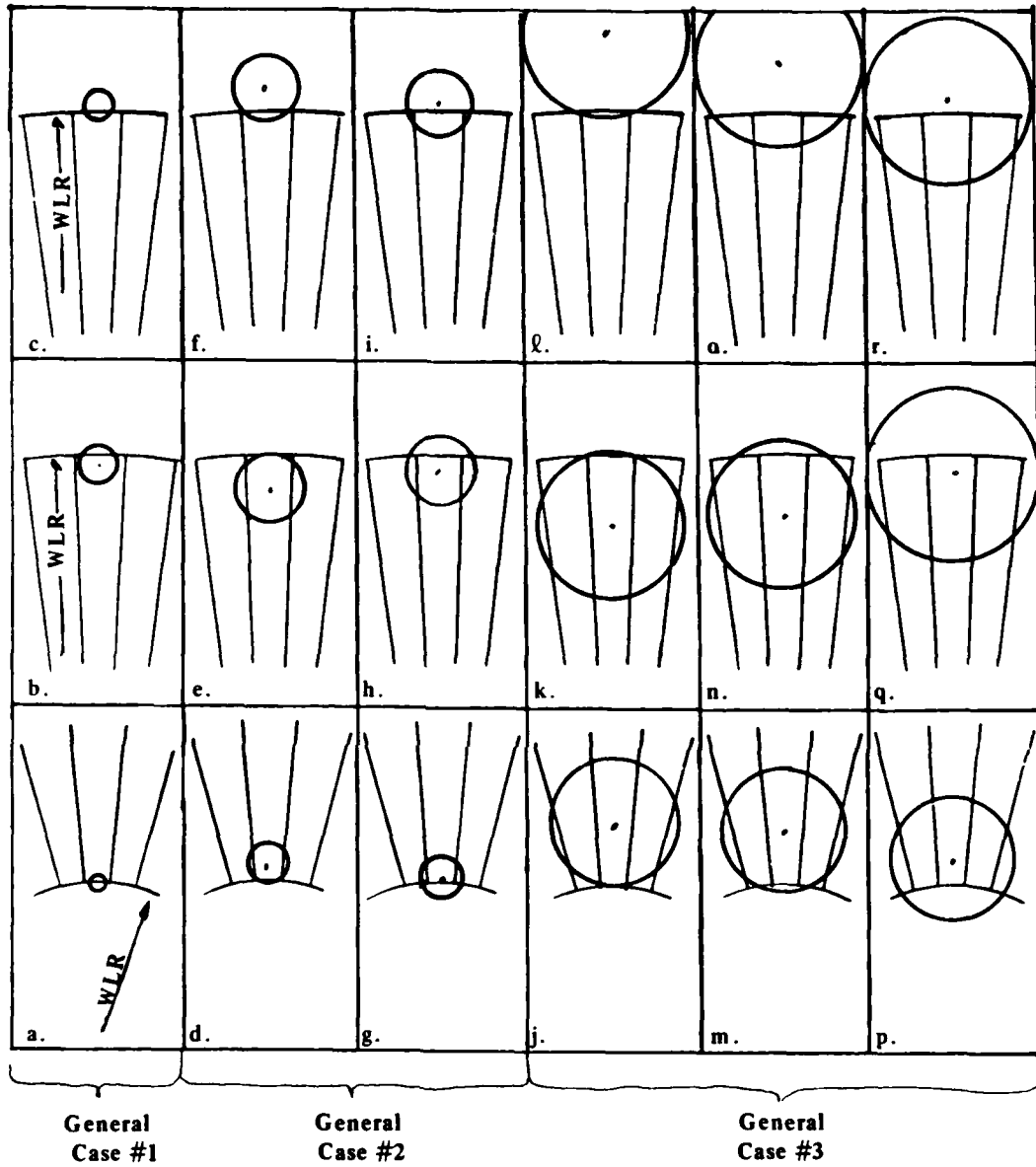


FIGURE 30. Eighteen Special Cases for Estimating Bessel Function Energy Incident on a ROSA Wedge Detector Element.

the ring detector signals for conditions of figure 21 are due to a single Bessel function positioned at the mid-ring radius. The R_j curve is directly relatable to the plots of ring widths in figure 17 and 18, and the shapes of R_{j-1} and R_{j+1} curves can also be related to these plots.

The wedge signals for figure 21 can be analyzed from table 7, which defines the axial distances and intensities of Ronchi deltas, from figures 29 and 30, which describe the general and special cases for estimating wedge signals, and from table 9, which summarizes the occurrences of the special cases. It will be noted that all W_j curves in figures 21 through 27 have a discontinuity between Ring 16 and Ring 17. This discontinuity is due to the transition from the occurrence of the first and third harmonics on the detector for the Ring 16 data to the first harmonic on the detector when the third harmonic is off of the detector for the Ring 17 data, as seen from tables 7 and 9. The slope changes in the W_{j+1} curves can be related to the diameter of the Bessel function zeros in table 6, the wedge width data in table 2, and the slope changes in figure 10.

Table 10 summarizes the number of detector elements with S/N greater than 1.0 for the data in Data Set 1A. It should be noted that when the $f^\#$ is less than about 1,000, all 26 rings and 32 wedges have S/N greater than 1.0, and the S/N improves inversely with $f^\#$.

2. Data Set 1B - Detector WRD 6400 Simulations. Table 5 lists the simulation conditions under which Data Set 1B was obtained. The essential differences between these data and those of Data Set 1A were the detectors, which have been described in the section Geometry of ROSA Detectors. Data Set 1B simulation results obtained with the WRD-6400 detector are presented in figures 31 through 36, and a quick comparison with their counterparts in Data Set 1A will show significant differences. The simulation results of Data Set 1B are generally less well-behaved and have lower S/N ratios. Details of the plots can be explained by using the plots of mid-ring radii for the two detectors in figures 15 and 16, the plots of the ring widths in figures 17 and 18, the dimensions of the two detectors in tables 2 and 3, and the summaries of Ronchi grating deltas for the 177.8 and 100.0 mm transform lens focal lengths shown in tables 11 and 12, respectively.

TABLE 10. Detector Elements with $S/N > 1$ In Data Set 1A.

	f	D	f/D	Number of Detector Elements with $S/N > 1$	
				Rings	Wedges
Fig. 21	177.8 mm	0.5 mm	355	26	32
22	177.8	0.25	711	26	32
23	177.8	0.10	1778	21	32
24	100.0	0.5	200	26	32
25	100.0	0.25	400	26	32
26	100.0	0.10	1000	25	32
27	100.0	0.075	1333	23	32

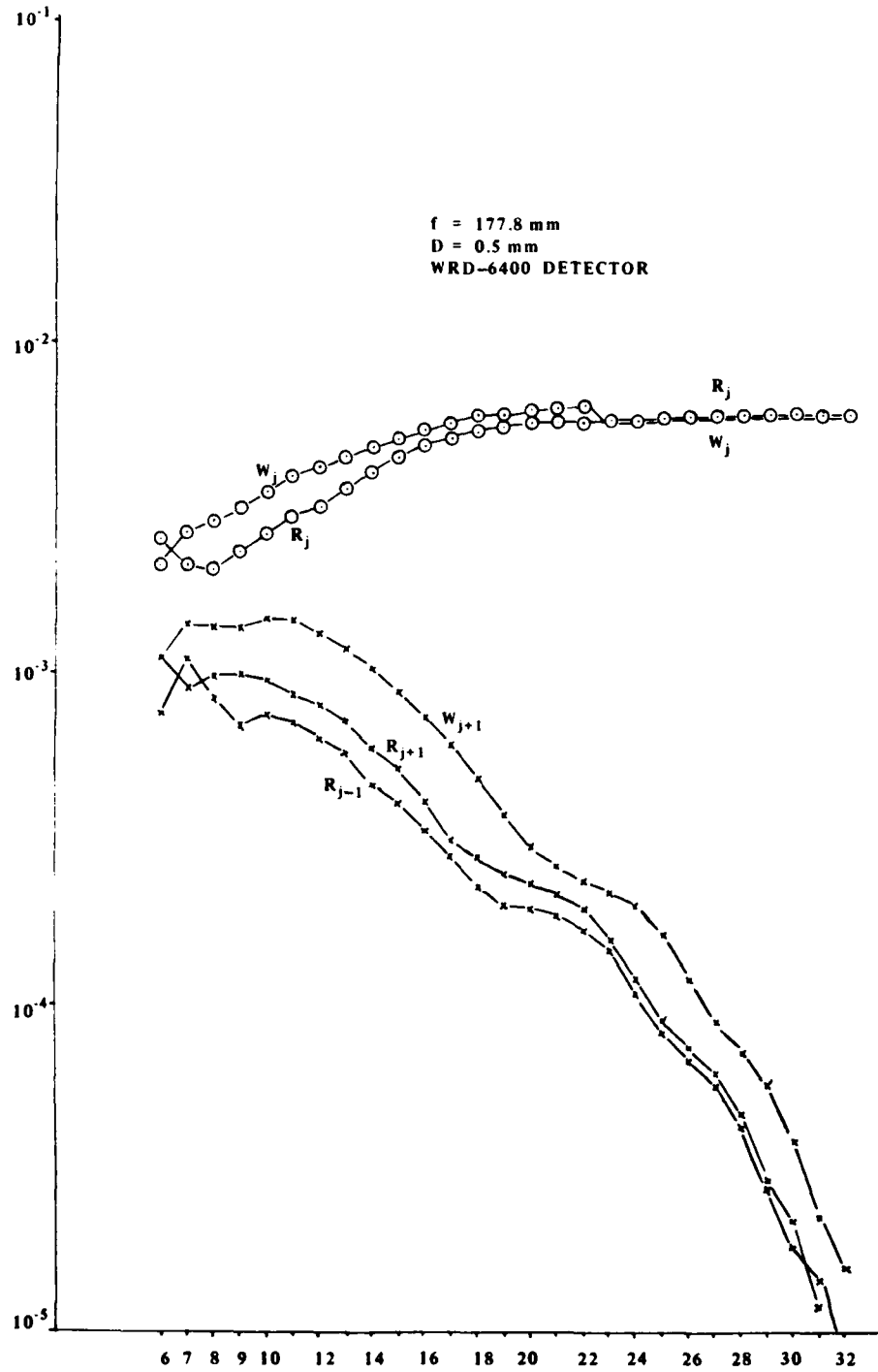


FIGURE 31. ROSA Simulation Results. H

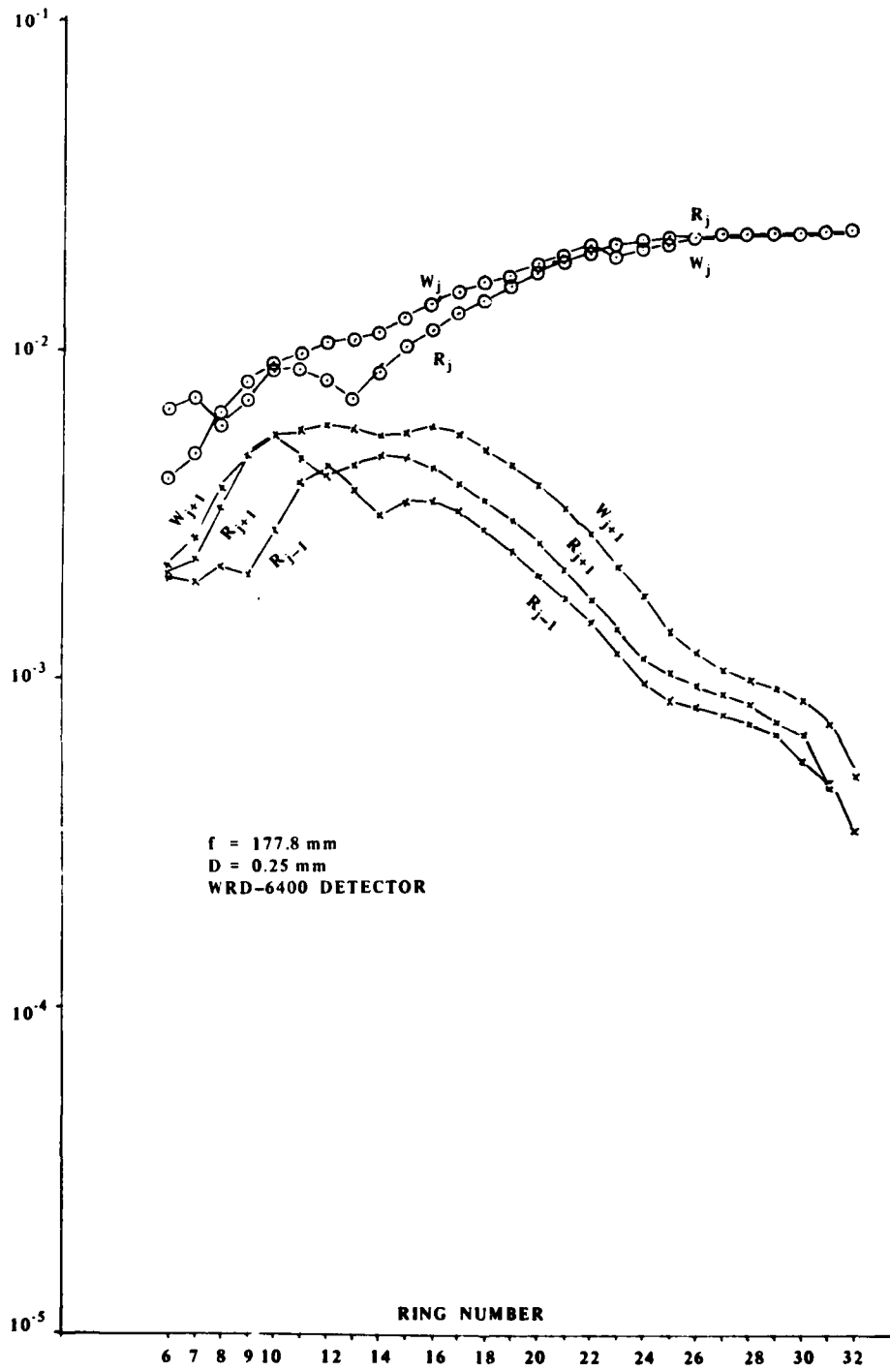


FIGURE 32. ROSA Simulation Results. I

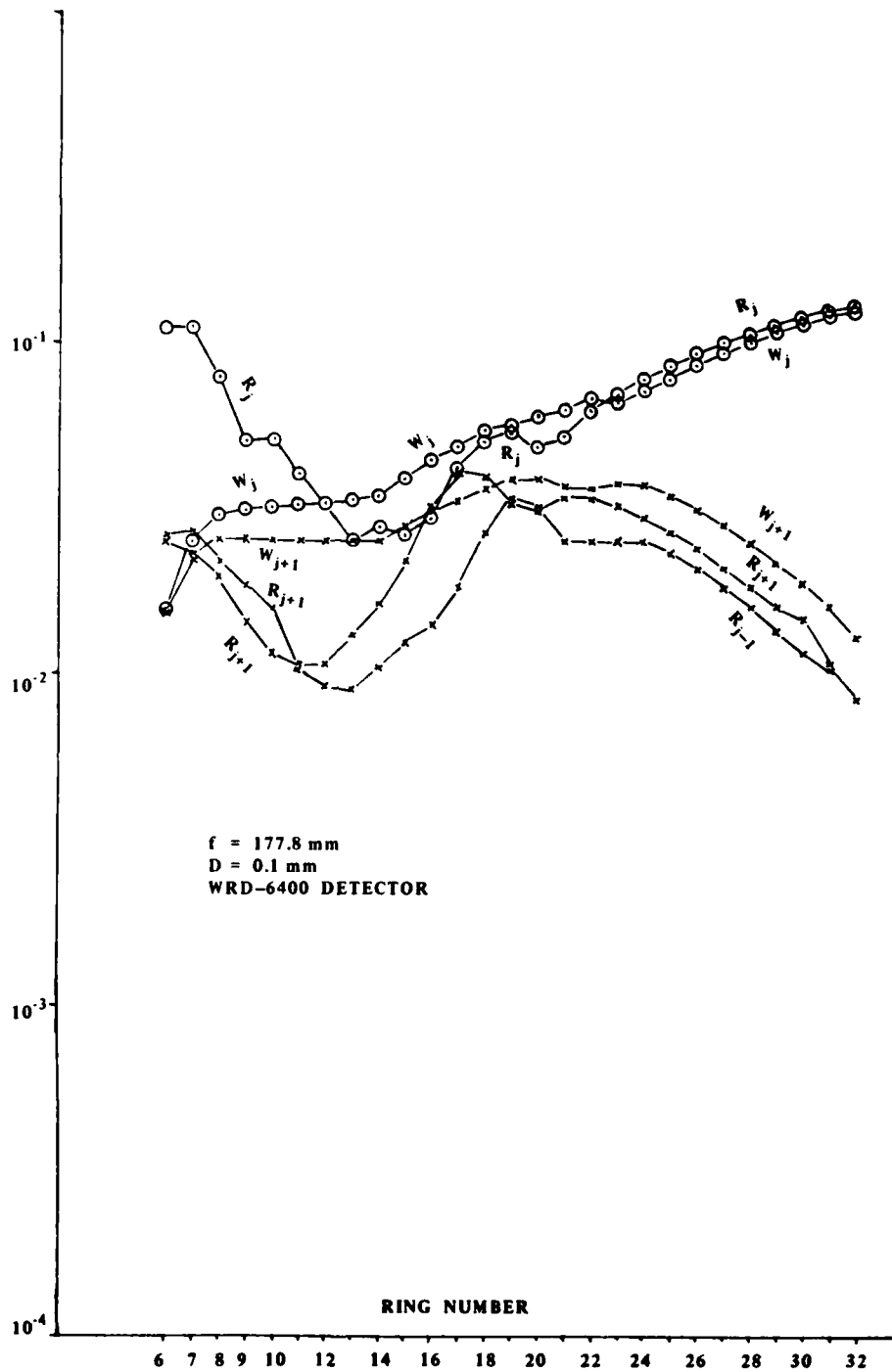


FIGURE 33. ROSA Simulation Results. J

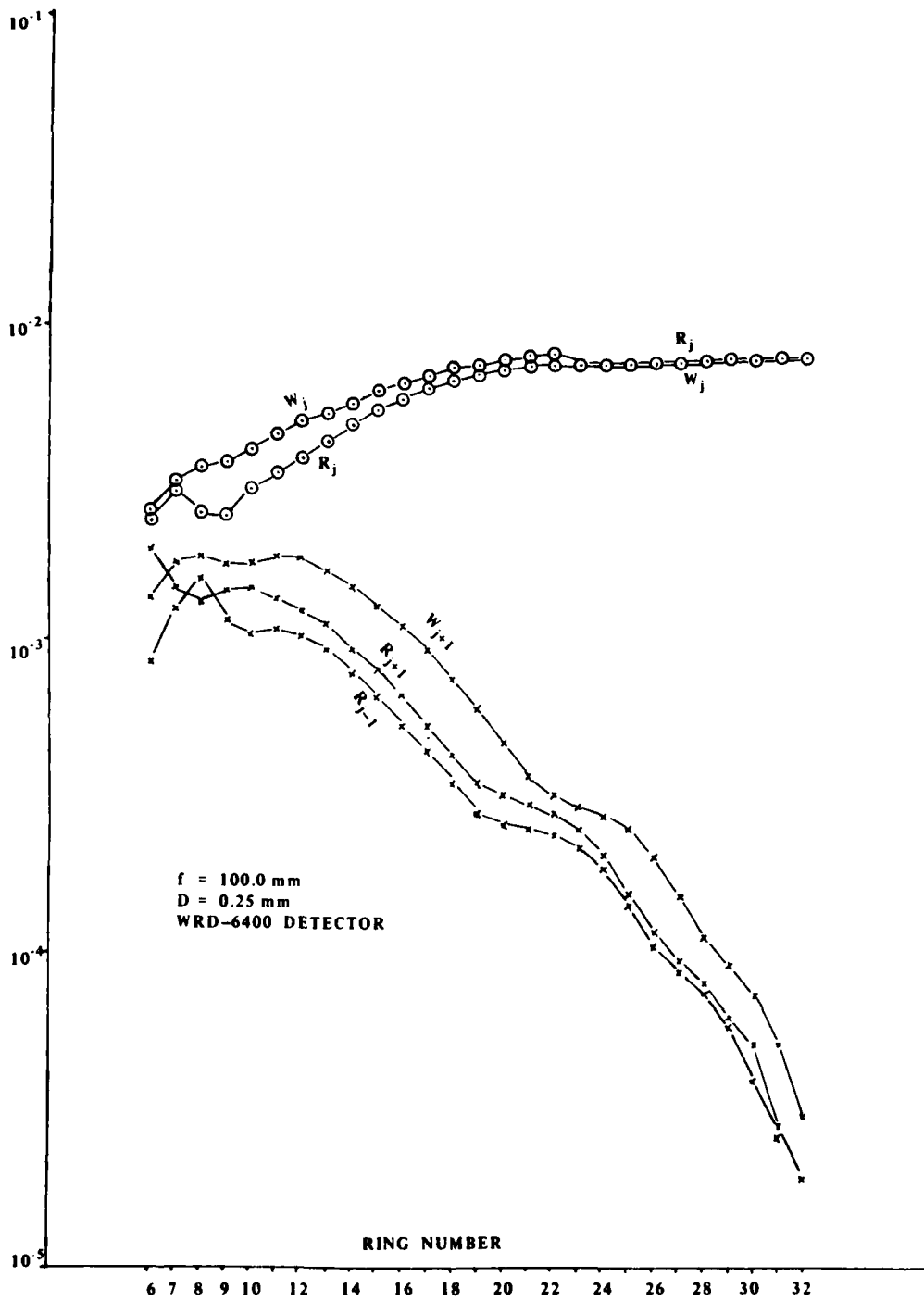


FIGURE 34. ROSA Simulation Results. K

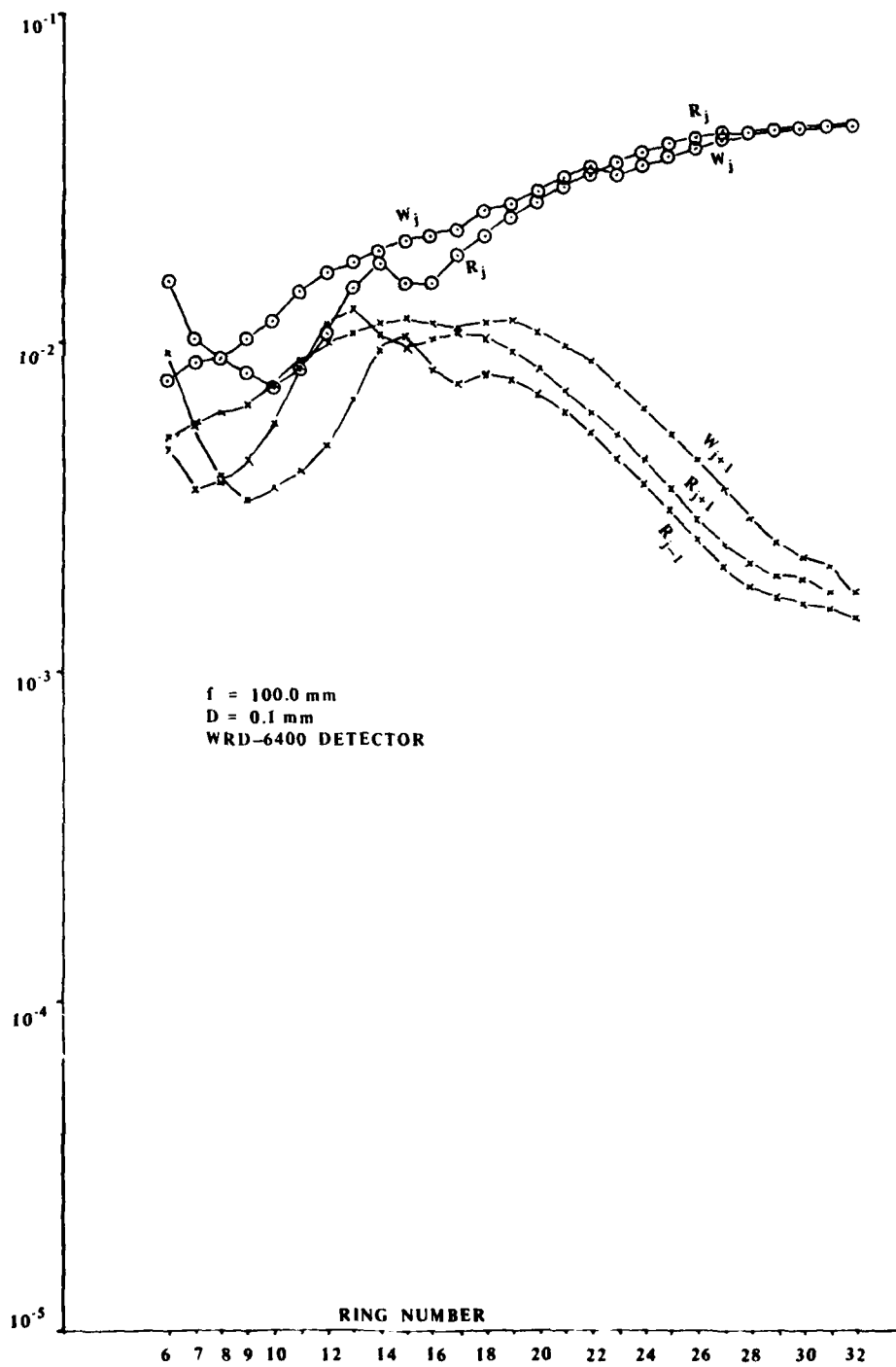


FIGURE 35. ROSA Simulation Results. L

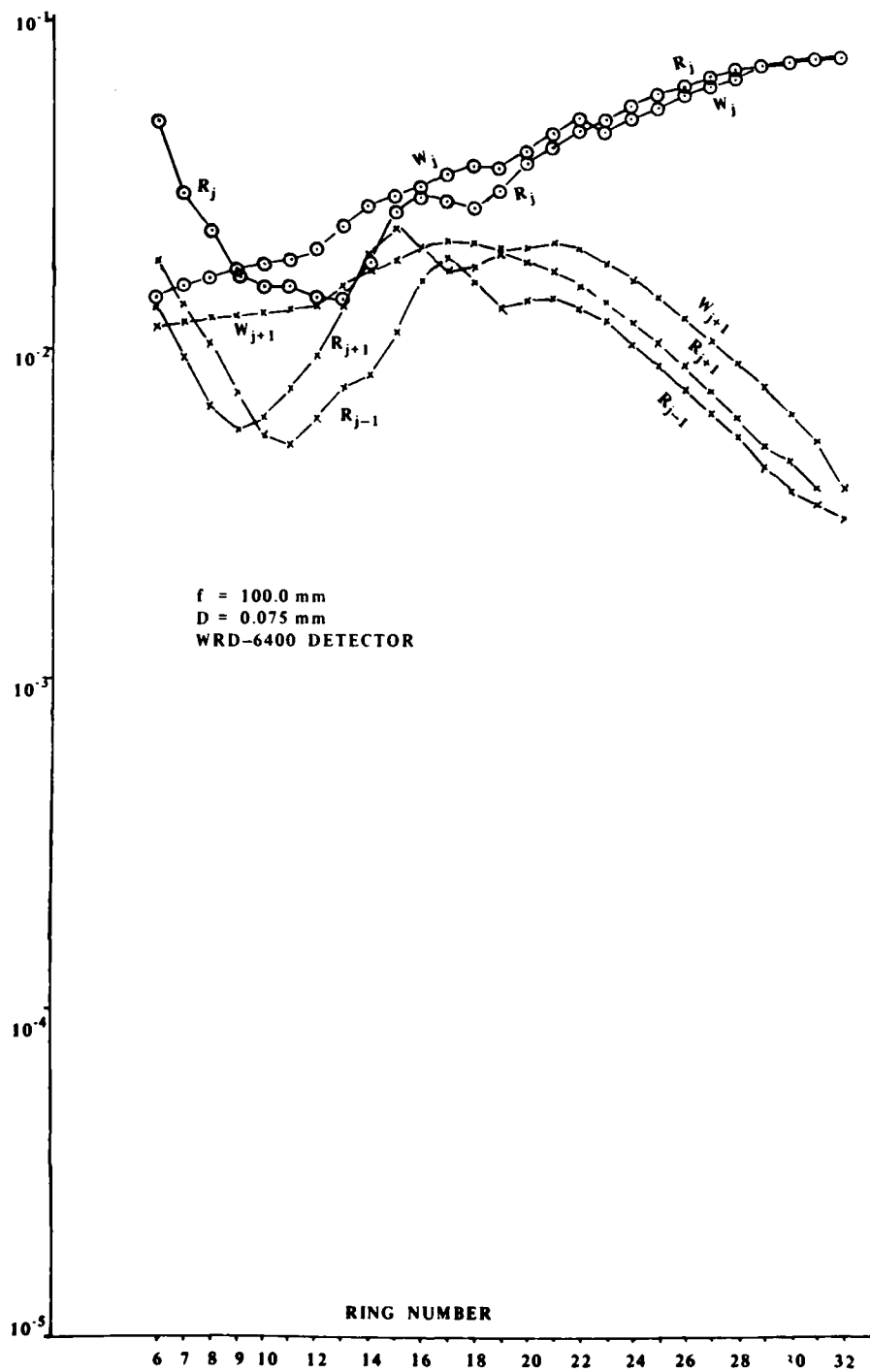


FIGURE 36. ROSA Simulation Results. M

TABLE 11. Summary of Ronchi Grating Deltas For 177.8 mm Transform Lens Focal Length (Detector WRD-6400).

Ring No.	Mid-Ring Spatial Frequency	Axial Distance of Ronchi Harmonics (mm) (Circled Distances Are Harmonics Beyond Detector)											Harmonic Delta Intensity	
		0	1	3	5	7	9	11						
6	5.19	0	0.584	1.752	2.920	4.088	5.255	6.423						
7	6.16	0	0.693	2.079	3.465	4.852	6.238	7.624						
8	7.19	0	0.809	2.427	4.045	5.663	7.281	8.899						
9	8.29	0	0.933	2.798	4.664	6.529	8.395	10.260						
10	9.50	0	1.069	3.207	5.344	7.482	9.620	11.757						
11	11.83	0	1.219	3.993	6.655	9.317	11.979	14.641						
12	12.32	0	1.386	4.158	6.931	9.703	12.475	15.248						
13	13.96	0	1.571	4.712	7.853	10.995	14.136	17.277						
14	15.83	0	1.781	5.343	8.905	12.467	16.030							
15	17.94	0	2.018	6.055	10.092	14.129	18.166							
16	20.32	0	2.286	6.859	11.431	16.004								
17	23.02	0	2.590	7.770	12.950	18.130								
18	26.06	0	2.932	8.796	14.660	20.524								
19	29.51	0	3.320	9.961	16.601									
20	33.40	0	3.758	11.274	18.789									
21	37.79	0	4.252	12.755	21.259									
22	42.72	0	4.806	14.420	24.032									
23	48.21	0	5.424	16.242										
24	54.36	0	6.116	18.348										
25	61.22	0	6.888	20.664										
26	68.35	0	7.746	23.239										
27	77.30	0	8.697	26.091										
28	86.65	0	9.749	29.247										
29	96.94	0	10.907	32.721										
30	108.27	0	12.182	36.545										
31	120.71	0	13.581	40.744										
32	134.32	0	15.113	45.338										

TABLE 12. Summary of Ronchi Grating Deltas For 100.0 mm Transform
Len. Grating Length (Detector WRD-6400).

Ring No.	Mid-Ring Spatial Frequency	Axial Distance of Ronchi Harmonics (mm) (Circled Distances Are Harmonics Beyond Detector)											Harmonic Delta Intensity
		0	1	3	5	7	9	11					
6	9.24	0	0.585	1.754	2.924	4.093	5.262	6.432	0.0008	0.0001	0.0008	6.432	
7	10.96	0	0.694	2.081	3.468	4.855	6.242	7.630				7.630	
8	12.78	0	0.809	2.426	4.044	5.661	7.278	8.896				8.896	
9	14.75	0	0.933	2.800	4.667	6.534	8.400	10.267				10.267	
10	16.90	0	1.069	3.208	5.347	7.486	9.625	11.764				11.764	
11	19.26	0	1.219	3.656	6.094	8.530	10.969	13.407				13.407	
12	21.90	0	1.386	4.157	6.929	9.701	12.472	15.244				15.244	
13	24.83	0	1.571	4.714	7.856	10.999	14.141	17.284				17.284	
14	28.14	0	1.781	5.342	8.903	12.465	16.026						
15	31.89	0	2.018	6.054	10.090	14.126	18.162						
16	36.13	0	2.286	6.859	11.432	16.004							
17	40.92	0	2.589	7.768	12.947	18.126							
18	46.34	0	2.932	8.797	14.622	20.527							
19	52.47	0	3.320	9.961	16.602								
20	59.39	0	3.758	11.275	18.791								
21	67.19	0	4.252	12.755	21.259								
22	75.94	0	4.805	14.416	24.027								
23	85.71	0	5.424	16.271									
24	96.65	0	6.116	18.348									
25	108.86	0	6.889	20.666									
26	122.41	0	7.746	23.238									
27	137.44	0	8.697	26.092									
28	154.05	0	9.748	29.245									
29	172.35	0	10.906	32.719									
30	192.51	0	12.182	36.546									
31	214.62	0	13.581	40.743									
32	238.83	0	15.113	45.333									

The simulation data for the WRD-6400 detector becomes particularly ill-behaved for both transform lens focal lengths when the sampling aperture has a diameter of 0.1 mm or less. An example of the manner in which a S/N value less than 1.0 is obtained for the $f = 100.0$ mm, $D = 0.1$ mm data shown in figure 35 is illustrated in figure 37 where the sections through the zero and first-order harmonics have been plotted for the first harmonic centered on Ring 12. If we algebraically add the two curves, square the results, and then integrate over the Ring 12 and Ring 13 areas, we find that the R_j/R_{j+1} is less than one.

It will also be noted that the wedge data have lower S/N ratios for the WRD-6400 detector because of the smaller wedge angles when compared to those of the WRD-6420 detector.

Table 13 summarizes the number of detector elements with S/N greater than 1.0 for Data Set 1B. When this data is compared with the similar data in table 10 for the WRD-6420 detector, we see more rings with S/N greater than 1.0, but it must be remembered that the S/N are in general lower, especially for the lower and middle detector rings, as shown in figures 38 and 39 for $f = 100.0$ mm and $D = 0.1$ mm.

3. Data Set 2A - Ronchi Grating Deformation. Table 5 lists the simulation conditions under which Data Set 2A was obtained. The purpose of this data set was to examine the change in S/N when the Ronchi grating was subjected to simple linear deformations. These linear deformations were obtained by multiplying the mid-ring spatial frequency by a factor that had a value between 0.96 and 1.04. Note that this is not the equivalent to selecting a deformation and then computing the S/N values for each ring detector element. For example, a 4 percent deformation having its first harmonic centered on Ring 7 for $f = 100.0$ mm with the WRD-6420 detector is only 0.051 mm; whereas, the same percent of deformation for the Ring 32 spatial frequency would amount to a deformation of 0.620 mm. In either case, however, the effect of the deformation is to move the position of the first harmonic grating function from its mid-ring position. Figures 38 and 39 plot the mid-ring S/N values for R_j/R_{j-1} and R_j/R_{j+1} for the WRD-6420 and the WRD-6400 detector respectively when $f = 100.0$ mm and $D = 0.10$ mm. Table 14 lists the S/N values for grating deformations associated with the WRD-6420 detector. Figure 38 plots S/N values for no deformation ($f = 1.0$) while figure 40 plots S/N for selected rings from table 14. Table 15 is similar to that of table 14, except that $D = 0.075$ mm instead of 0.10 mm.

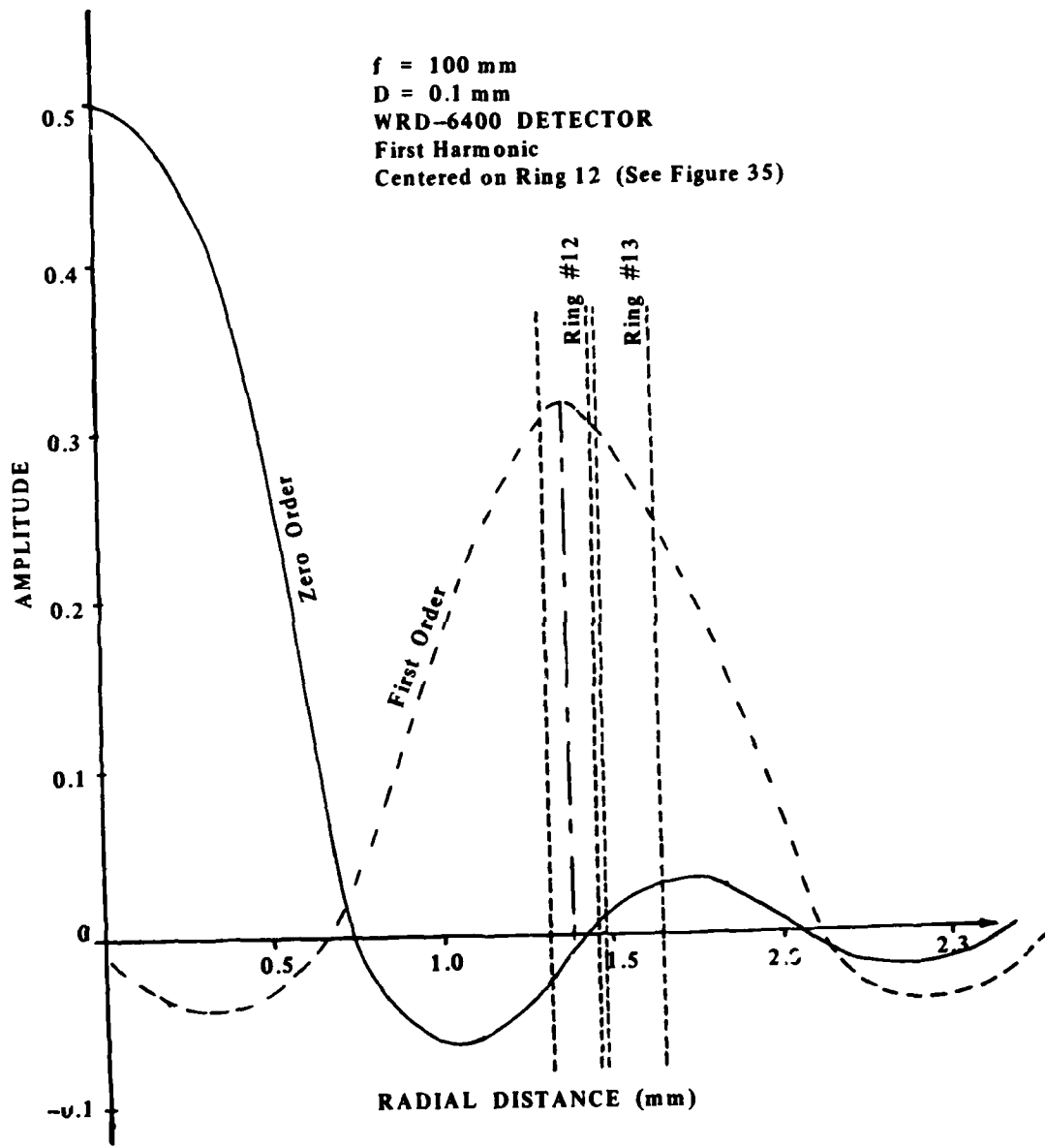
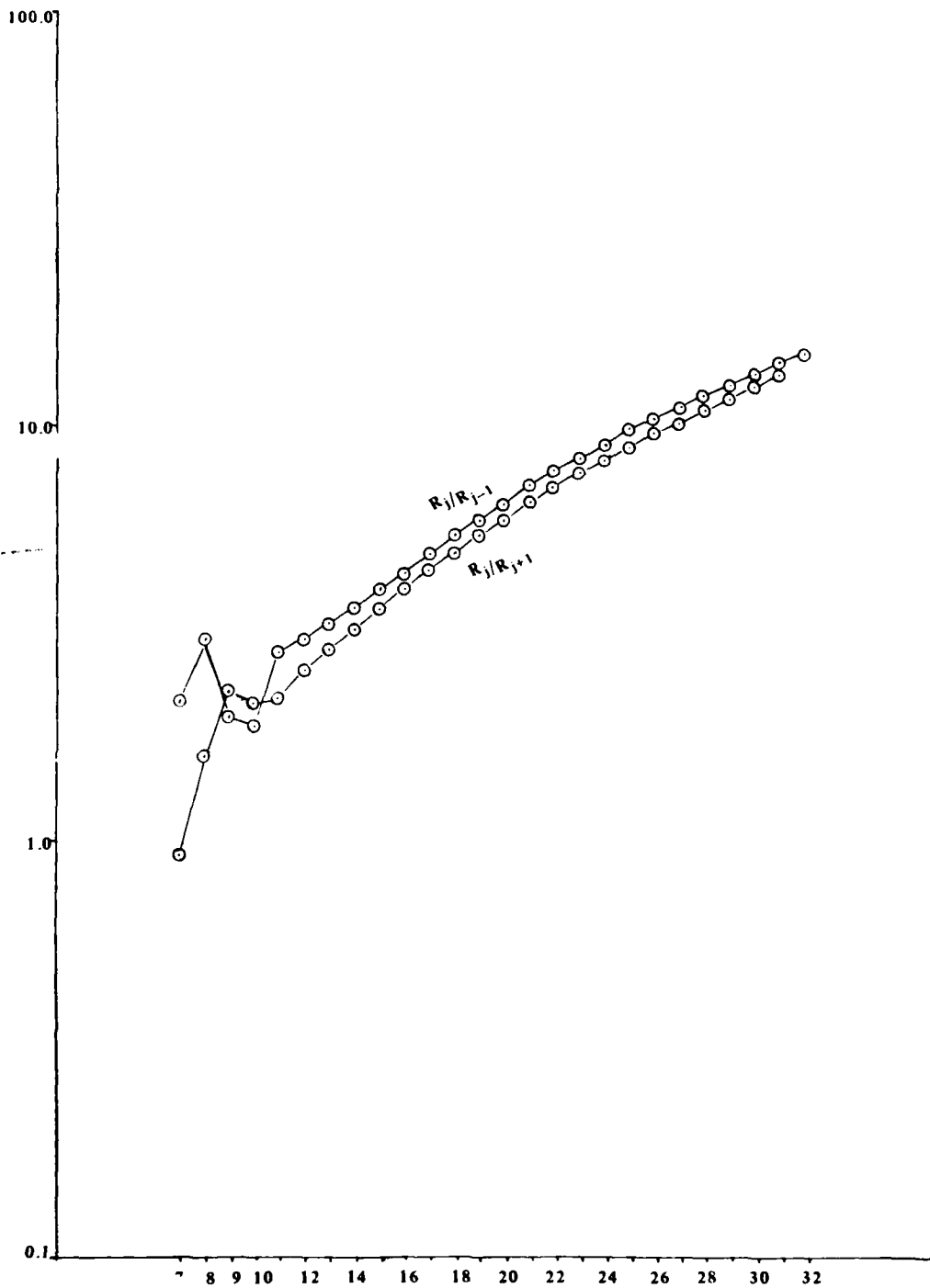


FIGURE 37. Example for S/N Less Than 1.0.

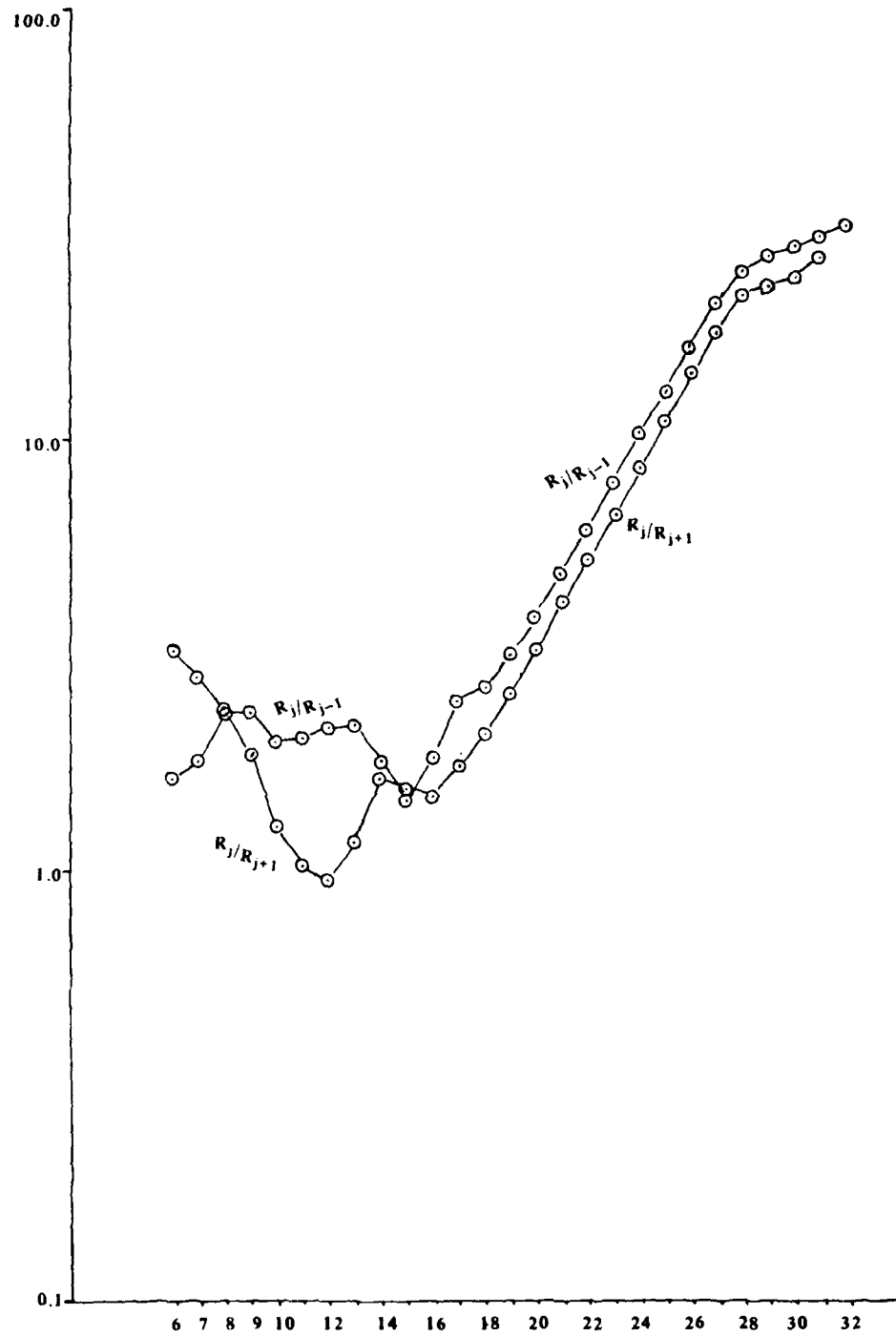
TABLE 13. Detector Elements with $S/N > 1$ In Data Set 1B.

	f	D	f/D	Number of Detector Elements with $S/N > 1$	
				Rings	Wedges
Fig. 31	177.8 mm	0.5 mm	355	27	32
32	177.8 mm	0.25 mm	711	27	32
33	177.8 mm	0.10 mm	1778	26	32
34	100.0	0.25 mm	400	27	32
35	100.0	0.10 mm	1000	26	32
36	100.0	0.075 mm	1333	26	32



Note: S/N for R_j/R_{j-1} and R_j/R_{j+1} When $f = 100.0$ mm, $D = 0.1$ mm, and WRD-6420 DETECTOR.

FIGURE 38. Signal-to-Noise Plots. A



Note: S/N for R_j/R_{j-1} and R_j/R_{j+1} When $f = 100.0$ mm, $D = 0.1$ mm, and WRD-6400 DETECTOR.

FIGURE 39. Signal-to-Noise Plots. B

TABLE 14. S/N for Ronchi Grating Deformations, (Grating Freq. = Factor X Mid-Radius Freq.)
 $f = 100.0 \text{ mm}, D = 0.1 \text{ mm}, (\text{Detector WRD-6400}).$

Ring No.	P_j/P_{j-1} FACTOR	R_j/R_{j+1} FACTOR	Ring No.	0.96	0.97	0.98	0.99	1.00	1.01	1.02	1.03	1.04
7	1.31	1.98	2.06	2.13	2.20	2.28	2.36	2.44	2.52	1.04		
8	2.45	2.60	2.76	2.93	3.09	3.30	3.51	3.73	3.96			
9	1.51	1.61	1.73	1.85	2.00	2.13	2.29	2.46	2.65			
10	1.30	1.43	1.57	1.73	1.90	2.10	2.32	2.56	2.83			
11	1.73	1.96	2.23	2.53	2.86	3.27	3.72	4.22	4.77			
12	1.63	1.95	2.26	2.63	3.09	3.57	4.00	4.89	5.71			
13	1.61	1.93	2.30	2.77	3.31	4.04	4.92	5.98	7.30			
14	1.51	1.92	2.37	2.94	3.67	4.53	5.49	7.22	9.01			
15	1.51	1.86	2.44	3.13	4.06	5.23	6.78	8.75	11.05			
16	1.44	1.90	2.51	3.33	4.42	5.97	7.98	10.48	13.13			
17	1.33	1.89	2.59	3.57	4.97	6.99	9.43	12.50	15.20			
18	1.29	1.84	2.62	3.76	5.45	7.79	10.64	14.18	16.26			
19	1.22	1.80	2.67	4.00	5.96	8.87	12.58	15.91	17.01			
20	1.12	1.72	2.67	4.16	6.50	9.90	13.98	16.92	16.83			
21	1.04	1.68	2.73	4.44	7.22	11.27	15.71	17.94	16.65			
22	0.95	1.61	2.72	4.64	7.81	12.42	16.91	18.24	16.06			
23	0.95	1.51	2.67	4.76	8.35	13.48	17.94	18.34	15.54			
24	0.77	1.43	2.65	4.95	9.02	14.77	19.00	18.48	15.20			
25	0.77	1.36	2.65	5.18	9.80	16.14	19.97	18.53	14.94			
26	0.62	1.26	2.58	5.30	10.43	17.30	20.65	18.50	14.67			
27	0.55	1.17	2.51	5.40	11.06	18.42	21.28	18.35	14.32			
28	0.43	1.10	2.47	5.59	11.90	19.80	21.81	18.34	14.21			
29	0.43	1.01	2.39	5.68	12.63	20.98	22.19	18.25	14.04			
30	0.37	0.92	2.29	5.73	13.32	22.04	22.38	18.07	13.80			
31	0.33	0.84	2.21	5.85	14.18	23.27	22.65	18.17	13.86			
32	0.22	0.77	2.10	5.86	14.98	24.12	22.63	18.12	14.64			

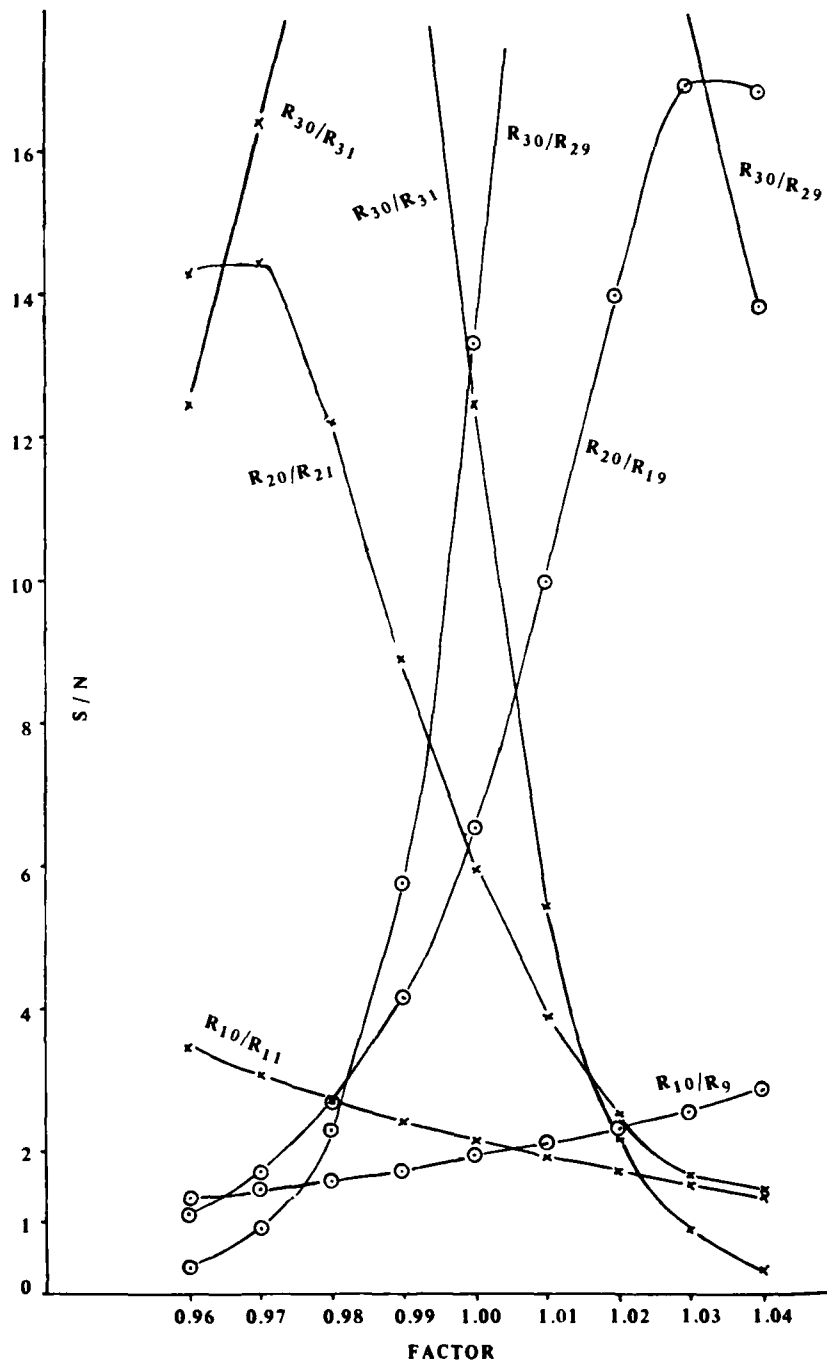


FIGURE 40. Plots of Selected Data From Table 14.

TABLE 15. S/N for Ronchi Ruling Deformations (Grating Freq. = Factor X Mid-Radius Freq.)
 $f = 100.0$ mm, $D = 0.075$ mm, (Detector WRD-6400).

Ring No.	R_j/R_{j-1} FACTOR				Ring No.	R_j/R_{j+1} FACTOR								
	0.96	0.98	0.99	1.00		1.01	1.02	1.04						
7	0.94	0.99	1.02	1.05	1.09	1.12	1.20	1.21	1.15	1.13	1.11	1.08	1.02	1.04
8	1.54	1.66	1.72	1.78	1.84	1.95	2.00	1.11	1.02	0.97	0.93	0.89	0.80	0.78
9	1.90	2.06	2.15	2.24	2.34	2.43	2.97	1.12	1.04	1.00	0.97	0.93	0.89	0.82
10	1.84	2.04	2.16	2.28	2.42	2.56	2.88	2.21	1.95	1.84	1.73	1.63	1.54	1.37
11	1.13	1.28	1.37	1.45	1.55	1.65	1.87	2.52	2.15	1.99	1.84	1.71	1.58	1.36
12	1.16	1.37	1.49	1.63	1.77	1.94	2.32	2.37	1.94	1.76	1.58	1.46	1.33	1.10
13	1.45	1.79	1.99	1.56	2.46	2.74	3.41	2.64	2.09	1.86	1.17	1.49	1.34	1.08
14	1.45	1.84	2.08	2.32	2.68	3.04	3.95	3.31	2.50	2.18	1.91	1.67	1.47	1.14
15	1.33	1.77	2.05	2.37	2.76	3.22	5.12	3.96	2.85	2.43	2.08	1.78	1.53	1.14
16	1.29	1.79	2.12	2.51	2.99	3.58	5.22	4.67	3.20	2.66	2.22	1.86	1.57	1.12
17	1.27	1.84	2.24	2.72	3.34	4.11	6.33	5.66	3.68	2.98	2.42	1.98	1.63	1.10
18	1.21	1.86	2.31	2.90	3.65	4.63	7.50	6.72	4.19	3.30	2.61	2.08	1.66	1.07
19	1.16	1.88	2.41	3.10	4.03	5.26	8.92	8.04	4.84	3.70	2.85	2.20	1.71	1.04
20	1.10	1.89	2.50	3.32	4.44	5.98	10.43	9.26	5.48	4.09	3.05	2.28	1.72	0.99
21	1.06	1.93	2.63	3.62	5.01	6.96	12.22	10.68	6.36	4.61	3.33	2.42	1.77	0.96
22	1.00	1.94	2.72	3.87	5.54	7.90	13.49	11.75	7.22	5.12	3.58	2.52	1.78	0.91
23	0.93	1.93	2.80	4.12	6.10	8.90	14.37	12.44	8.15	5.67	3.85	2.62	1.79	0.85
24	0.87	1.93	2.91	4.44	6.80	10.11	14.88	12.80	9.22	6.33	4.18	2.74	1.81	0.80
25	0.81	1.94	3.04	4.81	7.60	11.41	14.81	12.81	10.25	6.99	4.48	2.84	1.81	0.74
26	0.74	1.93	3.14	5.17	8.42	12.68	14.42	12.63	11.40	7.78	4.85	2.97	1.82	0.69
27	0.68	1.90	3.22	5.50	9.19	13.74	13.71	12.17	12.36	8.50	5.18	3.05	1.80	0.63
28	0.62	1.89	3.33	5.92	10.15	14.91	13.06	11.75	13.31	9.30	5.54	3.15	1.78	0.58
29	0.56	1.86	3.43	6.33	11.10	15.88	12.43	11.32	14.22	10.16	5.93	3.24	1.76	0.53
30	0.50	1.82	3.50	6.72	11.98	16.62	11.85	10.88	14.95	10.98	6.29	3.32	1.73	0.47
31	0.45	1.78	3.57	7.14	12.95	17.32	11.40	10.52	15.68	11.90	6.72	3.41	1.71	0.43
32	0.40	1.73	3.62	7.52	13.82	17.77	10.96	-	-	-	-	-	-	-

4. Data Set 2B - Ronchi Grating Rotation. This data set, as shown in table 16, was obtained to investigate S/N values when the Ronchi gratings were rotated from the wedge bisector. The f and D conditions under which the data were obtained are the same as figure 38 and table 14. The results, as expected, show a decrease to a S/N value of 1.0 when the grating is rotated 2.5° , neglecting a small but finite separator between wedges.

5. Data Set 3A - Equal Ring Width Detector. In section 4, the simulation data indicated response differences for the two detectors. This motivated an attempt to redesign the ROSA detector to perform better. Data Set 3A represents simulation data from a detector with equal ring spacing when $D = 0.1$ mm and the transform lens focal length were 100.0, 150.0, and 200.0 mm.

A summary for a ROSA type, equal ring width detector is tabulated in table 17. This detector had 32 rings and 32 wedges, with the mid-ring radii 0.5 mm apart and with 0.0254 mm (1.0 mil) allowance for detector element separators. Table 17 gives the mid-ring spatial frequencies for $f = 100.0$ mm, $f = 150.0$ mm, and $f = 200.0$ mm and the Ronchi grating delta positions when the first harmonic was positioned at the mid-ring. These detector data can be compared with similar data in tables 2, 3, 7, 8, 11, and 12.

Simulation data for the equal ring width detector are plotted in figures 41 through 43 for $D = 0.1$ mm and $f = 100.0$ mm, $f = 150.0$ mm, and $f = 200.0$ mm, respectively. For a quick appraisal of the results, compare figure 41 with figure 26 and figure 35, and note that although the absolute response is reduced for the rings and wedges, the S/N is increased and almost constant for the rings. Additionally, note that rings 3 through 32 and wedges 3 through 32 all have S/N greater than 1.0. Figures 42 and 43 indicate that S/N decreases with increased transform lens focal length, and the noise seen in figure 40, for the lower rings, becomes more severe as f increases. Table 18 summarizes the number of detector elements with S/N greater than 1.0 for Data Set 3A.

6. Data Set 3B - Modified Equal Ring Width Detector. Although there were noisy variations in the simulation data for Data Set 3A for the lower rings, a brief attempt was made to adjust ring width to minimize this noise. However, these attempts were unsatisfactory, and the data appears in appendix B as indicated in table 5.

TABLE 16. S/N For Grating Rotations From Wedge Bisector. $f = 100.0$ mm.
 $D = 0.1$ mm. (Detector WRD-6420).

Ring	ROTATION FROM WEDGE BISECTOR					
	$\phi = \phi.0$	$\phi = 0.5^\circ$	$\phi = 1.0^\circ$	$\phi = 1.5^\circ$	$\phi = 2.0^\circ$	$\phi = 2.5^\circ$
7	1.62	1.52	1.39	1.26	1.13	1.00
8	1.57	1.48	1.36	1.24	1.12	1.00
9	1.61	1.50	1.38	1.25	1.12	1.00
10	1.71	1.58	1.43	1.28	1.14	1.00
11	1.88	1.71	1.53	1.34	1.16	1.00
12	2.01	1.80	1.59	1.38	1.18	1.00
13	2.08	1.83	1.59	1.37	1.17	1.00
14	2.40	2.05	1.74	1.46	1.21	1.00
15	2.77	2.31	1.90	1.55	1.25	1.00
16	3.24	2.62	2.10	1.66	1.29	1.00
17	3.33	2.61	2.04	1.61	1.27	1.00
18	4.01	3.03	2.29	1.73	1.32	1.00
19	4.81	3.51	2.56	1.87	1.37	1.00
20	5.74	4.06	2.86	2.01	1.42	1.00
21	6.79	4.67	3.18	2.16	1.47	1.00
22	8.00	5.34	3.51	2.31	1.52	1.00
23	9.43	6.10	3.87	2.45	1.56	1.00
24	11.14	6.98	4.26	2.61	1.61	1.00
25	13.16	8.04	4.71	2.77	1.66	1.00
26	15.41	9.29	5.24	2.96	1.71	1.00
27	17.63	10.75	5.87	3.18	1.77	1.00
28	19.82	12.33	6.59	3.43	1.83	1.00
29	21.12	13.98	7.43	3.73	1.91	1.00
30	23.41	16.14	8.51	4.09	2.00	1.00
31	28.53	20.42	10.38	4.64	2.12	1.00
32	16.52	13.50	8.62	4.41	2.10	1.00

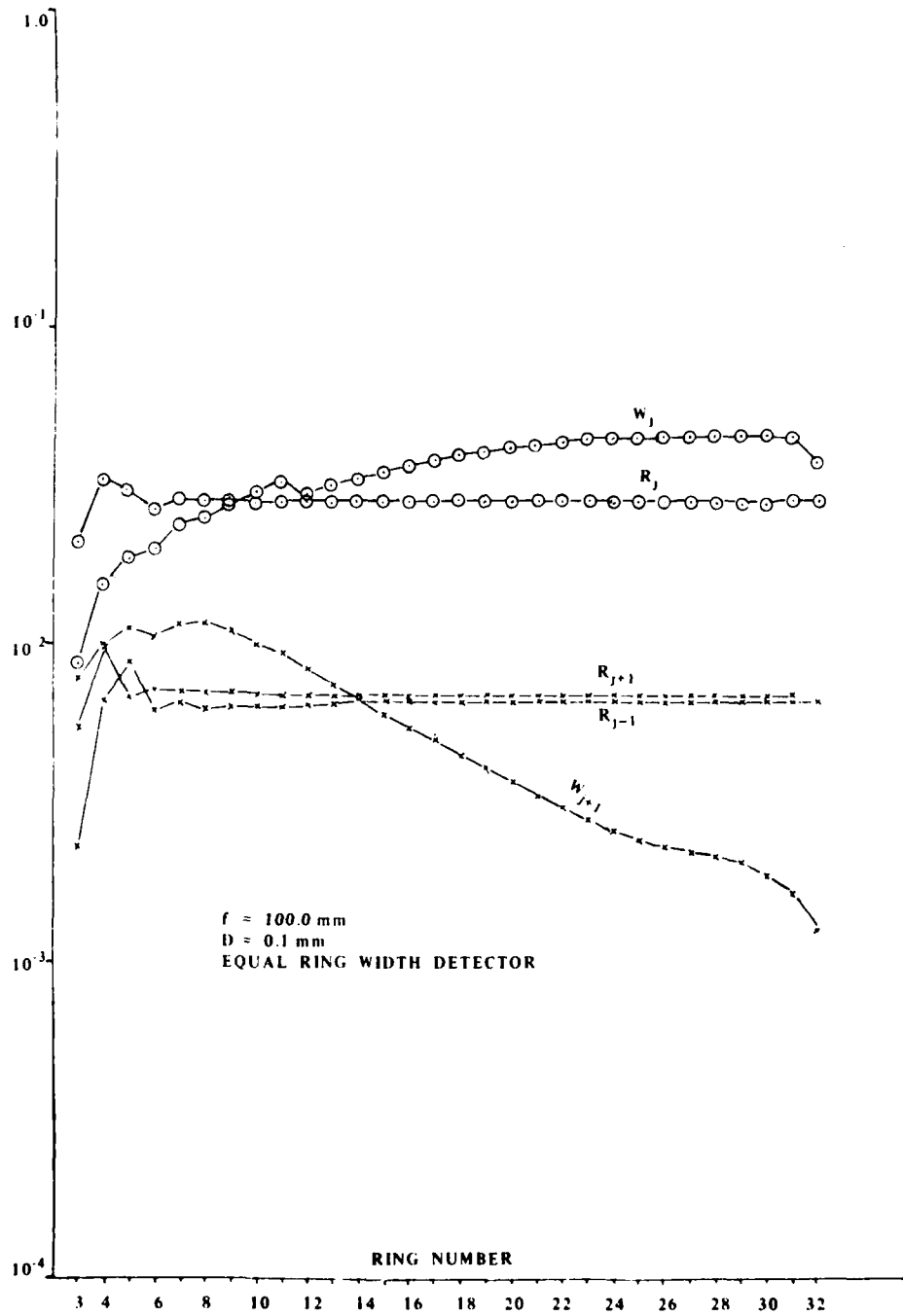


FIGURE 41. ROSA Simulation Results. N

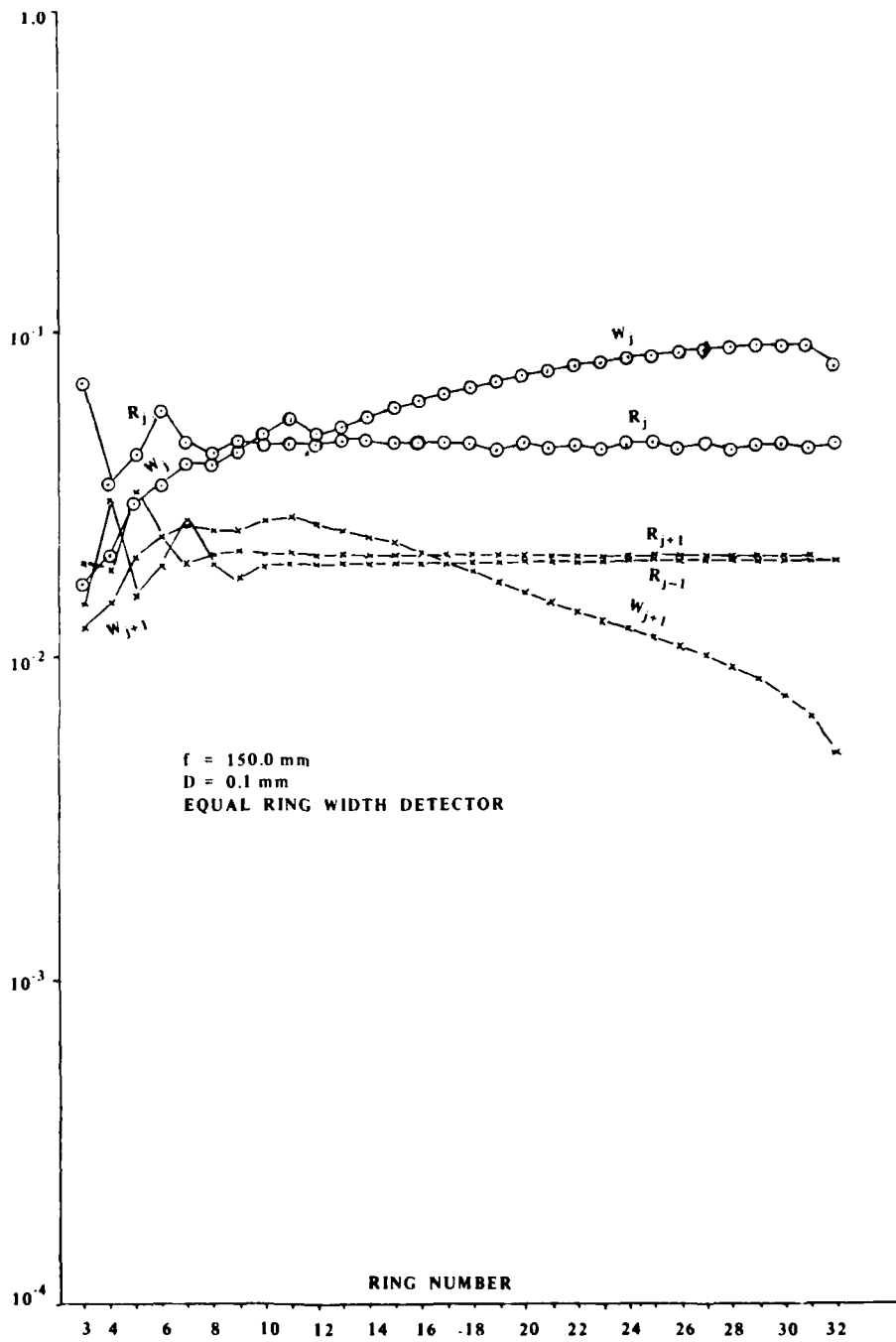


FIGURE 42. ROSA Simulation Results. O

AD-A110 795

ARMY ENGINEER TOPOGRAPHIC LABS FORT BELVOIR VA F/G 5/2
OPTICAL POWER SPECTRAL ANALYSIS FOR MACHINE-READABLE FACTOR MAP--ETC(U)
DEC 80 R D LEIGHTY
ETL-0212

NL

UNCLASSIFIED

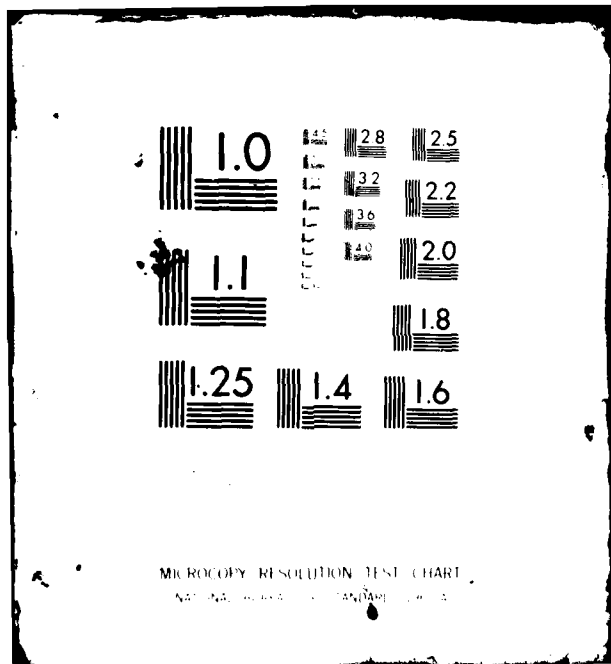
2 - 2

20
A 079

■



END
DATE
FILMED
3 82
DTIC



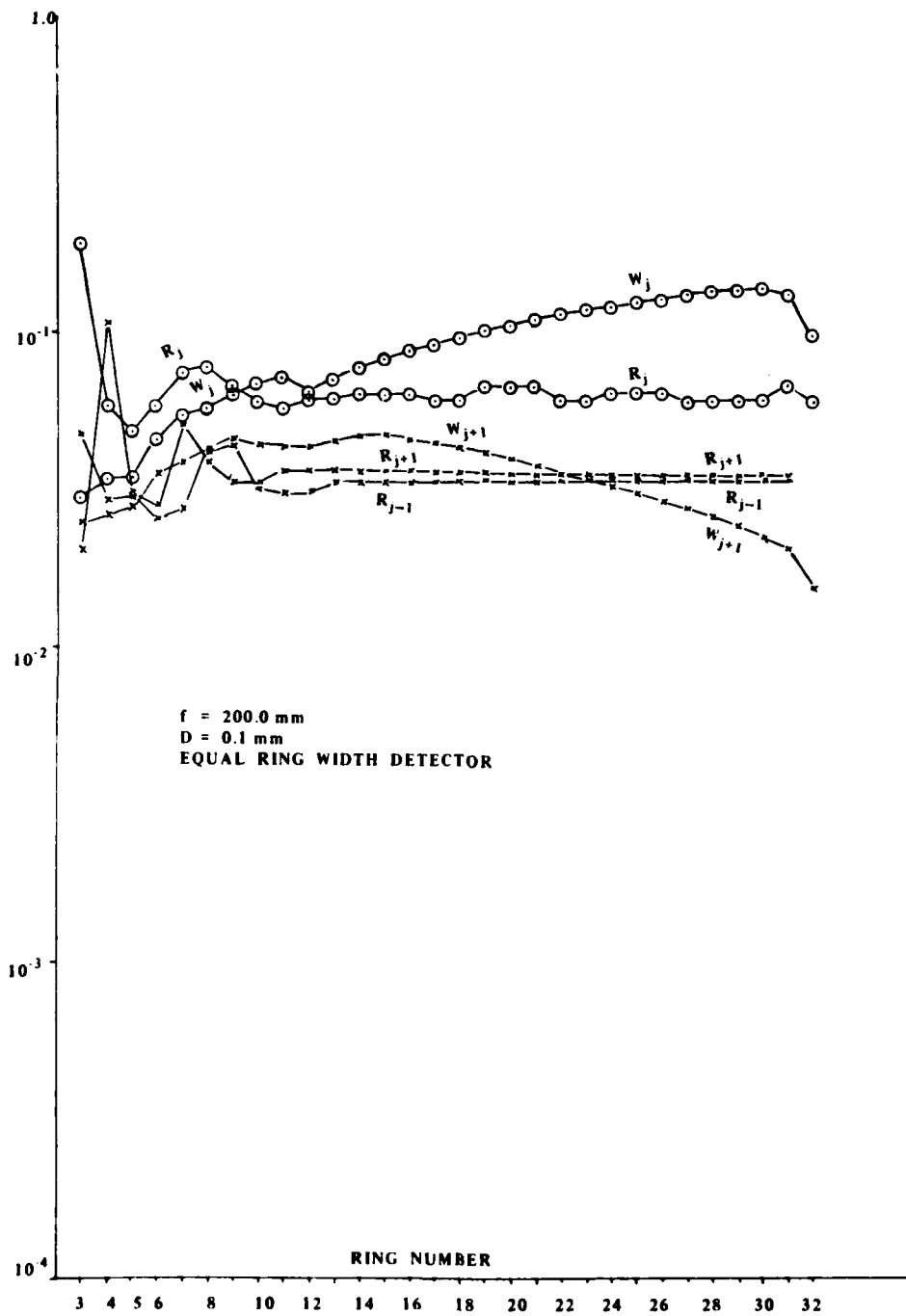


FIGURE 43. ROSA Simulation Results. P

TABLE 18. Detector Elements With $S/N > 1$ In Data Set 3A
(Equal Ring Width Detector).

	f	D	f/D	Number of Detector Elements with S/N>1	
				Rings	Wedges
Fig. 40	100.0 mm	0.1 mm	1000	30	32
41	150.0	0.1	1500	30	32
42	200.0	0.1	2000	29	32

V. PRELIMINARY OPTICAL SUBSYSTEM DESIGN FOR GRATING MAP SYSTEMS

In the preceding section, we determined that Ronchi gratings having spatial frequencies, such that the first harmonic of the grating transform is positioned at the mid-radius of the detector ring, would yield a unique detection of the grating frequency if the sampling aperture diameter and transform lens focal length are properly selected. In that section, we also determined that the direction of the Ronchi ruling could be determined uniquely if the grating was aligned perpendicular to the bisector of a detector wedge. In this section, we will be more pragmatic and will consider the preliminary optical subsystem design of grating map systems. We will see how optical system parameters affect the amount of information that can be recorded, and we will see how the interaction of parameters force the optical designers to make trade-offs for realistic optical system specifications. Yet we will not have enough information to design a system because of the dependence upon the grating fabrication capability, which will be discussed in the following section.

A. Basic Optical Subsystem Design. • Suppose we have a Ronchi grating map fabrication capability with a minimum writing spot diameter d . The maximum grating spatial frequency of the recorder system is then

$$w_{max} = 1/2d \quad (34)$$

and the minimum period of the grating is

$$P_{min} = 1/w_{max} = 2d \quad (35)$$

Knowing the dimensions of the frequency plane detector, we can use the relation

$$f = R_{max}/\lambda w_{max} \quad (36)$$

to determine the transform lens focal length f of the system, given the mid-radius of the most distant detector ring R_{max} and the wavelength λ of the laser light.

The minimum detectable grating spatial frequency w_{min} is related to the sampling aperture diameter D . To show this relationship, we note that

$$w_{min} = 1/P_{max} \quad (37)$$

where P_{max} represents the Ronchi grating period associated with the minimum grating spatial frequency w_{min} . We know that the Ronchi grating period must be less than the sampling aperture diameter D to enable detection of Ronchi frequency spectra. We choose

$$P_{max} \leq D/N \quad (38)$$

where the factor $N = 2.5$ enables at least 2.5 periods of the grating to be sampled with safety; a factor smaller than 2.0 will result in frequency spectra of a line or a line and an edge. Thus, the minimum detectable Ronchi grating spatial frequency should be

$$w_{min} \geq 2.5/D \quad (39)$$

For example, if $D = 0.1$ mm, then a choice for w_{min} would be 25 lp/mm. A clear choice for w_{min} can be obtained by the association

$$w_{min} = R_{min}/\lambda f \quad (40)$$

where R_{min} is the mid-radius of the detector ring closest to the optical axis that will satisfy equation (39).

Sampling aperture diameter D and transform lens focal length f also influence S/N as the simulation data in the previous section indicates. For an $f^\#$ less than 1000, i.e.

$$f^\# = f/D < 1000 \quad (41)$$

the simulation assures $S/N > 1.0$ for WRD-6420 detectors for 26 rings and 32 wedges (table 10) or 27 rings and 32 wedges for the WRD-6400 detectors (table 13). Higher $f^\#$ combinations can be used as indicated in tables 13 and 18.

The diameter of the sampling aperture, coupled with detector responsivity, will determine the power requirements for the system's laser light source. (Data are not available on laser power requirements at this time.) Available laser power, sample aperture diameter, and detector responsivity will determine the maximum sample rates and decision-making software that can be optimized to operate within these constraints. Sampling and decision-making should be possible at microsecond rates.

Selection of the sampling aperture diameter is of major importance for the S/N of the detected signal, and it determines the resolution of the factor map sampling. Selection of the sampling aperture diameter should be consistent with the precision of

the factor map. Table 19 indicates the relation between selected sampling aperture diameters for various map reduction ratios and their equivalent diameters when projected onto a map or the ground surface. For example, a 22" x 29" (558.8 mm x 736.6 mm) factor map having a scale of 1:50,000 when reduced 10x will have a format size of 55.9 by 73.7 mm, which is suitable for commercial 70-mm chips or roll films. If a 0.1 mm diameter sampling aperture is used for grating detection at this reduction, it has an equivalent of 50 meters on the ground. Complete readout of the factor map could be accomplished with 411,612 samples. Knowing the aperture diameter and sample spacing and knowing the format size of the grating map can be used to establish specifications for the optical or mechanical scanning components.

B. System Design Trade-Offs. • For any given set of design parameters, there is sufficient motivation to investigate approaches that will yield a more cost-effective system design. One potential means for accomplishing this design is to put more factor maps on the same recording material. For example, above we indicated that a 70-mm chip could be used to encode grating maps with 10x reduction, and if we now consider 35-mm grating maps with a 20x reduction, then we could put four grating maps on a 70-mm film chip. Likewise 16 separate 16-mm grating maps might fit on a 70-mm film chip with 40x reduction, and with 65x reduction 98 separate factor maps could be encoded on a 4 by 5.5-inch (10 by 14cm) microfiche format. Although factor map reductions of this magnitude are not practical, we will now discuss system trade-offs at the designer's disposal that may lead to smaller grating map formats for selected applications.

1. Focal Length Trade-Offs. Table 19 is of value in selecting the sampling aperture diameter when given a desirable level of factor map reduction and the map sample resolution. From the simulation data, we found that the $f^\#$ of the optical system (41) was a major factor in determining the S/N for Ronchi Grating Detection. The reason, of course, relates to the aperture diameter scaling of the Bessel function as shown in table 1. Thus, if we achieved acceptable S/N results for $D = 0.1$ mm and $f = 100.0$ mm, i.e. $f/D = 1000$, then we would expect equivalent S/N results for $D = 0.05$ mm and $f = 50.0$ mm. Although this is true, we must also keep in mind that given a grating of spatial frequency w_0 , a change in f will effect a change in the position of the grating harmonics on the detector, e.g.

$$f_1/f_2 = R_1/R_2 \quad (42)$$

where R_1 is the radius from the optical axis to the first harmonic of the grating function.

TABLE 19. Sampling Aperture Diameters Projected Onto Map and Ground Surface For Selected Map Reduction Ratios.

MAP SIZE: 22" x 29" (558.8 mm x 736.5 mm)
 MAP SCALE: 1:50,000

EQUIVALENT MAP SAMPLE DIA./GROUND SAMPLE DIA.

SAMPLING APERTURE DIAMETER

Map Reduction Ratio	Reduced Format	Commercial Format	0.01mm	0.025mm	0.05mm	0.075mm	0.10mm	0.25mm	0.50mm	0.75mm
-5x	111.5mm x 147.4mm	5" x 7"	$\frac{0.050 \text{ mm}}{0.01 \text{ mm}}$	$\frac{0.125 \text{ mm}}{0.025 \text{ mm}}$	$\frac{0.250 \text{ mm}}{0.05 \text{ mm}}$	$\frac{0.375 \text{ mm}}{0.075 \text{ mm}}$	$\frac{0.500 \text{ mm}}{0.10 \text{ mm}}$	$\frac{1.250 \text{ mm}}{0.25 \text{ mm}}$	$\frac{2.500 \text{ mm}}{0.50 \text{ mm}}$	$\frac{3.750 \text{ mm}}{0.75 \text{ mm}}$
-10x	55.7 x 73.7	7mm	$\frac{0.050 \text{ mm}}{0.01 \text{ mm}}$	$\frac{0.125 \text{ mm}}{0.025 \text{ mm}}$	$\frac{0.250 \text{ mm}}{0.05 \text{ mm}}$	$\frac{0.375 \text{ mm}}{0.075 \text{ mm}}$	$\frac{0.500 \text{ mm}}{0.10 \text{ mm}}$	$\frac{1.250 \text{ mm}}{0.25 \text{ mm}}$	$\frac{2.500 \text{ mm}}{0.50 \text{ mm}}$	$\frac{3.750 \text{ mm}}{0.75 \text{ mm}}$
-15x	37.3 x 49.2		$\frac{0.150 \text{ mm}}{0.01 \text{ mm}}$	$\frac{0.375 \text{ mm}}{0.025 \text{ mm}}$	$\frac{0.750 \text{ mm}}{0.05 \text{ mm}}$	$\frac{1.125 \text{ mm}}{0.075 \text{ mm}}$	$\frac{1.500 \text{ mm}}{0.10 \text{ mm}}$	$\frac{3.750 \text{ mm}}{0.25 \text{ mm}}$	$\frac{7.500 \text{ mm}}{0.50 \text{ mm}}$	$\frac{11.250 \text{ mm}}{0.75 \text{ mm}}$
-20x	27.9 x 36.9	35mm	$\frac{0.200 \text{ mm}}{0.01 \text{ mm}}$	$\frac{0.500 \text{ mm}}{0.025 \text{ mm}}$	$\frac{1.000 \text{ mm}}{0.05 \text{ mm}}$	$\frac{1.500 \text{ mm}}{0.075 \text{ mm}}$	$\frac{2.000 \text{ mm}}{0.10 \text{ mm}}$	$\frac{5.000 \text{ mm}}{0.25 \text{ mm}}$	$\frac{10.000 \text{ mm}}{0.50 \text{ mm}}$	$\frac{15.000 \text{ mm}}{0.75 \text{ mm}}$
-30x	14.6 x 19.5	15mm	$\frac{0.300 \text{ mm}}{0.01 \text{ mm}}$	$\frac{0.750 \text{ mm}}{0.025 \text{ mm}}$	$\frac{1.500 \text{ mm}}{0.05 \text{ mm}}$	$\frac{2.250 \text{ mm}}{0.075 \text{ mm}}$	$\frac{3.000 \text{ mm}}{0.10 \text{ mm}}$	$\frac{7.500 \text{ mm}}{0.25 \text{ mm}}$	$\frac{15.000 \text{ mm}}{0.50 \text{ mm}}$	$\frac{22.500 \text{ mm}}{0.75 \text{ mm}}$
-55x	8.6 x 11.3	Microfiche Image	$\frac{0.550 \text{ mm}}{0.01 \text{ mm}}$	$\frac{1.375 \text{ mm}}{0.025 \text{ mm}}$	$\frac{2.750 \text{ mm}}{0.05 \text{ mm}}$	$\frac{4.125 \text{ mm}}{0.075 \text{ mm}}$	$\frac{5.500 \text{ mm}}{0.10 \text{ mm}}$	$\frac{13.750 \text{ mm}}{0.25 \text{ mm}}$	$\frac{27.500 \text{ mm}}{0.50 \text{ mm}}$	$\frac{41.250 \text{ mm}}{0.75 \text{ mm}}$

Or if we fix the radius R_0 , such as a mid-ring radius of the detector, then a change in f must be reflected in a change in the spatial frequency, i.e.

$$f_1/f_2 = w_2/w_1 \quad (43)$$

Thus, if we reduce the focal length by a factor of 2.0, we must increase the grating spatial frequency by a factor of 2.0 to keep the first harmonic of the grating at radius R_0 . We will see in the next chapter that this trade-off is not generally applicable because it implies a capability for fabricating gratings at arbitrary spatial frequencies.

2. Laser Wavelength Trade-Offs. There is another trade-off available: we can change the wavelength λ of the laser light source within certain limits. As seen from (36) and (40), the wavelength of the laser light source is the scalar-relating focal length f , the grating spatial frequency w , and the radial distance from the optical axis R . Also, table 1 indicates that the size of the Bessel function for any $f^\#$ is directly related to the wavelength λ .

Table 20 lists some common gas lasers, their associated wavelengths, and a ratio value of the wavelength compared to the common HeNe wavelength. Using the expression for ratios of the Bessel function in table 1 and the laser wavelengths in table 20, we can compute equivalent sampling aperture diameters, as shown in table 21. Here the radius to the fourth Bessel zeros are given for detected values of f and D with $\lambda = 0.6328 \times 10^{-3}$ mm. The equivalent D_2 for other λ_2 , which yields the same Bessel radii, are given by

$$D_2 = D_1 (\lambda_2/\lambda_1) \quad (44)$$

and are shown to the right of table 21. Figure 44 graphs f/D versus radii from the optical axis for two selected Bessel zeros and two laser wavelengths. Changing from HeNe to HeCd lasers reduces the radius of the Bessel zeros by nearly a factor of 2.

Of equal importance, we can improve S/N by selecting a shorter wavelength. Modification of equation (41) to reflect this sensitivity to λ is given by

$$(\lambda_2/\lambda_1) f^\# = (\lambda_2/\lambda_1) (f/D) < 1000 \quad (45)$$

When the wavelength of the light source is changed, it should be remembered that the mid-ring spatial frequencies will change accordingly, as shown in Table 22

TABLE 20. Common Gas Lasers and Their Associated Wavelengths, λ .

<u>Gas Lasers (CW)</u>		<u>Ratio</u> <u>$\lambda_i/\lambda_{\text{HeNe}}$</u>
HeNe	, $\lambda = 0.6328 \times 10^{-3}$ mm	1.000
Ar	, $\lambda_1 = 0.5145 \times 10^{-3}$ mm	0.813
	, $\lambda_2 = 0.4880 \times 10^{-3}$ mm	0.771
HeCd	, $\lambda_1 = 0.4416 \times 10^{-3}$ mm	0.698
	, $\lambda_2 = 0.3250 \times 10^{-3}$ mm	0.514
<u>Gas Lasers (Pulsed)</u>		
Ne	, $\lambda = 0.5401 \times 10^{-3}$ mm	0.854
N ₂	, $\lambda = 0.3371 \times 10^{-3}$ mm	0.533

TABLE 21. Equivalent Sampling Aperture Diameters for Selected Laser Wavelengths.

$$D_s = D_0 / \lambda_0$$

Sampling Aperture Diameter ($\lambda_0 = 0.6328 \times 10^{-6}$)	RADIUS TO FOURTH BESSEL ZERO FOR TRANSFORM LENS FOCAL LENGTHS		EQUIVALENT SAMPLING APERTURE DIAMETERS (D_s) FOR SELECTED LASER WAVELENGTHS (λ_s)	
	$f = 100.0$	$f = 177.8$	0.488×10^{-6}	0.4416×10^{-6}
0.1	2.6837	4.7716	0.081	0.071
0.25	1.0735	-	0.203	0.174
0.5	0.5367	0.9543	0.386	0.349
1.0	-	0.4772	0.813	0.698

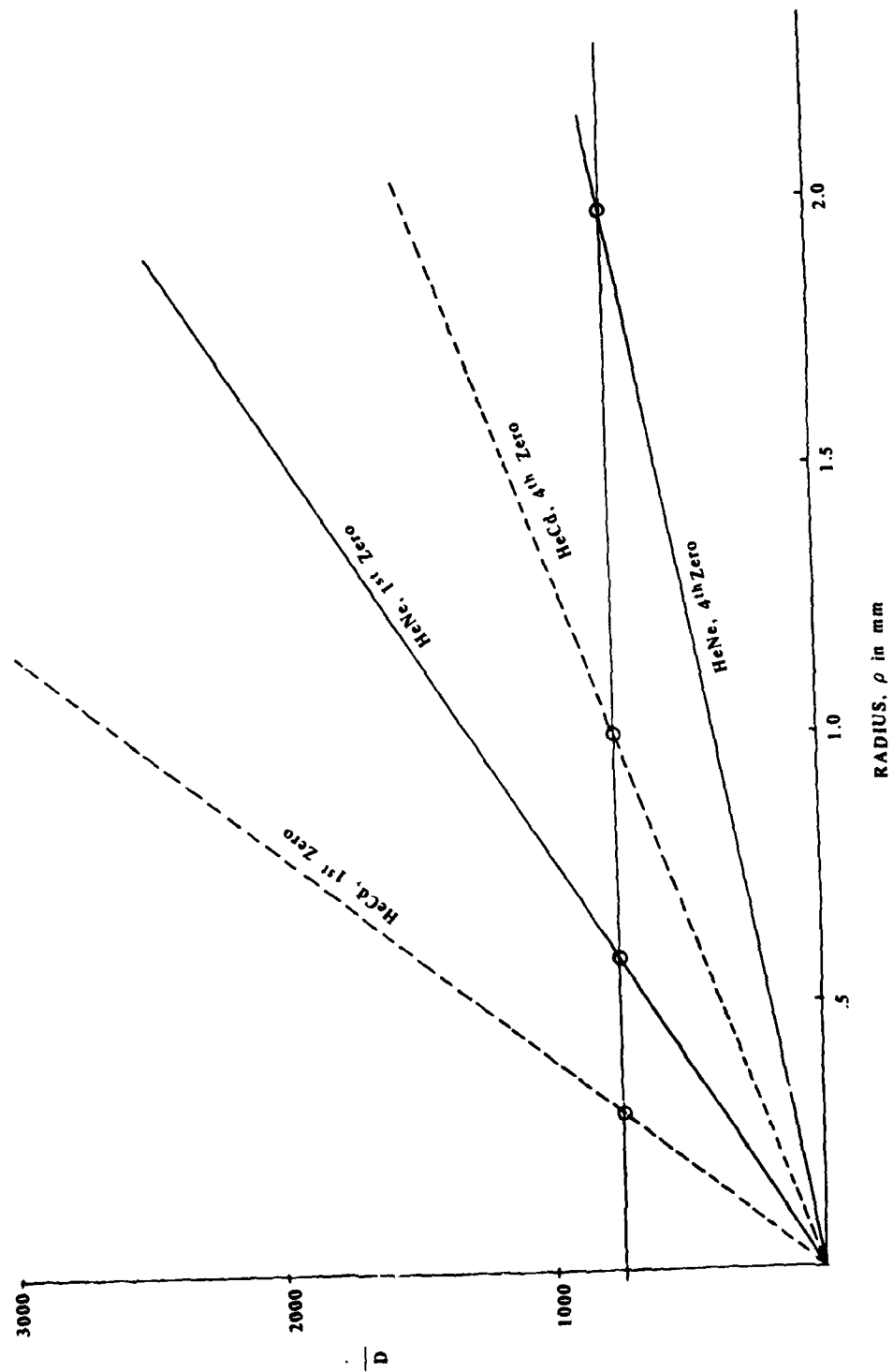


FIGURE 44. The f/D vs ρ (radius from optical axis) for Two Selected Bessel Zeros and Two Laser Wavelengths.

for the WRD-6420 detector. Also, the change in sensitivity of the ROSA detectors at shorter wavelengths must be considered, which will require higher laser power levels for equivalent output signals.

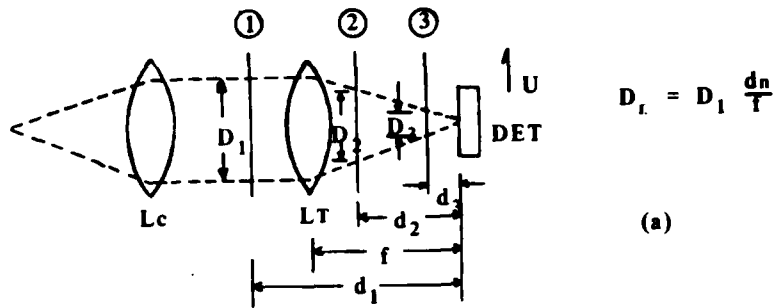
3. Trade-Offs For Position Of Input Transparency. Although the optical configuration shown in figure 4 is most commonly used in OPS systems, there is another configuration of potential value. In this configuration, the grating transparency normal to the optical axis is placed behind the transform lens, as shown in figure 45 (a), for the grating positions 2 and 3 instead of at the conventional position 1. Goodman⁵ discusses this configuration as involving diffraction of the converging cone of rays in the object plane that is detected and explained in the focal plane by Fresnel diffraction. An interesting aspect of this arrangement is that the aperture function transform, as indicated by figure 45 (b), remains the same, no matter where the transparency is placed between the transform lens and the detector and even though the diameter of the physical sampling aperture decreases by a ratio of d/f . This aspect is due to the constant $f^\#$ of the optical system. Moving the transparency behind the transform lens does however change the scale of the spectra in proportion to d/f . In figure 45 (c), the first two harmonics of a Ronchi grating spectrum are shown. Now consider this grating to be placed at one of the indicated positions in figure 45 (a). The physical location of the harmonics in the focal plane space is scaled according to

$$u = \frac{w}{\lambda f} \frac{d}{f} \quad (46)$$

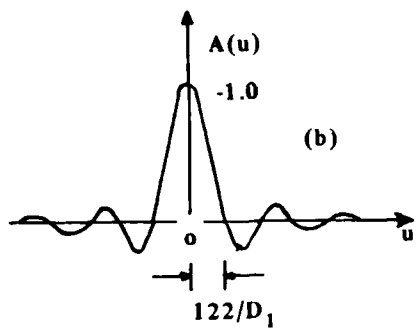
Thus in figure 45 (d, e, f), we see the size of the spectrum on the detector decreasing as the transparency is moved closer to the detector. Also, the amplitude in the converging cone of incident light will be more intense by $K' = K f/d$ as the physical sampling aperture becomes smaller. This is also indicated in figure 45 (d, e, f).

Trade-offs associated with this approach involve using smaller physical sampling apertures, with some flexibility of making adjustments or changing selections versus the complexity of maintaining multiple sets of decision criteria if the frequency plane scaling flexibility is exercised. Graphically it can be seen from figure 45 that S/N should decrease when figure 45 (b) is convolved with the spectra of figure 45 (e and f)

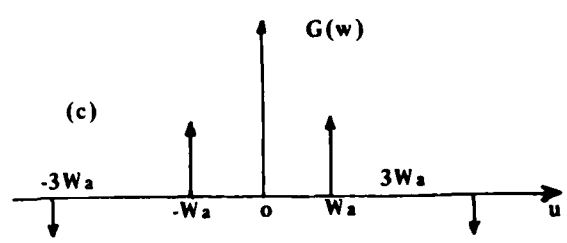
⁵J. W. Goodman, *Introduction To Fourier Optics*, McGraw-Hill Book Company, San Francisco, CA, 1968.



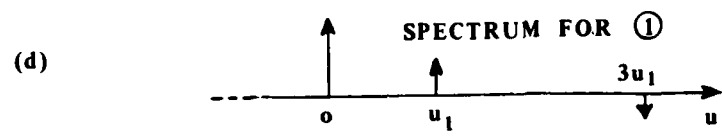
(a)



(b)



(c)

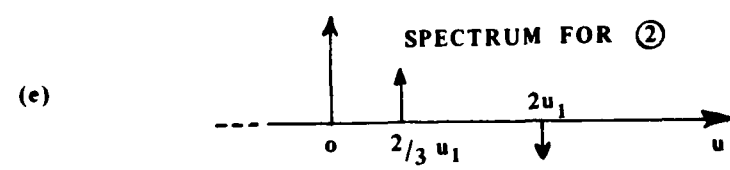


(d)

SPECTRUM FOR ①

SPACE SCALING:

$$u = \frac{W}{f\lambda} \left(\frac{d}{f} \right)$$

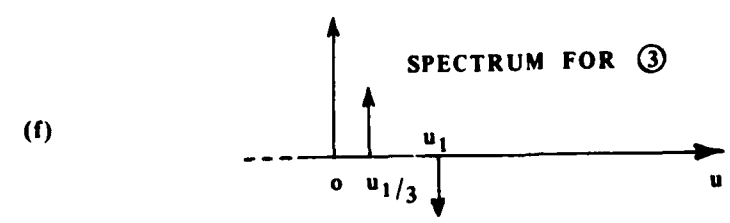


(e)

SPECTRUM FOR ②

AMPLITUDE SCALING:

$$K^1 = K \frac{f}{d}$$



(f)

SPECTRUM FOR ③

FIGURE 45. Gratings Placed Before and After Transform Lenses.

for the transparency positions 2 and 3, which should not be considered a generalization until further investigated. Another possible limitation of this approach involves aberrations in the detector plane introduced by placing the transparency in the converging beam of light. The major aberration will be spherical aberration, and it should increase in severity as d/f becomes smaller.

Additionally, the wavelength trade-offs discussed in the previous section can be coupled with those of this section to provide additional flexibility if desired.

VI. FABRICATION OF GRATING MAPS

In the previous chapter, the preliminary optical subsystem design and trade-off considerations for grating map systems were outlined. We saw that the system depended upon the grating map fabrication capability. In this chapter, we look at the technology for producing grating maps and complete the preliminary system design discussion. Then, approaches for extending capabilities to produce gratings with increased storage capacity will be outlined.

A. Fabrication Requirements. • For our purposes, a grating map is an optical transparency with factor map information encoded by Ronchi gratings at selected spatial frequencies and directions. Producing a grating map requires a capability to transform factor map codings into codings that can be used to produce the required gratings. For each class of data on the factor map, a unique Ronchi grating should be generated in terms of spatial frequency and direction. Figure 46 indicates conceptually how a grating map could be produced. Here the factor map at the upper left is transformed to a grating map at the lower right by a technique that essentially involves spatial masking with a separate grating for each factor map data class. In addition to the grating map, there must be an associated legend indicating the correspondence between the gratings and the factor map data classes. Also, a need exists for a capability to register automatically the transparency in the optical system, e.g. reference marks permitting automatic registration of the grating map in the optical system.

Although the grating map could be produced by cutting masks, it would be impractical because (1) it is labor intensive and (2) it would require a photographic reduction capability to achieve a micrographic image for mass storage.

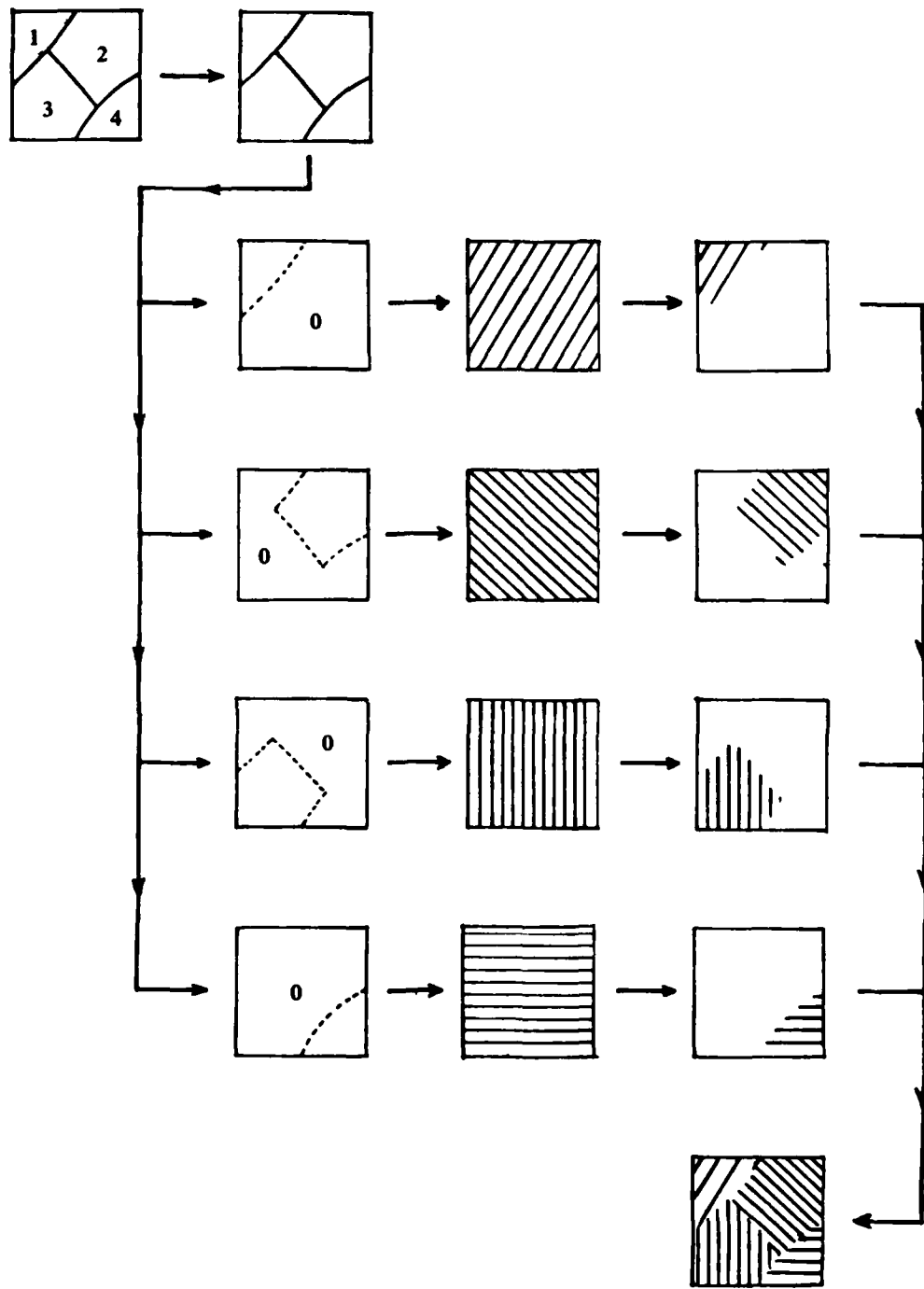


FIGURE 46. Generating the Grating Map.

A more practical approach would be to use a digital computer to program a modulated light scanning system that would write the gratings at the desired scale. We will assume the digital system can be programmed to accept factor map boundary data from a factor map and to generate a signal for driving the light modulator and scanner in synchronism. Two modes of scanning are available: vector scan and raster scan. The vector mode requires a random access capability, but provides faster, simpler and better performing grating recording capability; whereas, the raster mode is strictly sequential, but produces severe limitations on the signal processing and writing speeds.

Table 23 lists important parameters for grating map recorders. We will briefly review these parameters.

Printing Spot -- The size and shape of the printing spot on the recording medium will largely determine the resolution of the system. In general, the intensity profile of the printing spot will be Gaussian and not be a perfect square pulse. When the beam shape departs from an optimum, it is often necessary to provide a pixel overlap. The effective beam size and shape is mainly determined by the apertures in the system, which act as spatial filters.

Geometric Precision -- Geometric distortions of many types plague scanning printers. Deviations from orthogonality of the X and Y scanning axes cause distortions in the output image. The point-to-point accuracy of the scanner across the format determines the geometric precision of the scanner and should be on the order of 0.1 of the pixel size. Rescan error is important when two images are superimposed, and line start jitter can differentially displace scan lines in raster scan systems.

Radiometric Precision -- The minimum intensity of the scanning system determines the minimum density, or fog level, of the image. This parameter becomes particularly important where the rate of change of intensity to distance is large. For example, if a grating with a spatial frequency approaching that associated with the spot size is to be written in the raster mode where the scan direction is transverse to the grating, the rate of change of the intensity level will determine the grating modulation at that frequency. If the signal changes from 'full on' to 'full off' in one pixel distance, the digital-to-analog converters and the following electronics are "strained." The bandwidth of the system is defined by the rate of change of the signal rather than the pulse width. The radiometric errors should not exceed one-half of the least significant bit of the image data.

Writing Speed -- The throughput time or writing speed to produce an image from start to stop has been reduced significantly during the past several years, often at the expense of geometric and radiometric fidelity.

TABLE 23. Parameters For Grating Recorders.

Printing Spot

Size
Shape
Pixel overlap

Geometric Precision

Orthogonality of axes
Point-to-point accuracy
Rescan error
Line start jitter

Radiometric Precision

Minimum intensity
Rate of change of signal level
Radiometric error

Writing Speed

Operation and Maintenance

Operability
Maintainability
Reliability

Operation and Maintenance -- In addition to being reliable, systems must be simple to operate and maintain.

B. The State of Technology. • Table 24 contains a partial list of several technologies for producing Ronchi grating transparencies, including examples of available equipment. The completeness of the descriptive statements in terms of the parameters of table 23 illustrate the diversity and nonuniformity of the specifications with which manufacturers describe their equipment.

Although the equipment listed in table 24 was developed to generate hardcopy images from a computer, two listed systems appear to have the specifications necessary to make grating maps. The two systems are Electron Beam Recorder (EBR), produced by Image Graphics Inc., and the Cathode Ray Tube (CRT) system, produced by Information International Inc. Both systems have raster- and vector-scan modes. The high resolution EBR produces line widths from 3 to 90 μm (micrometers) by dithering a 3- μm printing spot around any of 32,768 x 32,768 addressable points, and the CRT system adjusts spot size from 3.6 to 19.6 μm for vector scanning. Both systems have recording speed, format size, and geometric fidelity advantages over the other systems.

Without available test data, a question arises of how precisely either system could produce a Ronchi grating for a selected spatial frequency within their operational range. For example, an ideal Ronchi grating will have sharp discontinuities in its optical density profiles; whereas, gratings produced by Gaussian-scanned printing spots will have smoother transitions, and the result will be a degraded Ronchi grating. The severity of degradation is dependent upon the beam profile. The effect of this degradation is to produce even and odd harmonics in the grating spectrum, which will decrease the S/N of the detected gratings. However, a limited testing program for generating gratings at a few selected spatial frequencies would resolve these questions.

C. Further Discussion of System Design Trade-Offs. • For this preliminary report, we assume that the above EBR and CRT systems will produce useful gratings. What then can we say about the optical system for detection of these gratings and how many data classes can we expect to encode and decode with these systems? Although it will be a continuation of the discussions of design trade-offs (see section 5B), this section will be concerned only with the EBR fabrication system.

TABLE 24. Examples of Grating Recording Systems.

ELECTRON BEAM RECORDER

- a. Image Graphics, Inc., Model Cartographic EBR, 3 μ m spot diameter, 32,768 x 32,768 addressable points, vector and raster plotting, vector mode line width selectable from 6 μ m to 250 μ m with standard electron gun or 3 μ m to 90 μ m with high resolution electron gun, 125,000 points/sec plotting rate in vector mode, raster scan rates variable up to 2 KHz, dynamic range 64 gray shades, optical density of 0 to 2.3, geometrical fidelity 0.03%, repeatability of sequential images 0.003%, 35 mm to 5.5 inch image formats, variety of films for recording. (Image Graphics Inc. produces twelve versions of the EBR with the major differences between units being the size of film and resolution.)

CATHODE RAY TUBE

- a. Dicomed, Model D-46 Digital Image Recorder, 2048 x 2048 spots on 70 mm format, raster plot only, 64 intensity levels.
- b. Dicomed, Model D-47 Color Digital Image Recorder, 2048 x 2048 pixels, 20 μ m spot diameter, 70 mm format, records on Ektrachrome Type 6115 film, 3 filters, exposure range 2.0 D, point spacing linearity 0.25%.
- c. Calcomp Inc, Model 1670 Graphic COM Recorder, random address and vector generation, spot size 10 μ m, number of addressable points 16,384 x 16,384, plotting area 79.4 mm x 79.4 mm, accuracy \pm 0.5%, 32 intensity levels, line generation rate 5 msec.
- d. Information International Inc., Model PFR-4, spot size programmable from 3.6 μ m to 19.6 μ m, 64,000 x 64,000 addressable points, 7.5 cm x 7.5 cm display, linearity 0.05%, 512 intensity levels, 0 to 3.15 density range, computer corrections for distortions, writing speed 400,000 points/sec.

TABLE 24. Continued.

DRUM PLOTTER

- a. Optronics, Model P-1500 Photowrite, sampling spots 12.5, 25, 50, 100, or 200 μm , density range 2.5D, 64 gray levels, light emitting diode light source, positional accuracy 2 μm , maximum data rate 60 KHz.

FLAT-BED PLOTTER

- a. Optronics, Model S-3200 Specwrite, Raster plotter, rasters 1, 5, 10, 25, 50, and 100 μm , density 0 to 2.5, 64 gray levels, positional accuracy 1 $\mu\text{m}/5$ cm, Maximum data rate 2.5 Kpoints/sec.
- b. Perkin-Elmer Corp., Model 1010, LED light source for black and white images has 2 to 500 μm spot size while color system uses CRT and filters with resolution of 5 to 50 lp/mm, 1024 gray levels, X and Y stage travel 25 cm, X and Y repeatability 1 μm .

113

LASER RECORDER

- a. Goodyear Aerospace Corp., Laser Recording System, 40 l/pmm, density dynamic range 0.2 to 2.4, 20 Mbit/sec data rate, geometric fidelity \pm 0.05%, sheet or roll film up to 9.5 inches.
- b. CBS, Model Laser Image Processing System, spot size 10, 20, or 40 μm , resolution 37.5, 19.8, or 9.4 lp/mm, film chip size 70 x 100 mm, 4096 x 4096 pixels, grey levels 256, 0 to 2.56 density, write time for 1024 x 1024 pixels is nine minutes.

LASER PHOTO FACSIMILE

- a. Harris Corp. Model Laser Photo, Resolution 256 samples/inch, dynamic range 0.1 to 1.75, data rates 1 minute/picture (8.5 x 11 inches).

The minimum spatial frequency grating generated by the EBR system with a line width of 90 μm is 5.5 Line-pairs per millimeter (LP/mm) and the maximum spatial frequency grating generated with a 3- μm -line width is 166.7 1/mm. From this information, we want to determine the best system for the parameters of sampling aperture diameter D, the focal length of the transform lens f, and the maximum number of detectable gratings corresponding to separate combinations of rings and wedges of the ROSA detector. To assist this discussion, table 25 presents an example worksheet in selecting the grating detection system parameter values. In addition to restricting this design to the EBR gratings, we assume that a WRD-6400 detector will be used and that a 0.10-mm sampling aperture is required to meet sampling criteria. However, the approach is general, and other criteria could be substituted.

In Trial 1 of table 25, the objective is to get an initial estimate for the parameter values by computing f from equation (36), w_{min} from equation (39), and D from equation (41). The result is a nonstandard value for f, and D was larger than specified. In Trial 2, a standardized value for f (6 inches) is given, the other values are computed, and a larger D value is obtained. In Trial 3, values for f and D are given and the value $f^\#$ is found to be larger than desired. Reducing f to 100.0 mm, while keeping D = 0.10 mm in Trial 4, results in w_{max} at detector Ring 32 being much greater than the high spatial frequency EBR capability, and w_{min} for Ring 7 has a spatial period that violates equation (39). Next, table 2 is used to find the detector ring having a spatial frequency equal to or less than the EBR high spatial frequency capability, and Trial 5 indicates this to be Ring 25. Likewise, the lowest ring satisfying equation (39) is found to be Ring 9 from table 2. This solution yields a total of 17 rings and 32 wedges for encoding 544 unique gratings. The decoding system would have a focal length of 100.0 mm, and the sampling aperture would be 0.10 mm, as per the specifications. The trials that follow explore possibilities of improving the capabilities by employing different laser wavelengths. As shown in table 25, Trial 9 achieves a similar number of rings and wedges, but would require a higher powered HeCd laser because of the lower WRD-6420 sensitivity at $\lambda = 0.3250 \times 10^{-3}$ mm. Thus, with all trade-offs considered, Trial 5 appears to offer the best set of preliminary design values. A similar approach could be used to investigate the applicability of the WRD-6400 detector or an equal ring width detector if the intended application could support a detector development effort. Likewise, this approach could be used to design and/or assist in the selection of other viable systems from those listed in table 24.

TABLE 25. Example Worksheet for Selection of Grating Detection System Parameter Values.

FOR: EBR GRATING WITH MAX. FREQ. = 166.7 λ_c /mm AND MIN. FREQ. = 5.5 λ_c /mm
 WRD-6420 DETECTOR WITH R_{max} = 15.49 mm and R_{min} = 1.01 mm,
 λ_c = 0.6328 x 10⁻³ mm UNLESS OTHERWISE STATED IN COMMENTS.

TRIAL	f (mm)	W_{max} (λ_c /mm)	W_{min} (λ_c /mm)	D (mm)	f/D	COMMENTS
1	146.86(36)	166.7(G)	17.02(E39)	0.146(E41)	1000(G)	NONSTD. f, D LARGER THAN DESIRED
2	152.4(G)	160.6(E36)	10.52(E40)	0.238(E39)	636(E41)	D LARGER THAN DESIRED
3	152.4(G)	160.6(36)		0.100(G)	1524(E41)	f# LARGER THAN DESIRED
4	100.0(G)	244.8(E36)	20.31(E40)	"	1000(E41)	(E39) VIOLATED
5	"	159.88 (T2,R ₁₅)	30.01 (T2,R ₉)	"	"	ACCEPTABLE, 17 RINGS & 32 WEDGES
6	"	158.33 (T22,R ₁₅)	24.98 (T22,R ₇)	"	813(E45)	λ_c = 0.5145 x 10 ⁻³ mm, ACCEPTABLE 15 RINGS & 32 WEDGES
7	177.8(G)	160.24 (T22,R ₁₅)	24.52 (T22,R ₁₀)	"	1445(E45)	λ_c = 0.5145 x 10 ⁻³ mm, SUBOPTIMUM f 22 RINGS & 32 WEDGES
8	"	159.59 (T22,R ₁₀)	25.82 (T22,R ₁₀)	"	1371(E45)	λ_c = 0.4880 x 10 ⁻³ mm, SUBOPTIMUM f 21 RINGS & 32 WEDGES
9	"	163.31	27.34	"	931(E45)	λ_c = 0.3250 x 10 ⁻³ mm, ACCEPTABLE 17 RINGS & 32 WEDGES
10	152.4(G)	λ_c = 11.221(E36) [λ_c = 10.821](T2)	λ_c = 2.411(E40) [λ_c = 2.621](T2)	"	1063(E45)	λ_c = 0.4416 x 10 ⁻³ mm, ACCEPTABLE 16 RINGS & 32 WEDGES

KEY: (G) - GIVEN; (E36) - EQUATION 36 FROM TEXT; (T2,R₁₅) - TABLE 2, RING 25 FROM TEXT
 λ_c = 11.221] = COMPUTED RADIAL DISTANCE, [λ_c = 10.82] - TABULAR RADIAL DISTANCE FOR RING-26.

D. Extending The Storage Capacity of Grating Maps. • The discussion of grating fabrication and the information storage capacity of a grating map would not be complete without advancing some concepts that improve the storage capacity if required. In the preceding section, we developed an example design showing that the EBR system may have the potential to encode Ronchi gratings at 17 spatial frequencies and 32 directions for a total of 544 thematic data classes for sampling with a 0.10 mm aperture. For certain classes of data, this number of data classes is more than sufficient, but suppose the need existed for producing grating maps with a larger set of data classes. This need might arise if contour maps are to be encoded for geographic areas having severe relief display problems. Another need for a large number of data classes might arise from a requirement to combine factor maps so as to keep the total number of graphics to a minimum. Nevertheless, these added capabilities will not be gained without paying some price. We will look at a few concepts for increasing capabilities and the price to be paid for the increase.

1. Amplitude Coding. All discussions have been concerned with binary Ronchi gratings in the form of optical transparencies, i.e. square wave gratings with maximum and minimum transmission values only. Table 24 indicates that the EBR can produce a modulated recording having 64 shades of grey over an optical density range of 0 to 2.3. Theoretically, this method should provide an encoding capability for 17 spatial frequencies, 32 directions, and 64 amplitudes equal to $17 \times 32 \times 64 = 34,816$ separate data classes. In reality, little margin is left for noise associated with system variability. Also, at low grating amplitudes, very low level OPS signal detection problems will be experienced. Thus, it is reasonable to select a subset of the 64 grey levels, say 10 levels, which produce high S/N results similar to that associated with the binary gratings. Just 10 amplitude levels may provide an encoding capability for 3,481 data classes with the EBR. With only two levels, the storage capability of the binary gratings will be doubled.

To obtain additional storage capacity in this manner will require a grating preparation capability that assures the desired uniformity. Also, the quality of the signal processing system must be such that the various signal levels can be unambiguously discriminated. For example, the laser light source must have a high degree of stability over short and long time periods. Thus, a simple laser for binary grating fabrication capability must be replaced by a stabilized laser when the multi-level gratings are employed. Similarly, the electronics must have temporal stability and perhaps more precision. The software for decoding the multi-level grating detection data increases in complexity and time required per decision as the number of grating amplitude levels increases.

2. Multiple Gratings. Combinations of superimposed gratings, each of which is aligned so that their separate spectrums will not fall on the same detector wedge, provide another means for increasing storage capacity, however, this approach is not as simple or powerful as the amplitude codings. An analytic explanation of this approach will not be advanced here, but one can easily conceptualize that in addition to the separate spectra of the individual gratings, there will be interaction spectra that tend to cloud the S/N mental picture. This approach could cause additional complexity in decision-making software to determine whether superimposed gratings or separate contiguous gratings existed in the sampling aperture.

3. Color Gratings. Amplitude coding and multiple grating codes can be used with gratings prepared on color transparencies. Separate lasers or narrow band filtered light will be required to decode the color transparency data. Table 20 indicates a range of blue through red optical wavelengths available in common gas lasers. Although it would appear to be promising, this approach must be tested.

VII. SYSTEMS CONCEPTS

The previous two chapters indicated optical subsystem design and trade-off considerations for grating map systems, outlined the technology associated with grating map fabrication. In this chapter, we outline more general optical subsystem concepts and integrate these with the other subsystems, i.e. the electronic, the digital, and the storage and retrieval subsystems, to present a more unified view of the major system features. An example system is then described in some detail to illustrate subsystem interrelations.

A. Basic Subsystems. • Important components of the optical, electronic, digital and storage and retrieval subsystems will be reviewed.

1. Optical subsystem. The major components of a standard OPS optical subsystem are as indicated in figure 4, and the preceding two chapters addressed their design considerations for OPS detection of grating maps. The basic optical configuration is duplicated in figure 47(a), where, along with figure 47(b and c), the different configurations for placing a transparency in a stationary light beam are indicated. The arrangement shown in figure 47(b) (which was given before in V, B, 3) and the single lens arrangement shown in figure 47(c) represents a further development that is simpler in concept, but will, in general, produce greater aberrations because of the severe requirements satisfied only by expensive lens systems. One- or two-dimensional sampling is

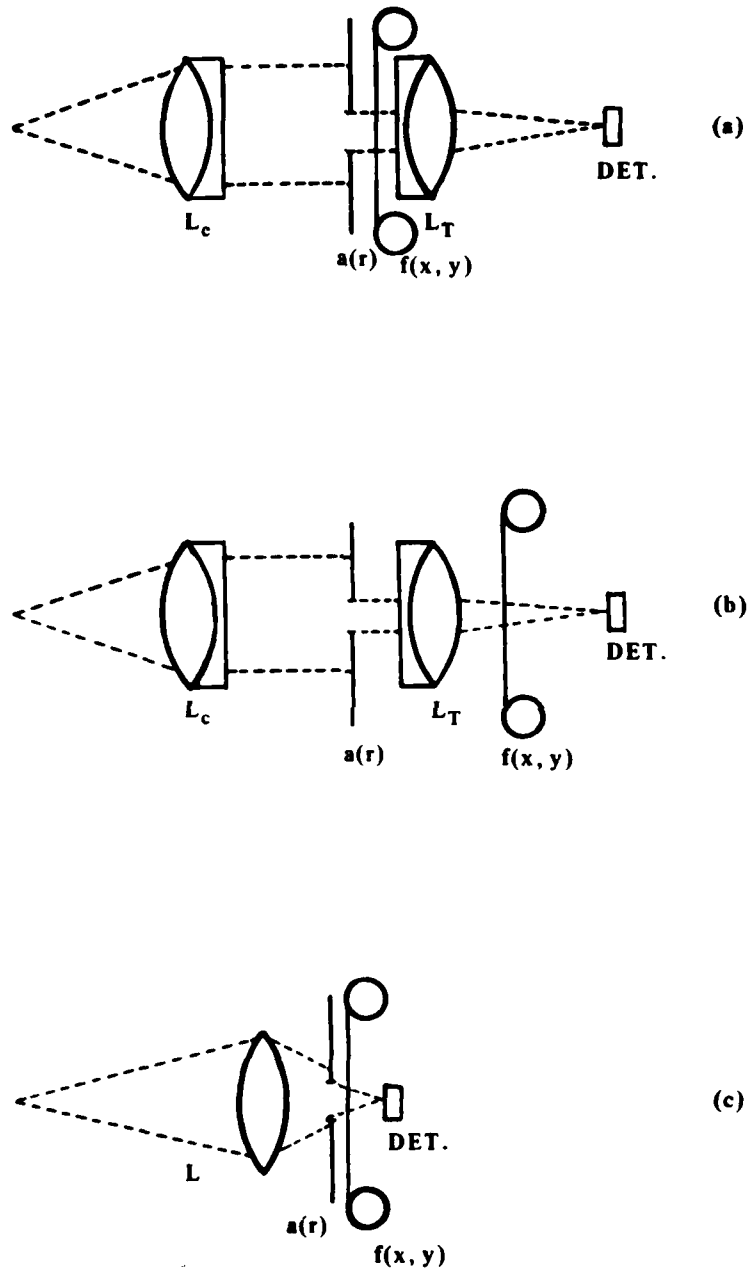


FIGURE 47. Optical Arrangements for Stationary Light Beam OPS Systems.

accomplished with these optical configurations by translating the sampling aperture $a(r)$, or more preferably by translating the transparency, while the sampling aperture remains fixed and centered on the optical axis.

In general, stationary light beam OPS systems, which translate the transparency to obtain sample data over an area, provide excellent research systems, but as with the automated microdensitometers, these arrangements are usually too slow for operational applications. Faster OPS sampling systems can be realized by moving a telecentric sampling beam, i.e. a collimated beam parallel to the optical axis, over a stationary transparency. Two approaches will be outlined. The first approach, shown in figure 48(a and b) for one- and two-dimensional arrangements respectively, uses glass lenses and galvanometers to move and form a telecentric scanner, with samples in plane 1 and 2. Here we will briefly review the two-dimensional arrangement of figure 48(b). The beam-forming optics (BFO) are primarily responsible for producing a clean, collimated beam of a given diameter. This beam is focused at the center of rotation of a galvanometer mirror M_{s1} and this spot is relayed by the relay optics (RO) to the center of rotation of a second galvanometer mirror M_{s2} , which scans orthogonal to that of the first. Generally, the galvanometers are moved under computer control so that the sampling beam raster discretely scans the transparency, and a matrix of sample points are obtained; however, random access scanning can also be applied. These systems have their limitations in that galvanometer retrace time is significant, and the galvanometer resolution and accuracy must be exceptional to obtain an orthogonal N by N sample matrix with a high number of points and with a high reproducibility. Additionally if the input transparency is large, then the lenses must also be large and expensive.

The second approach for OPS sampling with scanning telecentric beams is illustrated in figure 49. Here, reflecting optics in the form of parabolic mirrors reflect the beams similar to the manner that lenses refract light. The arrangements in figure 49 are analogous to the three configurations using lenses in figure 47, and also to those in figure 48. In figure 49, the first parabolic mirror M_1 focuses the collimated and sized beam onto a rotation multi-faceted mirror that reflects the beam to the first mirror, where it is collimated, diffracted by the transparency, as in (a). Parabolic mirror M_2 then acts as a transforming element to form the diffraction pattern of the sampled transparency on the detector surface. The rotating mirror is usually driven by a stepping motor having a high number of resolvable steps per rotation T , which enables this approach to have the advantage in that it has no retrace time. Tilted facets on the rotating wheel provide the scanner with a two-dimensional raster capability, limited of course by the number of facets. Thus, this approach usually provides a better one-dimensional scanner with a motorized film drive mechanism giving the second and slower scan motion.

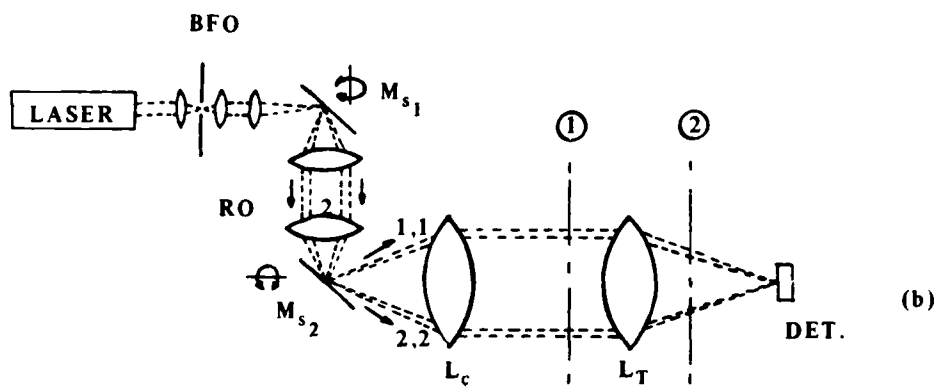
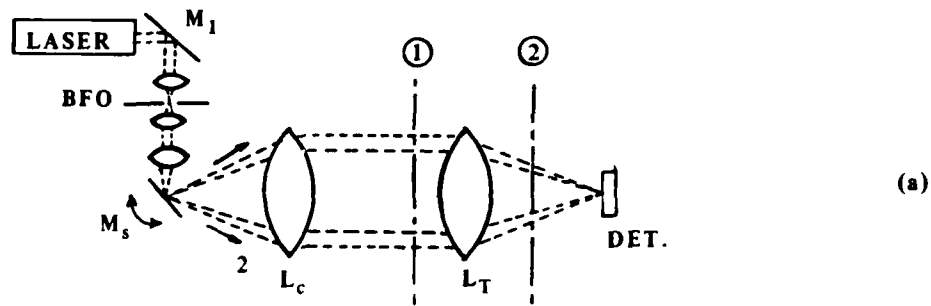


FIGURE 48. One- and Two-Dimensional Telecentric Beam-Scanning Arrangements Using Laser.

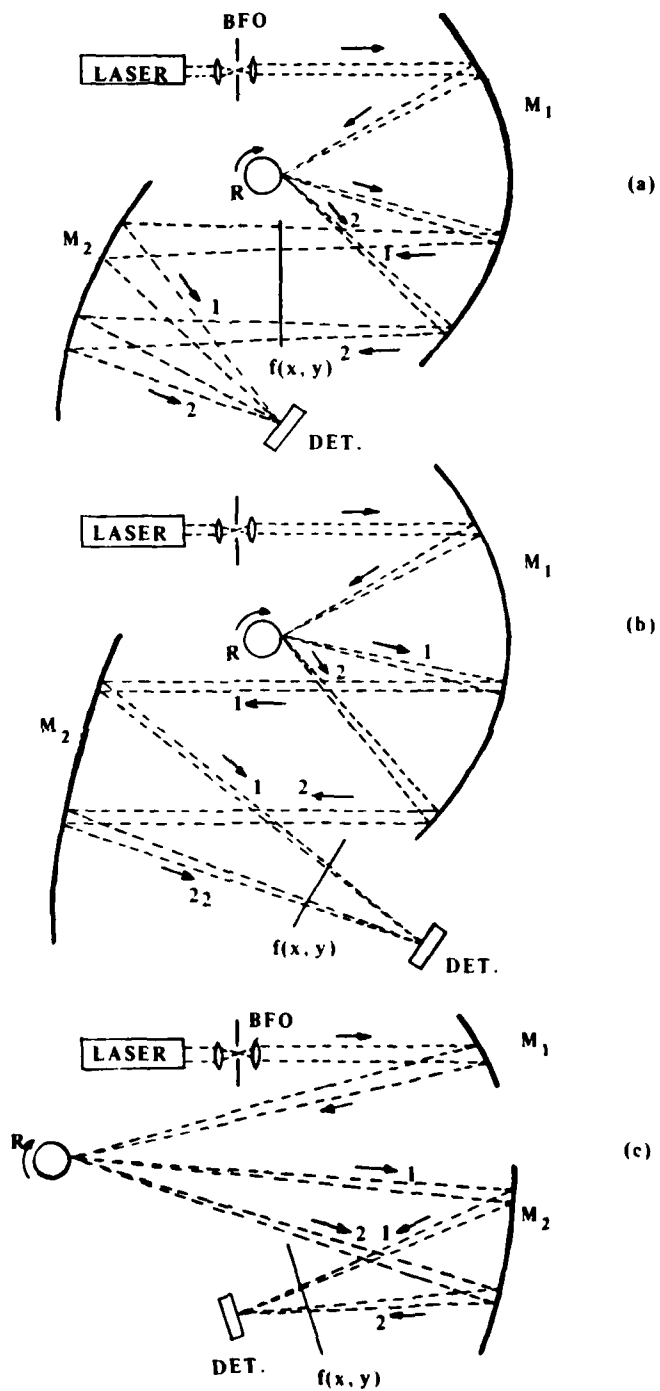


FIGURE 49. Optical Arrangements Using Parabolic Mirrors. Analogous to Figure 47 for Scanning Telecentric Beam.

2. Electronic Subsystem. For our purposes, we separate the electrical signal processing into electronic and digital subsystems arbitrarily, based upon whether the signal is analog or digital, respectively. Components of the electronic subsystem relate principally to the interface between the optical and digital subsystems. Analytical characterization of the ROSA optical and electronic processing is shown in figure 5. Here the detector changes the spatial light distribution in the spatial frequency plane to an ordered set of electrical signals, one signal for each detector ring and wedge. These signals must then be amplified in a manner that preserves the nature of the signal. The signals can be sequentially amplified, or each signal can be amplified in parallel and then multiplexed as shown in figure 5. This is followed by an analog to digital (A/D) converter that quantizes the analog detector element signals into an ordered string of binary signals that are formatted for the digital computer system.

Interfacing an OPS detector with a digital computer system is not trivial because the signal has a potential dynamic range of 10^6 between the high level signal near d.c. and that in the high spatial frequency areas, which is near or within the noise level of the detector. The ROSA electronic system uses an autoranging second stage amplification that divides the signal into decades as described in Section 3.1 and more specifically in equation (10).

3. Digital Subsystem. The major component of the digital system is the digital computer. The computer serves as the heart and mind of the system in the sense that it directs and controls all operations within the system and makes classification decisions, which are reflected in the data or information that are output from the system. The subsystem does only what it is programmed or hardwired to do; however, today's systems are sophisticated relative to digital machines of the not too distant past and they have significant capabilities. The digital subsystems can operate with today's minicomputers. Designs have flexibility and may choose to delegate selected processing, control, and decision-making responsibilities to lower-order microprocessors for one or more reasons.

Other components of the digital subsystem are the input/output devices used to communicate and interact with human operators.

4. Grating Map Storage and Retrieval Subsystem. A subsystem concerned with the storage and retrieval of the minified grating maps must provide not only a physical storage and retrieval capability but also an index of locations where grating maps are stored and must be returned to after use. This indexing function can be served by data base subsystems that are integral to the digital subsystem.

Automated and semi-automated components for physical storage and retrieval of large numbers of microfiche and smaller format transparencies are commercially available.

B. Example System Concepts. • The above discussion of basic subsystems will be supplemented with additional concepts for optical systems. This will be followed by a discussion of a simple system using minified grating maps, which will integrate subsystem concepts and show how the system is controlled and coordinated.

1. Additional Optical Subsystem Concepts. Previous discussions have emphasized the potential for an OPS detector in grating detection. Within automated systems context, it would often be convenient to be able to "see" the apertured portion of the input transparency sampled by the OPS detector, e.g. to aid in resolving boundaries between contiguous gratings within an OPS sampling aperture, to assist in registering the image and stage coordinates prior to sampling, or to help identify point and line data. An $n \times n$ photodiode array detector can be added to the OPS optical subsystems in figure 47(a) and figure 48(a and b) as shown in figure 50. The stationary beam optical subsystem in figure 50(a) is rather simple to implement, and the focal length of the inverse transform lens is chosen so that the sampled image fills the $n \times n$ photodiode array detector. In figure 50(b), a one-dimensional telecentric scanner may have a galvanometer scanner to direct properly the reconstructed image to the image detector, and in figure 50(c) the two-dimensional telecentric scanner requires two galvanometers. The corresponding galvanometer from figure 50(b and c) can be slaved to those of figure 48(a and b), respectively, to effect a simple coordinated scan.

Figure 51 indicates how multiple factor maps of the same geographic area may be sampled in a coordinated fashion. This is a simple extension of the system shown in figure 47(a).

Two example illustrations of how a spatial light modulator (SLM) may be used in an OPS system are shown in figures 52 and 53. Several types of SLM are currently under study at a number of laboratories for applications in coherent optical image processing systems. Casasent⁶ presents a review of the technology. For the applications in these illustrations, an SLM such as the Itek Corporation Pockel's Readout Optical Modulator (PROM) device with record, read, and erase capabilities and properties of high dynamic range and analog image manipulation with bias adjustments can be used.

⁶D. Casasent, "Spatial Light Modulators," Proc. IEEE, Vol. 65, No. 1, Jan 1977, pp. 143-157.

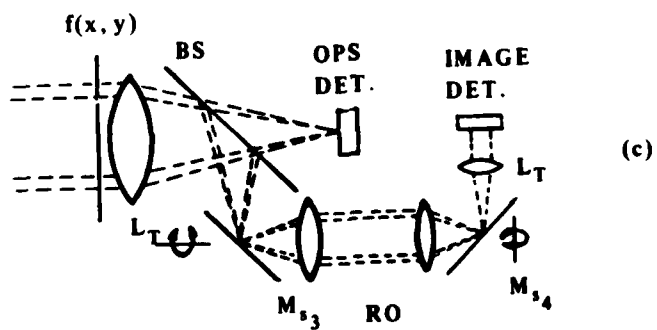
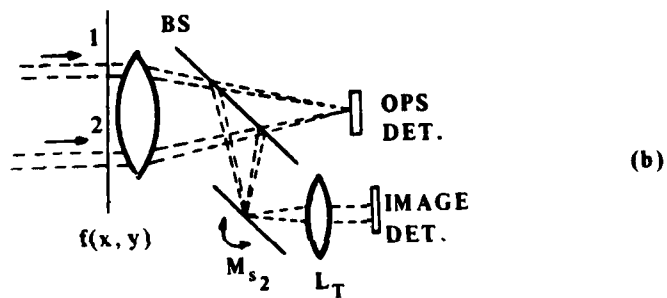
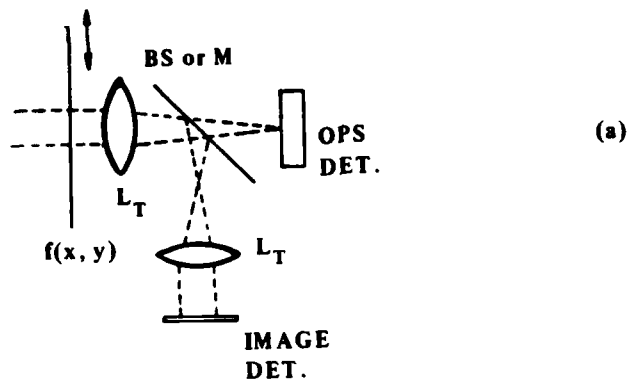
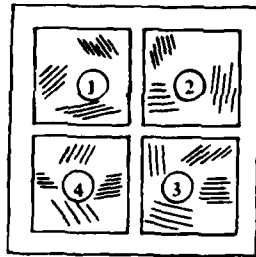


FIGURE 50. Addition of a Photodiode Array Detector to Enable "Seeing" of the Image Sampled by the OPS Detector.

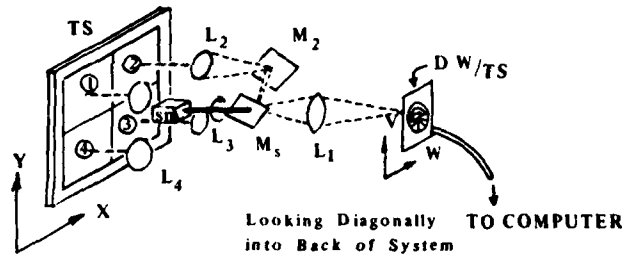
FACTOR MAP GRATINGS:



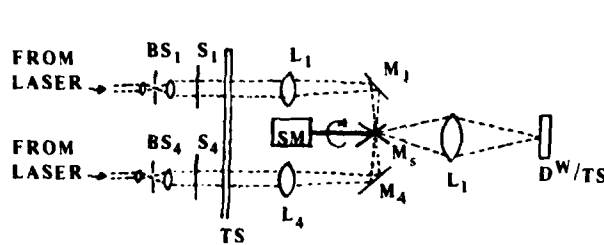
DIFFERENT FACTOR MAP GRATINGS:

① ② ③ and ④

TRANSLATION STAGE, TS



MIRRORS M_1 , M_3 , and M_4
NOT SHOWN



$i = 1, 2, 3, 4$

- BS_i - Beam Shaping Optics
- S_i - Shutters
- TS - Translation Stage
- L_i - Transform Lens
- M_i - Mirror
- SM - Stepping Motor
- M_s - Spinning Mirror
- L₁ - Imaging Lens
- D - OPS DETECTOR

SIDE VIEW SCHEMATIC IN X-DIRECTION

OPERATIONAL SEQUENCE:

Grating to be sampled is selected by Computer (example, 1), then Shutter S_1 is opened and S_2 , S_3 , and S_4 are closed. Simultaneously, the stepping motor rotates Mirror M_s into position so that lens L_1 can image the OPS from 1 onto the Detector, D. Detector D is mounted on a translation stage that is servo driven to center target Detector on the optical axis and thus compensate for alignment errors in positioning the rotating Mirror, M_s .

The registered gratings are mounted on a translation stage which moves orthogonally so as to allow four sample beams to illuminate the same grating coordinates.

FIGURE 51. Concepts for Multiple-Coordinated Factor Map Gratings.

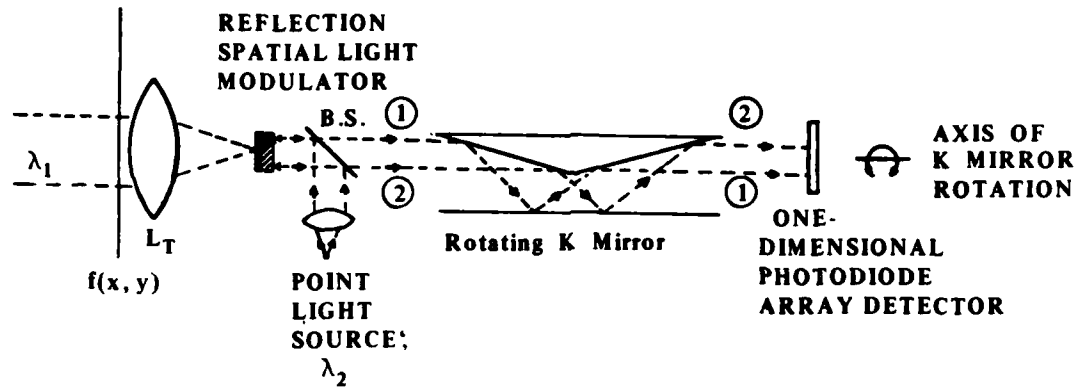


FIGURE 52. Example of an OPS Configuration Using a Spatial Light Modulator, a Rotating K Mirror, and a One-Dimensional Photodiode Array Detector.

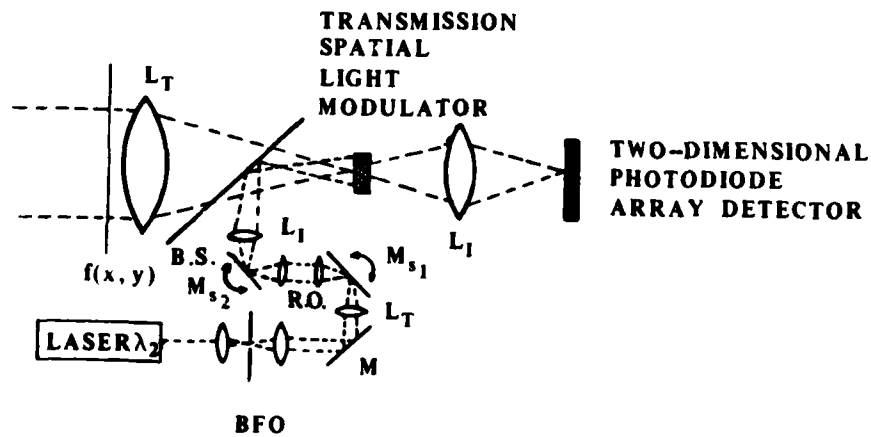


FIGURE 53. Example of an OPS Configuration Using a Spatial Light Modulator, a Two-Dimensional Scanner and a Two-Dimensional Photodiode Array Detector.

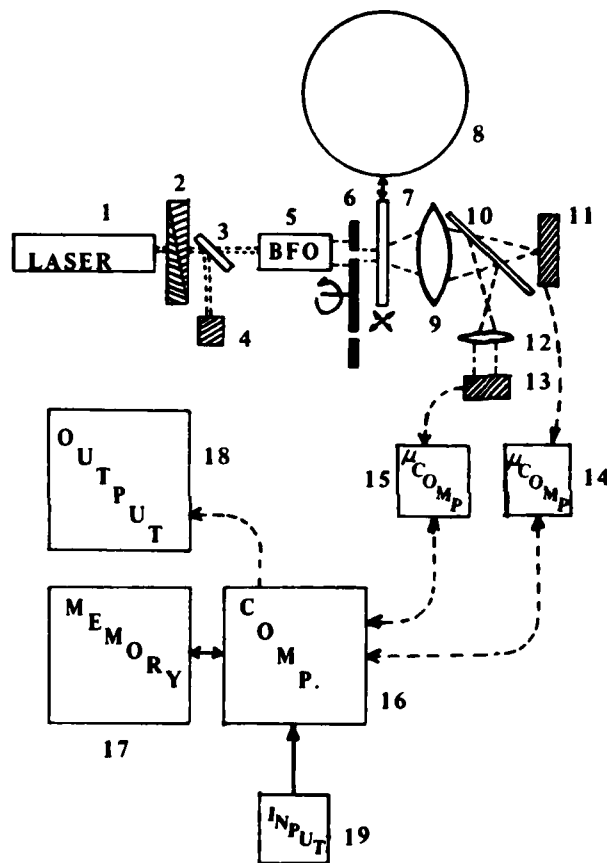
The example shown in figure 52 has an SLM that records the spectrum of the sampled portion of the transparency. The SLM is a reflection device with a dichroic filter on its face and is nearest to the transform lens. This filter passes the OPS record light of wavelength λ_1 , while serving as a reflector for the collimated readout light λ_2 . The light is doubly modulated image-wise by the OPS record during its two passes through the SLM crystal. A rotating K mirror serves to rotate the spectrum on a one-dimensional detector. Decision criteria associated with this system would determine the spatial radius and direction of the first harmonic of the grating being sampled. The K mirror rotates so as to keep the optical axis stationary, with the image rotating at twice the angular velocity as the prism.

For the example shown in figure 53, the OPS pattern is recorded in the SLM. By changing the electrical bias on the device, the positive pattern is changed to a negative pattern and thresholded. A scanning spot traces a high-resolution, two-dimensional raster over the SLM and light is transmitted through the device only above the negative threshold so that detection and identification of the grating direction and spatial frequency is rather simple with a two-dimensional photodiode array detector. In this illustration, a transmission SLM is shown, but a reflection SLM could be used by moving all components associated with the scanner to the opposite side of the SLM as in figure 52.

2. A Simple System Example. A simple automated system for machine readable factor maps is shown in figure 54. The purpose of this discussion is to indicate the coordination of the previously discussed components of an automated OPSA system and to present some additional concepts not developed earlier. We will first briefly review the system components and how they are coordinated, then we will present a scenario related to the possible use of such a system.

Most components of the optical subsystem in figure 54 have been discussed previously except for the variable optical density wedge (2) and laser intensity level detector (4), which may serve in combination to monitor and control the laser output by feedback through the computer. The rotatable disc with sampling apertures (6) also operates under computer control, as does the two-dimensional translation stage (7). The grating map storage and retrieval subsystem (8) is similar to a carousel that contains grating map transparencies with more than one grating map per transparency. This subsystem also has capability for loading and unloading the translation stage with transparencies under computer control.

Electronic subsystem components, except the detectors, have not been shown in figure 54 so as to keep the illustration simple and uncluttered. The two de-



SYSTEM COMPONENTS

1. LASER
2. Variable Optical Density Wedge
3. Beam Splitter
4. LASER Intensity Level Detector
5. Beam Forming Optics
6. Rotatable Disc with Sampling Apertures
7. Grating Map Transparency on Two-Dimensional Translation Stage
8. Grating Map Storage and Retrieval System
9. Transform Lens
10. Beam Splitter
11. OPS Detector
12. Inverse Transform Lens
13. Photodiode Array Detector
14. Micro-Computer for 11
15. Micro-Computer for 13
16. Mini-Computer
17. Memory Devices
18. Output Devices
19. Input Terminal

FIGURE 54. A Simple Automated OPSA System for Reading Optically Stored MGI Factor Maps.

tectors, similar to those in figure 50(a), are used for sampling the optical power spectrum with a ROSA detector (11) and a two-dimensional photodiode array detector (13) for sampling the input image.

A microcomputer (14 and 15) can be interfaced directly to each detector to improve system efficiency by removing processing, control, and decision tasks from the central computer. These microcomputers can be micro programmed to accomplish the data acquisition and formatting temporary storage in local buffers, the low level data processing and decision-making, and the data transfer directly to memory via a DMA (direct memory access). The microcomputers are controlled by a central minicomputer (16) that serves to coordinate and control subsystem operations and to process data for internal use or to satisfy requirements placed in the system. The central computer controls the laser output level by periodically sampling the laser intensity level detector (4) signal after A/D electronic conversion (A/D converter not shown). The central computer then translates the variable optical density wedge via a solenoid or stepping motor to effect the desired light level input for the system. It also controls the movement of the two-dimensional translation stage (7), the rotatable disc with sampling apertures (6), and the grating map transparency storage and retrieval system (8). The central computer accepts a problem statement for a geographic area (19) and selects appropriate factor map transparencies with the aid of a data base management system and other collateral data in memory. The selected solution approach will dictate the geographic areas to be scanned, the sample spacing, and the sampling aperture diameter. The central computer then controls movement of the two-dimensional translation stages (7), the rotatable disc with sampling apertures (6), and the grating map transparency storage and retrieval system.

The spatial image detector is used to register the transparency in the stage coordinate system. The grating legend, stored in memory for the sampled transparency, provides information to decide grating spatial frequency and direction to obtain data classifications. These decisions are processed in MGI application programs and the results are output in readable form (18).

A short scenario of the manner in which the system of figure 54 may be used in a MGI application problem follows. The problem statement is presented to the system by an operator through the input station (19) by problem type with selected parameters defined, e.g. for a cross-country mobility problem, the parameters may be initial geographic location, final destination, type of vehicle, number of vehicles, etc. Application software then selects types of data desired and checks the data base to determine if these data types are available for the problem area.

Suppose this concerned MGI Terrain Factor Maps stored as Ronchi grating maps on transparencies is an automated storage and retrieval system as in figure 54. The computer system then controls retrieval of a selected factor map (transparency) from the storage carousel and inserts it into a holder on the two-dimensional translation stages. A short automated registration procedure is accomplished with the aid of the photo diode array detector to align the transparency coordinate system with the translation stage coordinate system. Now the stage coordinates can be computed to obtain the desired transparency sampling. Each time the stages are incremented to a new sampling location, the ROSA detector's microcomputer is directed to obtain a set of detector element samples. While the stage is translating to the next sample location, the sampled data can be decoded and only the factor map class symbol is stored temporarily in a buffer within the microcomputer. These processed data are then block transmitted to central memory via direct memory access when the buffer is full or the sampling completed. Other factor map data for the same area, e.g. soils, slopes, vegetation, etc., can be processed in like manner. The central computer can then use these spatial data, along with temporal data, e.g. local weather history and projected weather, to compute or decide on the cross-country mobility data class for each sample location. Processed data can then be formatted and output on a monitor and/or plotter for inspection and/or distribution.

A somewhat similar program to the system in figure 54 is flow charted in figure 55. This simple example relates to only one of many possible ways in which an automated grating map storage and retrieval capability may be employed as a machine-readable MGI factor map mass store system. These concepts must now be tested and verified for correctness as well as completeness. The potentials at this preliminary stage are quite promising.

VIII. SUMMARY

This report analyzed optical power spectral (OPS) approaches to machine-readable factor maps for use in terrain information systems. The objective was to offer a more compact, simpler, and cheaper factor map data base storage and retrieval systems than would be available by all digital technology. The basic concept of the system involves use of OPSA for decoding data from reduced factor maps that have been encoded by spatial frequency and direction of Ronchi optical gratings.

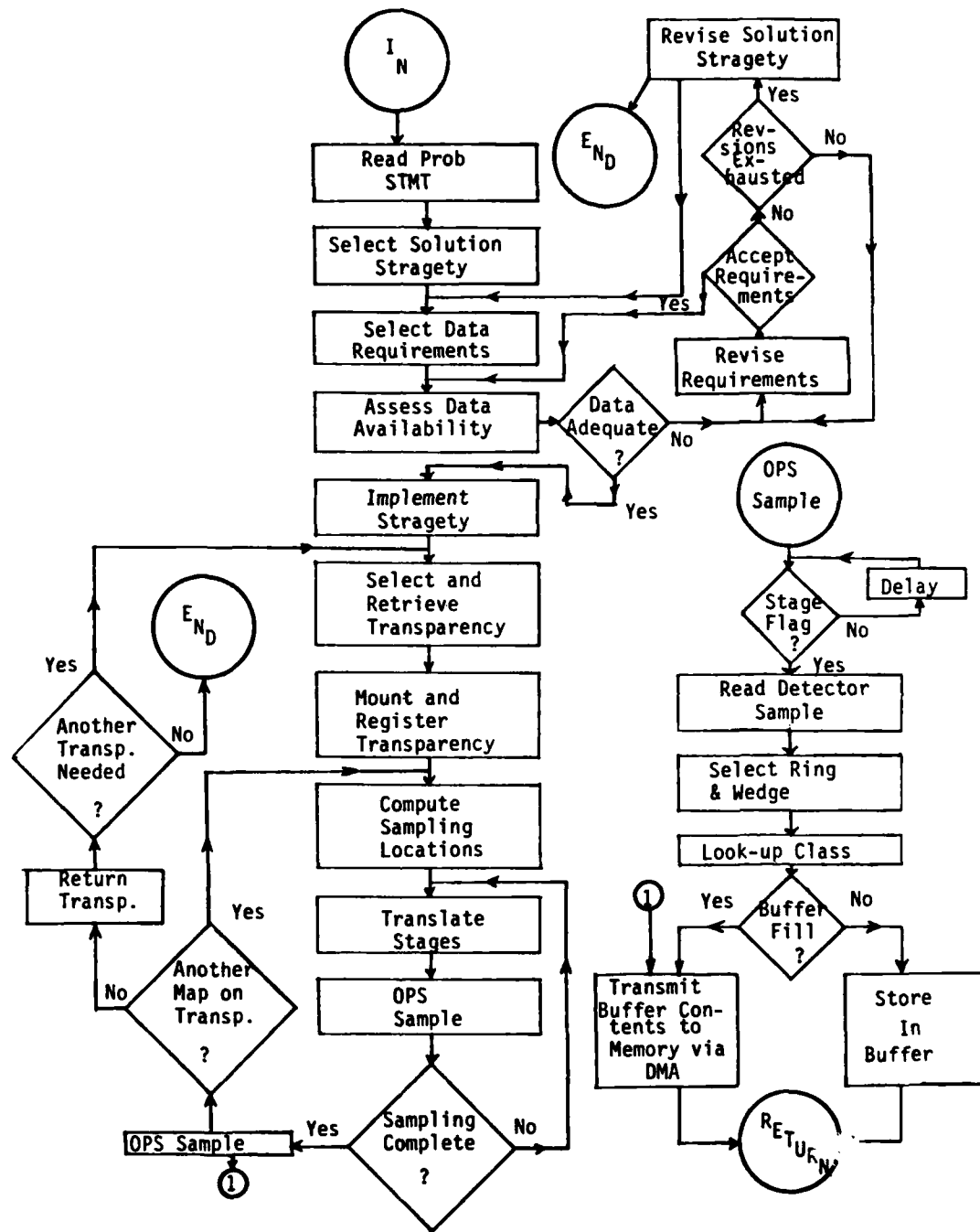


FIGURE 55. Program Associated With Automated OPSS System in Figure 54.

An OPSA system consists of a coherent optical sampling subsystem, an electronic detection and signal processing system, and a digital computer with associated software for control and decision-making. In Chapter III, an analytical characterization of an OPSA system was discussed when the input transparencies are ideal Ronchi optical gratings. Particular attention was given to characterizing the resultant optical signals from ROSA (Recording Optical Spectrum Analyzer) photodiode detectors having 32 concentric ring detectors on one semi-circle and 32 equally sized wedge detectors on the conjugate semi-circle. This result formed the basis for presenting a computer simulation program in the following chapter, along with simulation results from its use under a wide range of operational parameters with two commercially available ROSA detectors of slightly different detector element configuration. One detector had mid-radii of the ring elements spaced logarithmically, and the other detector had linear spacings. These simulation results indicated that as many as 27 rings and 32 wedges yield factor map encoding potentials for 864 thematic data classes (27 x 32) with detection signal-to-noise ratios greater than 1.0 when the $f^\#$, i.e. the ratio of the transform lens focal length to the sampling aperture diameter, is less than 1,000. These results motivated an attempt to redesign the ROSA detector element configuration to effect better performance. The detector redesigns with equal ring element spacings resulted in a capability of detecting 30 rings and 32 wedges, i.e. 960 thematic data classes, with a signal-to-noise ratio greater than 1.0.

Preliminary design of an optical subsystem for detection of grating maps is developed in Chapter V to indicate how the interaction of system parameters forces the designer to make trade-offs for realistic optical system specification. Here particular attention is given to sampling aperture diameter, which determines the resolution of factor map sampling. For example, a 22- by 29-inch factor map having a scale of 1:50,000 when reduced 10x will have a format size of 55.9 mm by 73.7 mm, which is suitable for commercial 70-mm chips or roll films, and a 0.1-mm-diameter sampling aperture will have an equivalent resolution of 50 meters on the ground. Trade-offs leading to smaller grating map formats are then investigated. Significant findings indicate that a 0.051-mm sampling aperture having approximately a 25-meter ground resolution can have the same signal-to-noise results as the 0.1 mm aperture with 50-meter ground resolution if the laser light wavelength is changed from the HeNe $0.6328\mu\text{m}$ to HeCd at $0.350\mu\text{m}$.

In Chapter VI, the technology for producing grating maps is reviewed and approaches for extending capabilities to produce gratings with increased storage capacity are outlined. Two systems appear to have the specifications necessary for generating grating maps: the electron beam recorder made by Image Graphics Inc., and the cathode ray tube system available from Information International Inc. However, without test

data there is a question of how precisely either system could produce a Ronchi grating for a selected spatial frequency within their operational range. An example worksheet (table 25) is given to outline selection of the grating detection system parameter values, which indicates that the electron beam recorder has a potential to encode Ronchi gratings at 17 selected spatial frequencies and 32 directions for a total of 544 thematic data classes. Means for increasing the number of thematic data classes are discussed for amplitude coding, e.g. with 10 gray scale levels for the Ronchi gratings the electron beam recorder could encode 3,481 separate thematic data classes in a single grating map. Likewise, multiple gratings composed of superimposed gratings or gratings prepared in color transparencies decoded by selected laser light wavelength illumination provide potential for increasing data capacity in a grating map.

In Chapter VII, concepts for the optical, electronic, digital, and storage and retrieval subsystems are described. For example, several optical subsystem configurations are described and illustrated for (1) stationary light beam optical subsystems with moving input transparencies and (2) a telecentric scanning beam optical subsystem with stationary input transparencies. It is shown that one- or two-dimensional telecentric scanning can be accomplished with either the standard refractive optics afforded by glass lenses or by reflective optics with parabolic mirrors. Integration of a photodiode array detector into an OPSA optical subsystem is presented to assist in registering image and stage coordinate systems as well as serving as a possible aid in resolving boundaries between contiguous gratings on an input grating map. It is shown how spatial light modulations, such as Itek's PROM device, might be used in OPSA systems.

Also in this Chapter, coordination of the various subsystems into an integrated automated system is described in an example scenario. This system features a carousel for storing the reduced factor map data encoded as Ronchi gratings. The simple system uses a minicomputer as a central processor to coordinate and control the various subsystem operations and to process data for internal use. Microcomputers are interfaced to an OPS detector and to an image plane photodiode array detector to increase system efficiency by removing processing, control, and decision tasks from the central computer. OPSA samples can be preprocessed and classified within the microprocessors, and the reduced class nemonic can be stored in local buffers until transmission to central system memory via direct memory access when the buffer is full. This system could be programmed to operate in a true automated fashion by accepting formatted problem statements for a defined geographic area and for a defined problem for which an application algorithm exists, e.g. cross-country mobility between selected points for a given class of vehicles. The central computer could select the appropriate factor map transparencies, transfer them sequentially to the sampling system, register them in the sampling coordinate system, and select the areas of the transparencies to be sampled, the sample spacing, and sampling aperture size. The OPSA detector microcomputer could process sample data while the translation stage is moving to the next sample position. The central

computer could use these spatial data, along with temporal data, e.g. local weather history and projected weather, to compute or decide on a problem answer for each sample location. The processed data could then be formatted and displayed for human inspection or placed in a computer file for access for map overprinting by automated cartography systems.

IX. CONCLUSIONS

This preliminary investigation of optical power spectral analysis approaches to machine-readable factor maps for use in terrain information systems has developed information and data indicating that the concepts are feasible. Experimental testing of the simulated system concepts can provide data useful for system design and implementation planning.

**DAT
FILM**